Vapochromism Induced by Intermolecular Electron Transfer Coupled with Hydrogen-Bond Formation in Zinc Dithiolene Complex

Mori and Ozaki Groups

Reversible control of electronic functionalities of molecular materials using external stimuli and perturbations is important not only for applications to next-generation switching devices and sensors but also from the viewpoint of basic science to elucidate the mechanism and to establish the material design criteria. Recently we have demonstrated a proton-electron coupled phenomenon in H (hydrogen)-bonded π-conjugated molecular crystals [1-3], in which magnetism and electrical conductivity were switched by proton (deuteron) dynamics in an intermolecular H-bond. If control of the functionalities, such as optical properties, other than magnetism and electrical conductivity by modulating the electronic states through H-bonding is well established, it will impact various research fields and greatly expand the design criteria of functional materials. As one of the functional molecular materials with optical properties responsive to external stimuli, vapochromic materials, which respond with color changes when exposed to solvent vapors, have been actively studied as good candidates for their use as chemical sensors because they can directly visualize external environmental changes. In this study, we focused on a novel Zn complex, $(Ph_4P)_2[Zn(4\text{-mxbdt})_2]$ (**1** in Fig. 1; 4-mxbdt = 4-methoxybenzene-1,2-dithiolate) to realize the control of vapochromic behavior by direct modulation of electronic states through H-bonding. Based on the detailed single-crystal structure analyses and first-principles calculations considering intermolecular interactions using the periodic structure model of the crystal, we disclosed a new mechanism of vapochromism in **1**, that is, not molecular structure and arrangement changes but electron transfer via H-bond formation for the first time [2].

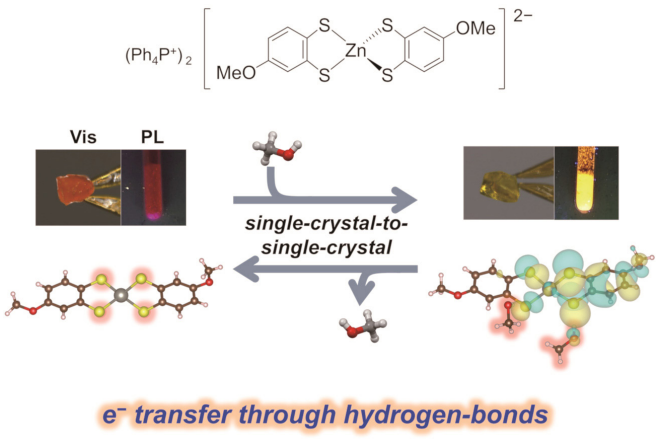

Fig. 1. A novel vapochromic mechanism by intermolecular electron transfer coupled with hydrogen-bond formation was realized in a zinc dithiolene complex crystals, $(Ph_4P)_2[Zn(4\text{-mxbdt})_2]$ (**1**, left) and **1**·2CH_3OH (right).

The Zn complex **1** was synthesized by complexation of zinc(II) chloride and the ligand precursor in methanol. Yellow block-like crystals were obtained by the slow evaporation of the crude mixture. From the X-ray structural analysis, the yellow crystal was determined as $(Ph_4P)_2[Zn(4\text{-mxbdt})_2]\cdot 2CH_3OH$ (= **1**·2MeOH) (Fig. 1). In this crystal, the $[Zn(4\text{-mxbdt})_2]$ complex showed tetrahedral coordination without a π-stacking structure because of the presence of bulky Ph_4P^+ cations, and thus there were no significant intermolecular interactions between the complexes. The spaces in the loosely packed structure were filled with two methanol molecules per formula. These methanol molecules formed [S···H–O] H-bonds with S atoms on the $[Zn(4\text{-mxbdt})_2]^{2-}$. Interestingly, drying the crystals overnight under vacuum induced the color change from yellow to orange, maintaining its high crystallinity (Fig. 1).

We quantitatively evaluated the color change of each crystal by UV-vis absorption spectra. Visible-light absorption edges of the orange crystal **1** and yellow crystals, **1**·H_2O and **1**·2MeOH, were estimated to be 2.29 eV (541 nm), 2.41 eV (514 nm), and 2.45 eV (506 nm), respectively. A blue shift of the absorption edge (0.12–0.16 eV) upon methanol or water vapor absorption was observed, which is consistent with the visually observed color changes. We also evaluated the photoluminescence properties of these crystals. Significantly, a blue shift was observed in the photoluminescence spectra (0.10–0.14 eV) for both **1**·H_2O and **1**·2MeOH, similar to the

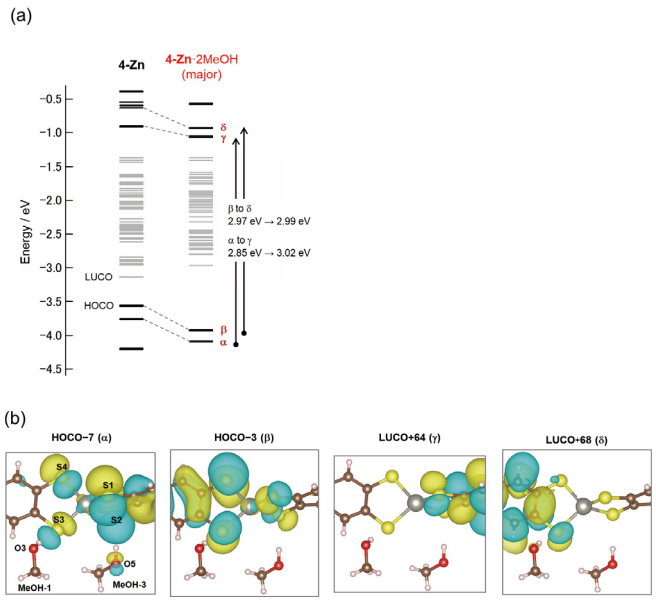

Fig. 2. (a) Crystal orbital energies of **1** and **1**·2MeOH (major) and (b) corresponding crystal orbitals in **1**·2MeOH (major). Crystal orbitals from -3.2 eV to -1.3 eV (left; gray lines) are mostly on Ph_4P^+ cation molecules.

UV-vis absorption spectra. The apparent color changed from red to yellowish-orange. These experimental data demonstrate that crystal **1** is a novel vapochromic material having both visible-light absorption and photoluminescence changes when exposed to methanol or water sorption with reversible SCSC (single crystal-single crystal) transformations. Remarkably, this is the first report of metal-dithiolene-based vapochromic materials with SCSC transformations.

Then, we focused on the mechanism of vapochromism in this crystal, **1**·2MeOH. DFT calculations based on the experimentally observed crystal structures using OpenMX software revealed the mechanism of the Fig. 2(b) H-bonding structures in **1**·2MeOH. In **1**·2MeOH (major), energy gaps for both α to γ and β to δ transitions increased (α to γ: 2.85 eV to 3.02 eV, β to δ: 2.97 eV to 2.99 eV), where the α and β orbitals were more stabilized than γ and δ (Fig. 2 (a)). This is because of the fact that the occupied orbital groups (α and β) have a large weight on the H-bonding S atoms, on which the largest changes in the number of electrons were estimated by Mulliken population analysis, compared with the unoccupied orbital groups (γ and δ). Considering the orbital shape around the H-bond, these crystal orbitals are derived from the hybridization of the frontier orbitals (HOMO-1, HOMO, LUMO, and LUMO+1) of the $[Zn(4\text{-mxbdt})_2]^{2-}$ complex with the LUMO of the absorbed vapor molecules at higher energies. This hybridization leads to the above-mentioned electron transfer to stabilize both the α/β and γ/δ orbitals.

In conclusion, a novel mechanism of vapochromism based on the intermolecular electron transfer coupled with H-bond formation was realized in the newly obtained zinc dithiolene complex crystal, $(Ph_4P)_2[Zn(4\text{-mxbdt})_2]$ $2CH_3OH$. According to the mechanism proposed in this study, molecules in which molecular orbitals for visible-light absorption are significantly distributed to H-bonding parts can be promising candidates for a new class of vapochromic materials. The findings here provide important insights to expand the scope of molecular designs for vapochromic as well as other stimuli-responsive materials.

References

[1] S. Yokomori, A. Ueda, T. Higashino, R. Kumai, Y. Murakami, and H. Mori, Cryst Eng Commun. **21**, 2940 (2019).
[2] S. Yokomori, S. Dekura, T. Fujino, M. Kawamura, T. Ozaki, and H. Mori, J. Mater. Chem. C. **8**, 14939 (2020).
[3] S. Yokomori, S. Dekura, A. Ueda, R. Kumai, Y. Murakami, and H. Mori, J. Mater. Chem. (to be published).

Authors

S. Yokomori, S. Dekura, T. Fujino, M. Kawamura, T. Ozaki, and H. Mori

Nonlinear Anomalous Hall Effect in Organic Massive Dirac Fermion System

Osada Group

When an electron system has a conduction band with a finite Berry curvature and no time reversal symmetry, it may exhibit the intrinsic anomalous Hall effect (AHE) even at zero magnetic field. This topologically nontrivial transport phenomena disappears in equilibrium state of the system with time reversal symmetry. However, the AHE may revive as a nonlinear transport phenomenon in the non-equilibrium state carrying finite electric current.

In this study, we predicted the nonlinear AHE in a layered organic conductor α-$(BEDT\text{-}TTF)_2I_3$, and confirmed it experimentally. This is the first example of topological transport phenomena in organic conductors. We focused on the "weak" charge ordering (CO) state in α-$(BEDT\text{-}TTF)_2I_3$, where the inversion symmetry is broken. This compound exhibits a phase transition to a CO insulator at 135 K at ambient pressure. This CO transition is suppressed by pressure, and a two-dimensional (2D) massless Dirac fermion (DF) state appears above the critical pressure $P_c \sim 1.3$ GPa. The CO state just below P_c is called the weak CO state.

First, we experimentally established the fact that the weak CO state is a 2D massive DF state with a pair of tilted gapped Dirac cones [1]. We used the temperature-dependent peak structure of the interlayer magnetoresistance, which is peculiar to the layered DF system. The magnetic field dependence of the peak temperature observed in the weak CO state is explained only by the massive DF with a finite gap. Therefore, a finite Berry curvature appears in the weak CO state.

Next, we investigated the nonlinear AHE in the current-carrying state in the 2D massive DF system [2]. Under the time reversal symmetry, the sum of Berry curvature over occupied states is canceled out between the Kramers pair of Dirac cones, resulting in no AHE in the equilibrium state. However, if the Dirac cones are tilting, this Berry curvature balance is broken between the Dirac cone pair in the current-carrying state with non-equilibrium distribution. It revives finite AHE as the current-induced nonlinear AHE. The efficiency for the appearance of this current-induced phenomenon is represented by the Berry curvature dipole (BCD) of the system. We demonstrated the anisotropy and rectification characteristics (non-reciprocity) of the nonlinear AHE in the 2D tilted massive DF system. The generated Hall current exhibits unidirectionality even under an external AC field. Furthermore, we quantitatively estimated the nonlinear AHE expected in the weak CO state in α-$(BEDT\text{-}TTF)_2I_3$, and concluded that it is within the measurable range.

In real α-$(BEDT\text{-}TTF)_2I_3$, there may exist two types of

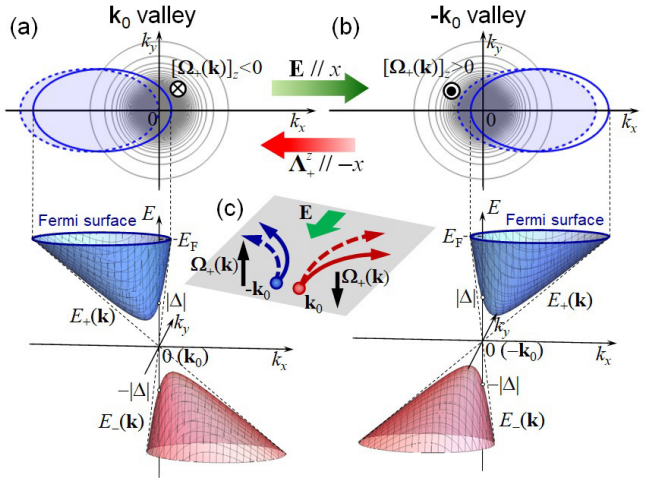

Fig. 1. Current-carrying state in the 2D massive DF system with tilted Dirac cones around (a) $\mathbf{k}_0$ and (b) $-\mathbf{k}_0$. Lower panels depict the band dispersion and upper panels illustrate the Berry curvature (contours) and the Fermi surface of the conduction band. The hatched region indicates occupied states in the current-carrying state. (c) Schematic of the nonlinear AHE. The balance of average anomalous velocity of electrons around $\mathbf{k}_0$ and $-\mathbf{k}_0$ is broken (dashed arrows) in the current-carrying state.

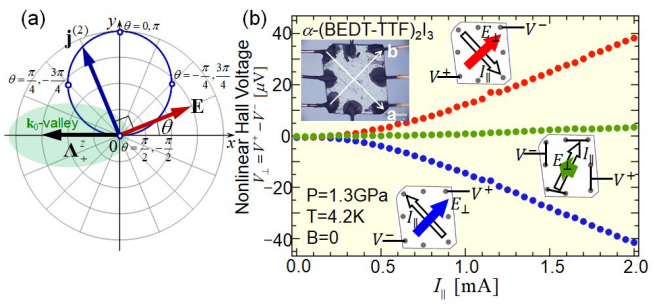

Fig. 2. (a) Dependence of anomalous Hall current **j**(2) on the electric field direction θ in the current-carrying state. (b) Nonlinear AHE observed in the weak CO state in α-(BEDT-TTF)$_2$I$_3$. It shows the rectifying characteristics, that is, the same Hall voltage against reversed current.

CO domains, which cancel the nonlinear AHE under current. So, we proposed the "current-field-cooling" technique, for macroscopic emergence of nonlinear AHE [2]. It utilizes the current-induced orbital magnetization (orbital Edelstein effect) to enhance the formation of single type of CO domains.

Finally, we attempted an experimental confirmation of the nonlinear AHE in the weak CO state in α-(BEDT-TTF)$_2$I$_3$. We performed transport measurements in the weak CO state at 1.25 GPa and 4.2 K, and extracted the nonlinear signal from current-reversed data. We successfully observed nonlinear AHE with estimated order and rectifying characteristics only below the CO transition temperature [3].

References
[1] K. Yoshimura, M. Sato, and T. Osada, J. Phys. Soc. Jpn. **90**, 033701 (2021).
[2] T. Osada and A. Kiswandhi, J. Phys. Soc. Jpn. **89**, 103701 (2020); *ibid*. 128002 (2020).
[3] A. Kiswandhi and T. Osada, arXiv: 2103.00300.

Authors
T. Osada, A. Kiswandhi, K. Yoshimura, M. Sato, K. Uchida, and T. Taen

Thermal Hall Effects of Spins and Phonons in Kagome Antiferromagnet Cd-Kapellasite

Yamashita, Hiroi, Kawashima, and Sakakibara Groups

The trajectory of an electron bends as it moves through a magnetic field. This Hall effect has been thought to not appear in insulators because of the apparent absence of mobile electrons. But recent reports of a thermal version of this effect, known as the thermal Hall effect, in numerous insulators has led to broad attention from researchers to understand its origin as well as potential applications for thermal current control.

Thermal current in an insulator is carried by spins and phonons. This leads us to ask how these charge neutral carriers can be bent by magnetic fields and how one can separate these two effects. To clarify the issue, we investigate the magnetic insulator Cd-kapellasite $CdCu_3(OH)_6(NO_3)_2$, a kagomé antiferromagnet [1]. In Cd-kapellasite, Cu^{2+} ions form a kagomé structure with a dominant nearest-neighbor antiferromagnetic interaction J/k_B = 45 K. The geometrical frustration effect of the kagomé structure suppresses the magnetic order down to T_N = 4 K, realizing a spin liquid state in a wide temperature range $T_N < T < J/k_B$.

We find clear thermal Hall signals in the spin liquid phase in all samples. The thermal Hall conductivity (κ_{xy}) is larger in a higher-quality sample with a larger longitudinal thermal conductivity (κ_{xx}), whereas the temperature dependence of κ_{xy} is similar (Fig. 1(a)). At 15 T, κ_{xy} and κ_{xx} are found to show a peak at almost the same temperature, a telltale sign of a phonon contribution κ_{xy}^{ph} in κ_{xy} at high fields. In addition, we find that the field dependence of κ_{xy} turns to be nonlinear at low temperatures and at low fields (Fig. 1(b)), concomitantly with the appearance of the field suppression of κ_{xx}, indicating the presence of a spin contribution κ_{xy}^{sp} in κ_{xy} at low fields. This is the first observation of both κ_{xy}^{ph} and κ_{xy}^{sp} in the same magnetic insulator.

Remarkably, by assembling the κ_{xx} dependence of κ_{xy}^{sp} data of other kagome antiferromagnets, we find that, whereas κ_{xy}^{sp} stays a constant in the low-κ_{xx} region (the "intrinsic" line in Fig. 2), κ_{xy}^{sp} starts to increase as κ_{xx} does in the high-κ_{xx} region (the "extrinsic" line in Fig. 2). This κ_{xx} dependence bears similarity to that of the anomalous Hall effect in ferromagnetic metals; the intrinsic mechanism by the Berry curvature is dominant in a moderate dirty metal, whereas the extrinsic mechanism by skew scatterings is dominant for a superclean metal. This good analogy indicates the presence

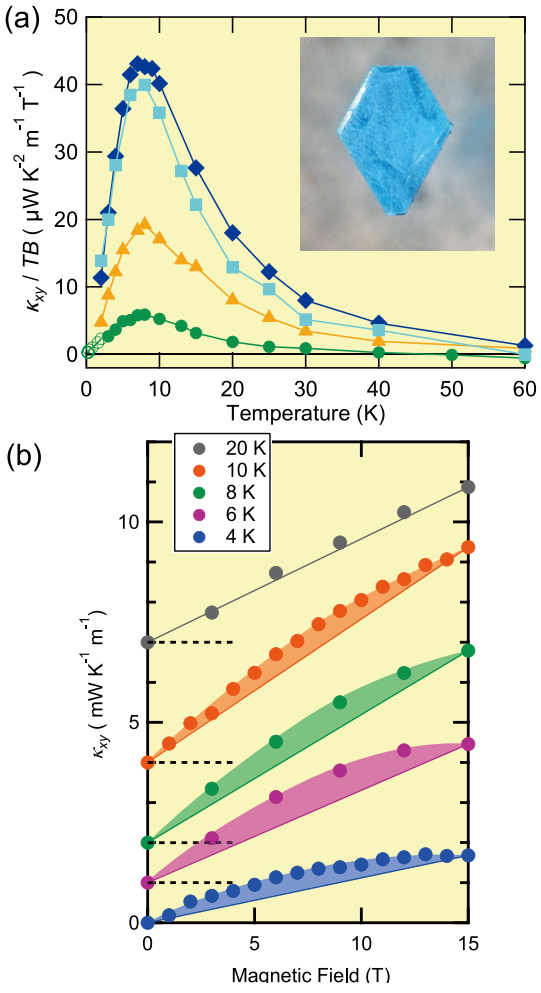

Fig. 1. (a) The temperature dependence of the thermal Hall conductivity of Cd-kapellasite of different samples at 15 T [1]. All the samples show a peak at the same temperature, but with different magnitudes. (b) The field dependence of κ_{xy} at different temperatures. The non-linear part (colored region) shows the spin contribution.

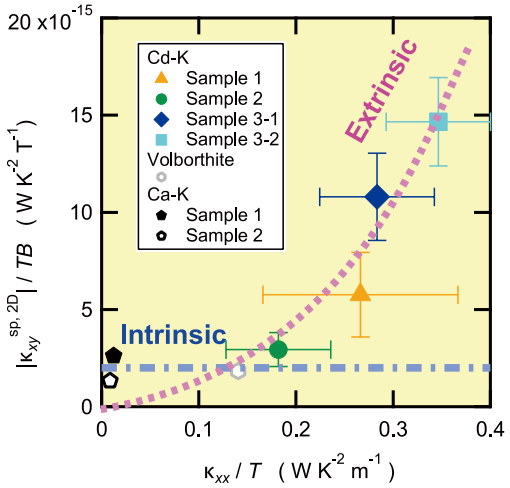

Fig. 2. The dependence of the spin thermal Hall conductivity per the 2D kagomé layer ($\kappa_{xy}^{sp,2D}$) on the longitudinal thermal conductivity (κ_{xx}) of Cd-kapellasite [1], Volborthite [2], and Ca-kapellasite [3]. The blue and pink dashed lines are guides to the eye for the intrinsic and extrinsic contributions, respectively.

of a similar duality of intrinsic-extrinsic mechanisms for the spin thermal Hall effect of an insulator.

Furthermore, we find that both κ_{xy}^{ph} and κ_{xy}^{sp} disappear in the antiferromagnetic ordered phase at low fields, showing that phonons alone do not exhibit the thermal Hall effect. A high field above approximately 7 T induces κ_{xy}^{ph}, concomitantly with a field-induced increase of κ_{xx} and the specific heat, suggesting a coupling of the phonons to the field-induced spin excitations as the origin of κ_{xy}^{ph}.

References
[1] M. Akazawa *et al.*, Phys. Rev. X **10**, 041059 (2020).
[2] D. Watanabe *et al.*, Proc. Natl. Acad. Sci. USA **113**, 8653 (2016).
[3] H. Doki, M. Akazawa, H.-Y. Lee *et al.*, Phys. Rev. Lett. **121**, 097203 (2018).

Authors
M. Akazawa, M. Shimozawa[a], S. Kittaka[b], T. Sakakibara, R. Okuma, Z. Hiroi, H.-Y. Lee[c], N. Kawashima, J. H. Han[d], M. Yamashita
[a]Osaka University
[b]Chuo University
[c]Korea University
[d]Sungkyunkwan University

Presence and Absence of Itinerant Gapless Excitations in the Quantum Spin Liquid Candidate $EtMe_3Sb[Pd(dmit)_2]_2$

Yamashita Group

The presence or absence of itinerant gapless excitations in the organic quantum spin liquid (QSL) candidate $EtMe_3Sb[Pd(dmit)_2]_2$, probed by a finite residual linear term in the thermal conductivity $\kappa_0/T \equiv \kappa/T\ (T \to 0)$, has been controversial hot topic. We find that κ_0/T strongly depends on the cooling process. A finite κ_0/T is observed in a slow-cooled sample, but not in a rapid-cooled sample [1]. These results provide evidence that the true ground state of $EtMe_3Sb[Pd(dmit)_2]_2$ is a QSL with itinerant gapless excitations.

The organic Mott insulator $EtMe_3Sb[Pd(dmit)_2]_2$ possesses a nearly isotropic triangular lattice of localized spin-1/2 on the $Pd(dmit)_2$ dimers. This geometrical frustration effect caused by the triangular lattice and a proximity effect of the Mott transition are believed to enhance the zero-point fluctuation not to allow the spins to order. While the presence of a finite linear residual thermal conductivity, $\kappa_0/T \equiv \kappa/T\ (T \to 0)$ has been shown [2], recent experiments [3, 4, 5] have reported the absence of κ_0/T in some samples. (Fig. 1). However, in the experiments reporting the absence of κ_0/T, the phonon thermal conductivity is strongly suppressed [3]. In sharp contrast, a large phonon thermal conductivity with a phonon mean free path reaching almost the boundary limit is observed in the experiments showing the presence of the κ_0/T. Therefore, it is not clear if the absence of κ_0/T shows absence of the gapless spin excitations or if the gapless spin excitations are simply suppressed when the phonons are strongly scattered.

Here we show that both the magnitude of the phonon thermal conductivity and the presence/absence of κ_0/T strongly depend on the cooling process of the sample. When cooling down very slowly, a sizable κ_0/T is observed. In contrast, when cooling down rapidly, κ_0/T vanishes and, in addition, the phonon thermal conductivity is strongly suppressed. These results suggest that possible random scatterers introduced during the cooling process are responsible for the apparent discrepancy of the thermal conductivity data in this organic system. The present results provide evidence that the true ground state of $EtMe_3Sb[Pd(dmit)_2]_2$ is likely to be a quantum spin liquid with itinerant gapless excitations.

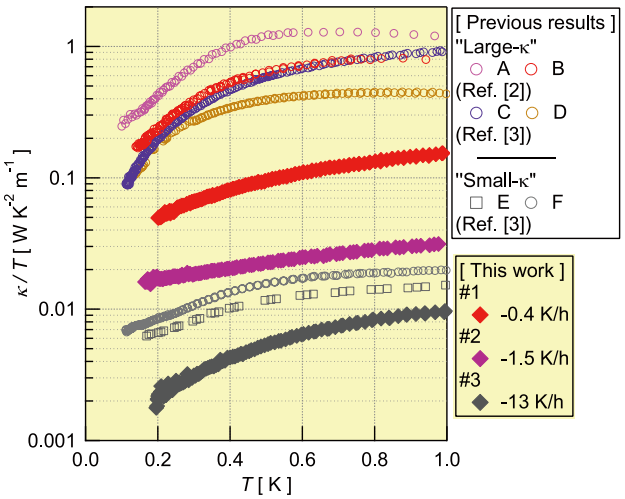

Fig. 1. Temperature dependence of the thermal conductivity divided by the temperature of $EtMe_3Sb[Pd(dmit)_2]_2$. The data of the previous reports [2, 3] are also plotted.

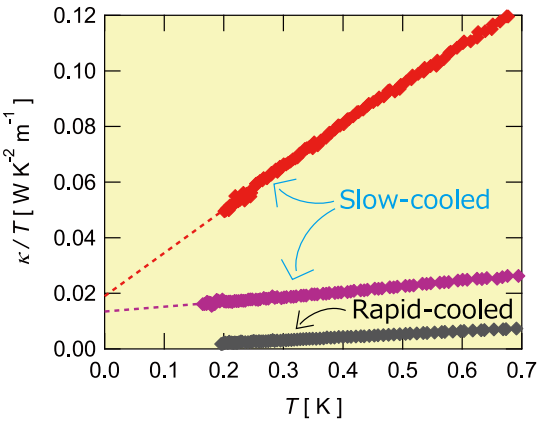

Fig. 2. Low-temperature data of κ/T plotted as a function of T. The dashed lines show an extrapolation of the data.

References
[1] M. Yamashita *et al.*, Phys. Rev. B **101**, 140407(R) (2020) * Editor's suggestion.
[2] M. Yamashita *et al.*, Science **328**, 1246 (2010).
[3] M. Yamashita, J. Phys. Soc. Jpn. **88**, 083702 (2019).
[4] P. Bourgeois-Hope *et al.*, Phys. Rev. X **9**, 041051 (2019)
[5] J. M. Ni *et al.*, Phys. Rev. Lett. **123**, 247204 (2019).

Authors
M. Yamashita, Y. Sato[a], T. Tominaga[a], Y. Kasahara[a], S. Kasahara[a], H. Cui[b], R. Kato[b], T. Shibauchi[c], and Y. Matsuda[a]
[a]Kyoto University
[b]RIKEN
[c]The University of Tokyo

Sample Dependence of the Half-Integer Quantized thermal Hall Effect in a Kitaev Candidate α-$RuCl_3$

Yamashita and Uwatoko Groups

Non-trivial topology in a condensed-matter state realizes a quantization of a physical quantity. One of the most fundamental examples is the quantized Hall conductivity in a quantum Hall system, where the quantized Hall conductivity is given by the Chern number determined by the topology of the system.

A new intriguing case of this topological quantization is now found in a magnetic insulator, a Kitaev magnet. In the Kitaev model, localized spin-1/2 moments on a two-dimensional (2D) honeycomb structure are coupled each other by bond-dependent Ising interactions. The frustration effect of this Kitaev Hamiltonian prevents the spins from ordering even at the zero temperature, realizing a quantum spin liquid state. Remarkably, this ground state of the Kitaev Hamiltonian is exactly solvable. The ground state has been shown to be characterized by the two kinds of elementary excitations; itinerant Majorana fermions and localized Z_2 fluxes. In a magnetic field, this itinerant Majorana fermions have topologically non-trivial gapped bands with the Chern number $C = \pm 1$, giving rise to a quantized chiral edge current protected by the field-induced gap. In contrast to a quantized chiral edge current of electrons in a quantum Hall system, this chiral edge current is carried by the charge neutral Majorana fermions. Therefore, this quantized chiral edge current has been predicted to appear in the 2D thermal Hall conductivity as $\kappa_{xy}^{2D}/T = q_t C/2$, where $q_t = (\pi/6)k_B^2/\hbar$.

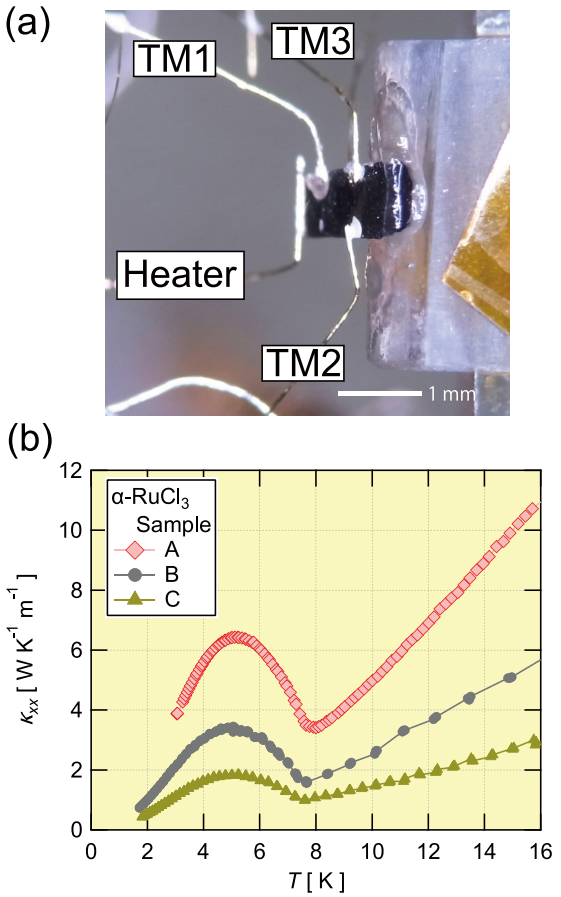

Fig. 1. (a) A setup picture of the thermal conductivity (κ_{xx}) and the thermal Hall (κ_{xy}) of α-$RuCl_3$ (sample A). The sample was tilted to the base plate so that the magnetic field oriented to 45 degree to the c axis. (b) The temperature dependence of κ_{xx} of different samples (A, B, and C) at zero field.

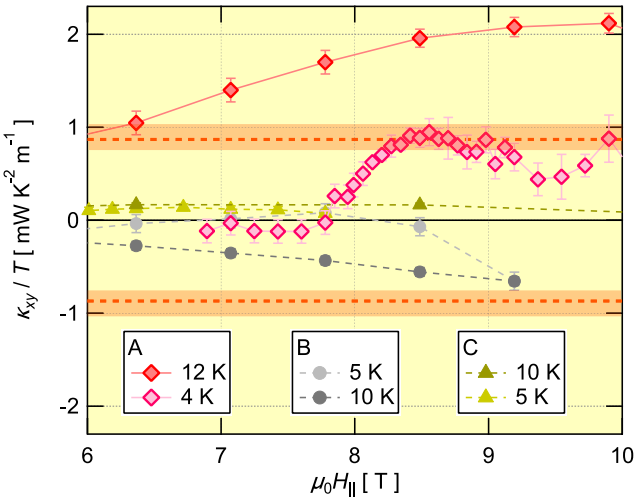

Fig. 2. The in-plane field dependence of κ_{xy}/T of all the samples. The dotted lines show the value corresponding to the half-integer quantized thermal Hall effect $\kappa_{xy}^{2D}/T = q_t C/2$, where $q_t = (\pi/6)k_B^2/\hbar$. The sign of κ_{xy} of sample A is inverted for a clarity.

In this work [1], we reveal that it is necessary to protect the chiral edge current from severe scattering effects on phonons to stabilize the quantized thermal current. We investigate the sample dependence of the longitudinal (κ_{xx}) and transverse (κ_{xy}) thermal conductivity of three single crystals of α-$RuCl_3$ – a promising candidate realizing the Kitaev spin liquid [2]. We find the half-integer quantized thermal Hall effect in a sample showing the largest κ_{xx} among the three crystals (sample A in Fig. 1). On the other hand, the other samples with smaller κ_{xx} show κ_{xy} much smaller than the value expected for the quantization (Fig. 2). Given that κ_{xx} is mostly given by phonons, the different magnitudes of κ_{xx} in different samples reflect the different scattering strengths on phonons; phonons in a sample with smaller κ_{xx} are exposed in stronger scattering effects. Therefore, the dependence of κ_{xy} on κ_{xx} shows that the chiral edge current in the Kitaev magnet is sensitive to scattering effects on phonons.

Further, we find that a sample with a larger κ_{xx} shows a larger decrease of the magnetic susceptibility below the Néel temperature, in addition to a larger field-increase effect of κ_{xx}, showing that magnetic scattering effects are more strongly suppressed by magnetic fields in a sample with a better quality. These results suggest that suppressing this magnetic scattering effect plays an important role to realize the quantized thermal Hall effect.

References
[1] M. Yamashita *et al.*, Phys. Rev. B **102**, 220404(R) (2020).
[2] Y. Kasahara *et al.*, Nature 559, **227** (2018).

Authors
M. Yamashita, J. Gouchi, Y. Uwatoko, N. Kuritaa, and H. Tanakaa
[a]Tokyo Institute of Technology

Ultralow Temperature NMR of $CeCoIn_5$

Yamashita and Takigawa Groups

We have established the experimental procedures to measure high-field spin-echo NMR signals down to ultralow temperatures (~1 mK) with ensuring the thermal equilibrium between the sample and the cryostat [1]. This technique allows us to observe a peak in $1/T_1T$ of ^{59}Co NMR signals at ~20 mK, showing a magnetic transition in $CeCoIn_5$.

Understanding the role of enhanced quantum fluctuations near a magnetic quantum critical point (QCP) has been a central issue in condensed-matter physics, because such quantum fluctuations are believed to mediate various exotic phenomena, such as non-Fermi liquid behaviors, enhancements of effective mass, and unconventional Cooper pairings. Many studies of unconventional superconductivity near a magnetic QCP have been performed in heavy-fermion materials. Among the various heavy-fermion materials, $CeCoIn_5$ has been attracting broad attention because of its *d*-wave superconducting state with the high transition temperature of 2.3 K and the proximity to a putative magnetic QCP. However, no antiferromagnetic (AFM) state corresponding to the QCP has been observed, shrouding the origin of the QCP in mystery.

Recently, we have reported anomalous decrease in the de Haas–van Alphen (dHvA) amplitudes of $CeCoIn_5$ below 20 mK for 6–10 T [2]. An appearance of a field-induced AFM phase has been put forward to explain the decrease of the dHvA amplitude, because additional dissipation by

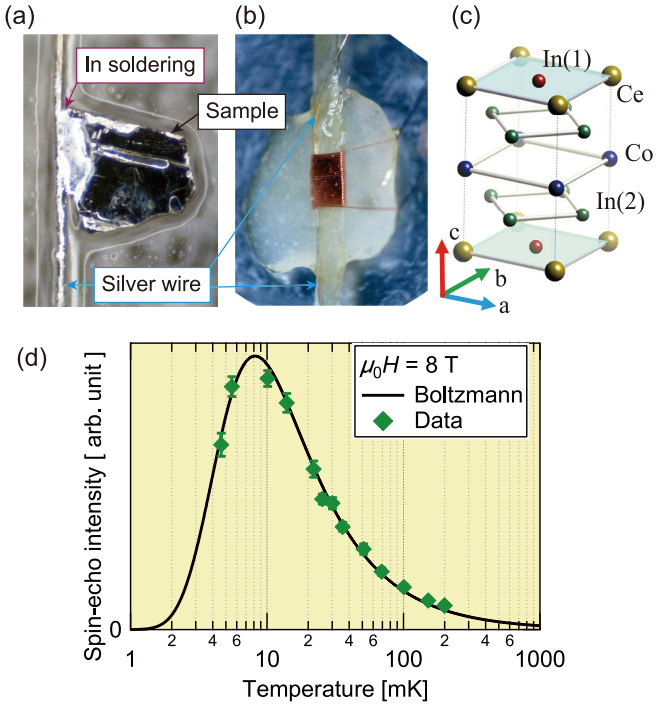

Fig. 1. (a) A picture of the sample with a silver wire (100 μm diameter) soldered by indium. (b) Cu wires were wound around the sample for NMR measurements. The silver wire was thermally anchored to the cryostat. (c) Crystal structure of $CeCoIn_5$. NMR measurements were performed at ^{59}Co (I = 7/2) nuclei. (d) The temperature dependence of the spin-echo intensity at 8 T. The solid line shows the calculation from the Boltzmann distribution of the nuclear spins.

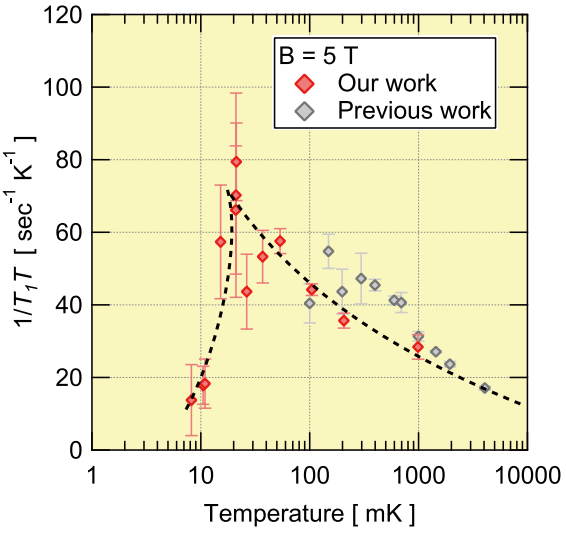

Fig. 2. The temperature dependence of $1/T_1T$ at 5 T. The data of the previous report [3] is also plotted. The dashed line shows a guide to the eyes.

magnetic breakdowns in the AFM phase can provide the most plausible explanation for the decrease of the dHvA amplitude. However, direct evidence of magnetic order has yet to be observed.

In this work, we performed spin-echo NMR measurements down to 5 mK to find the magnetic order. It is a very challenging issue to observe NMR signals down to ultralow temperatures without heating the sample. First, we made a strong thermal connection between the sample and the cryostat by indium soldering a silver wire to the sample (Fig. 1). Second, we find that the temperature dependence of the spin-echo intensity $I_{SE}(T)$ provides a good measure of the sample temperature. By taking into account the population difference of the nuclear spins in different energy levels which have the Boltzmann distribution, one can find the temperature dependence of $I_{SE}(T)$ as shown by the solid line in Fig. 1d. We confirm that the NMR signal follows the Boltzmann curve when the heating caused by the NMR pulses is negligible (Fig. 1d), allowing us to find a pulse condition without heating the sample.

Having established the NMR pulse conditions without heating of the sample, we investigate the temperature dependence of the longitudinal relaxation time (T_1). We find a pronounced peak in $1/T_1T$ at 5 T, implying an appearance of magnetic order as suggested by our previous dHvA measurements [2]. On the other hand, the NMR spectrum shows no change below 20 mK. Moreover, the peak in $1/T_1T$ disappears at 6 and 8 T in contrast to the results of the quantum oscillation. We discuss that an antiferromagnetic state with a moment lying in the *a*–*b* plane can be a possible origin for the peak in $1/T_1T$ at 5 T.

References
[1] M. Yamashita *et al.*, Phys. Rev. B **102**, 165154 (2020).
[2] H. Shishido *et al.*, Phys. Rev. Lett. **120**, 177201 (2018).
[3] T. Taniguchi *et al.*, JPS Conf. Proc. **30**, 011107 (2020).

Authors
M. Yamashita, M. Tashiro, K. Saiki, S. Yamada, M. Akazawa, M. Shimozawa[a], T. Taniguchi[b], H. Takeda, M. Takigawa, and H. Shishido[c]
[a]Osaka University
[b]IMR, Tohoku University
[c]Osaka Prefecture University

Dynamics of Composite Domain Walls in Multiferroics $FeGdO_3$

Tsunetsugu Group

Domain Walls (DW) are topological defects with mesoscopic size and understanding their dynamics is important for both experimental and theoretical interests. We have theoretically studied the steady state dynamics of DW driven by magnetic field in a system with multiple orders coexist [1].

Our target system is the multiferroic compound $FeGdO_3$ and its low-temperature phase is characterized by three order parameters: antiferromagnetic moments of Fe spins $\boldsymbol{N}$ with biaxial anisotropy and isotropic Gd spins $\boldsymbol{n}$ and one component of electric polarization P. Their coupling $c\boldsymbol{N}\cdot\boldsymbol{n}P$ leads to composite DWs, i.e. two order parameters need to flip together in each DW, and therefore there exist 3 different types of composite DWs: ***N*-*n*, *N*-*P***, and ***n*-*P***.

We have studied the dynamics of these composite DWs driven by magnetic field based on the phenomenological time-dependent Ginzburg-Landau theory. Neglecting fluctuations inside the DW, we have investigated by numerical calculations the time evolution of their one-dimensional motion. With the help of anisotropic exchange couplings, the applied magnetic field couples to $\boldsymbol{N}$ and thus drives ***N*-*P*** and ***N*-*n*** DWs. One important finding is the difference between these two types in the scaling of DW steady state velocity $v(c,H)$. In its weak field expansion $v(c,H) = \alpha(c^2)H+\beta(c^2)H^3+\ldots$, the coefficients exhibit a singularity at $c = 0$ for ***N*-*n*** DW, and this is related to $\boldsymbol{n}$'s internal isotropy.

As a big surprise, it turns out that a composite DW becomes unstable in strong magnetic field and splits into a pair of different types: ***N*-*P*** → ***N*-*n*** + ***n*-*P*** and ***N*-*n*** → ***N*-*P*** + ***n*-*P***. In both cases, ***n*-*P*** DW is immobile but its partner succeeds to the moving part after splitting. The possibility of this type of splitting was pointed out as an impurity effect [2], but we have found that it may occur in a pure bulk as a dynamical instability. An important point is that the non-flipping component is also dragged by the flipping ones due to the coupling c-term. With increasing the driving field, its modulation grows and finally creates a pair of kink and anti-kink, which is DW splitting. This type of dynamical instability may appear, in principle, in any systems with more than two types of order parameters. It is an interesting challenge to observe in experiments this splitting of composite DW.

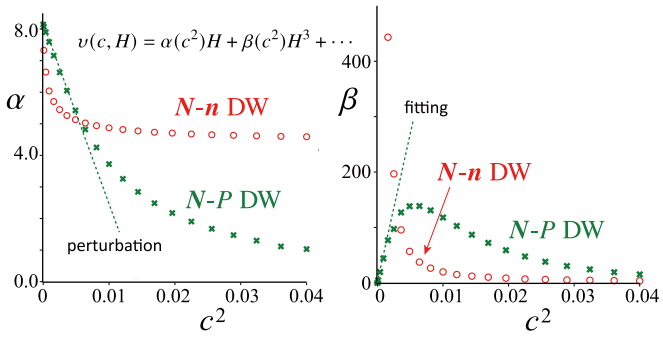

Fig. 1. Velocity of composite DWs driven by magnetic field expanded in H. α is the linear mobility. c is the interaction strength.

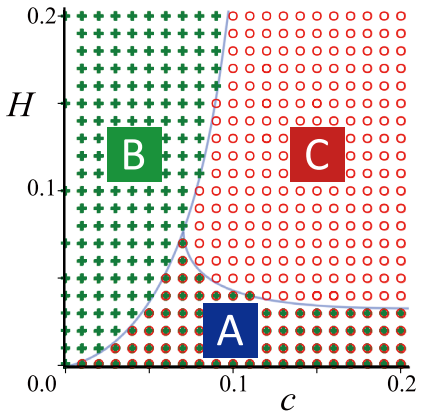

Fig. 2. Stability phase diagram of composite DWs driven by magnetic field H. B: ***N*-*n*** DW is unstable, C: ***N*-*P*** DW is unstable, A: both DWs are stable.

References

[1] K. Kawahara and H. Tsunetsugu, J. Phys. Soc. Jpn. **90**, 014703 (2021).

[2] Y. Tokunaga *et al.*, Nat. Mater. **8**, 558 (2009).

Authors

H. Tsunetsugu, K. Kawahara

Fermi-Liquid Correction in Current Noise through a Correlated Quantum Dot

Kato Group

Artificially generating, controlling, and measuring quantum states on semiconductor substrates is the key to realizing quantum information technology, such as quantum computers and quantum communications. On the other hand, the development of technologies to generate and control artificial quantum states has brought about a paradigm shift in material science. As a result, it has become possible to thoroughly explore the physical phenomena that give rise to nontrivial features of matter by artificially reproducing the quantum states in matter, rather than simply investigating the properties of natural matter as has been done in the past. Furthermore, through advanced control technology, it has become possible to precisely investigate the behavior of quantum many-body states in complex environments, such as nonequilibrium states, which were previously not easy to access.

Along with superconductivity and the quantum Hall effect, the Kondo effect is one of the fundamental many-body effects of electrons. The primary mechanism of the Kondo effect was elucidated in 1964 and has been thoroughly investigated since then. The Kondo effect occurs not only in dilute magnetic materials, where the phenomenon was originally discovered, but also in a variety of physical systems. Recently, many studies on the Kondo effect have been carried out in various physical fields, such as condensed states of light-trapped cooled atoms and quarks. However, the actual state of these systems often deviates from the ideal state assumed in the mathematical analysis. In other words, it is known that the symmetries possessed by physical states (time-reversal symmetry and particle-hole symmetry) are broken and play a significant role in the low energy states. However, the correction on the local-Fermi-liquid state beyond the linear response had remained a difficult problem until recently [1].

Consider a situation in which electrons are confined in a quantum dot, which is a device of several tens of

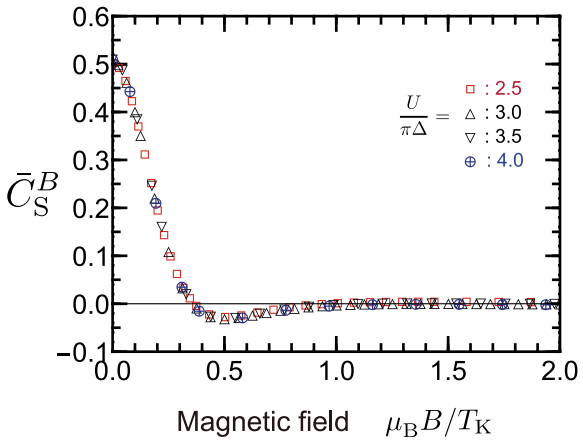

Fig. 1. Bias-voltage nonlinear coefficient of current noise $\bar{C}_S^B$ as a function of magnetic field B normalized by the Kondo energy scale (Kondo temperature) T_K for several choices of the Coulomb interaction $U/(\pi\Delta)$ is plotted. Here the current noise is given in the form $S = \frac{4e^2}{h}|eV|\left[S_1 + \bar{C}_S^B\left(\frac{eV}{T_K}\right)^2\right] + O(V^5)$. It is found that all the data points are on a universal curve.

nanometers in size made of a semiconductor or other material. In a quantum dot made of carbon nanotubes, for example, the shape of the electron confinement region is highly symmetric. As a result, in addition to the spin of the electrons, a magnetic moment is generated in the quantum dot due to the orbit of the electron motion. By attaching electrodes to this quantum dot, the number of confined electrons can be tuned, and the local-Fermi-liquid state can be controlled in a state of broken electron-hole symmetry. Using quantum field theory and mathematical methods, we have clarified that the local-Fermi-liquid corrections, which are caused by the three-electron correlation, play an essential role in the correlated quantum dot beyond the conventional theory on the local Fermi liquid. This three-electron correlation is particularly pronounced in quantum dots with multiple orbitals. For example, in the Kondo effect caused by electron spin alone, it is difficult to observe the local-Fermi-liquid corrections because the Kondo effect itself disappears when the number of electrons is changed.

Exploiting numerical simulations and field theory techniques, we have clarified that the local-Fermi-liquid corrections can be observed in actual experiments based on the transport quantities such as nonlinear current, current noise, and thermal conductivity [2]. We have also found that there is a scaling universality in the nonlinear current noise behavior when a magnetic field is applied to a quantum dot. Application of magnetic field breaks the time-reversal symmetry of the quantum dot and gives rise to the local-Fermi-liquid corrections in nonlinear transport quantities. It is also found that the local-Fermi-liquid corrections have a universal scaling property independent of the details of the nanoscale materials, similar to the conventional local-Fermi-liquid (see Figure).

This research has significantly advanced our understanding of the physical mechanisms that give materials their nontrivial features through the interaction of electrons. The Kondo effect is the most fundamental quantum many-body effect, and it appears in the properties of various materials. Therefore, it is expected to be helpful in designing new materials and exploring new materials in the future. In addition, the study of artificially controlled quantum many-body states in nanoscale materials requires highly sensitive observation techniques, which will contribute to the development of technologies to generate and control quantum states. Recently, our collaborators have succeeded in an experiment to verify the local-Fermi-liquid correction effect using current measurement on a carbon nanotube-based quantum dot [3].

As described so far, the results of this research are fundamental to the physics of condensed matter. However, it is expected that they will lead to the development of materials science and quantum information technology.

References
[1] C. Mora, C. P. Moca, J. von Delft, and G. Zarand, Phys. Rev. B **92**, 075120 (2015).
[2] Y. Teratani, R. Sakano, and A. Oguri, Phys. Rev. Lett. **125**, 216801 (2020).
[3] T. Hata, Y. Teratani, T. Arakawa, S. Lee, M. Ferrier, R. Deblock, R. Sakano, A. Oguri, and K. Kobayashi, Nat. Commun. **12**, 3233 (2021).

Authors
R. Sakano, Y. Teratani[a], and A. Oguri[a]
[a]Osaka city university

Sub-Atomic Lattice Distortion of an Atomic Layer Compound Visualized by Moiré Pattern

Komori Group

Chemical and physical properties are greatly affected by lattice distortion through the change of the electronic structures. At solid surfaces, the local distortion induced by the adsorbates, subsurface impurities and hetero-interface modify reactivity, growth and other atomic processes. By mapping the amplitude and direction of the local distortion, we can elucidate the details of the atom processes including surface reactivity. However, it has been technically difficult to observe the local distortion directly using microscopy methods. While scanning tunneling microscopy (STM) with atomic resolution is one of the ideal tools for studying the local structure, its lateral resolution is still insufficient to measure the distortion of the order of a few % of the lattice constant [1]. One of the ways to improve the lateral resolution is a use of the moiré pattern in the STM images [2]. In the present study, we demonstrate that the local lattice distortion of a hexagonal iron-nitride monatomic film grown over a flat and wide Cu terrace can be visualized by analyzing the moiré pattern. [3]

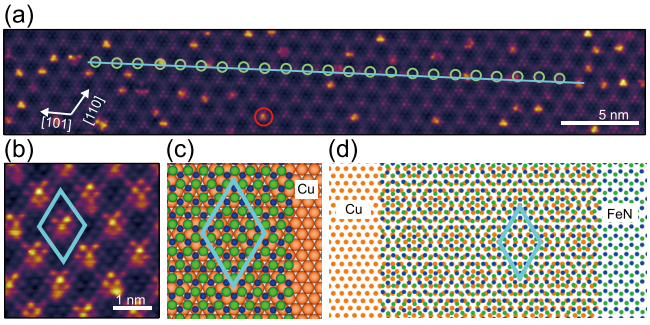

Fig. 1. (a,b) Topographic STM images of the hexagonal iron-nitride monolayer on Cu(111). Cyan line in (a) is drawn along the moiré pattern. The lattice orientation of the iron-nitride monolayer is indicated by green circles in (a). The red circle in (a) indicates the point protrusion. (c) Schematic model of the hexagonal iron-nitride monolayer on Cu(111). Green, blue and orange balls indicate Fe, N and Cu atoms, respectively. The Cu(111) lattice is rotated by 0.28° from the iron-nitride lattice. (d) Moiré pattern between the hexagonal iron-nitride monolayer and Cu(111) obtained by the schematic model in (c). Cyan rhombuses in (b), (c) and (d) show the unit cell of the moiré pattern [3].

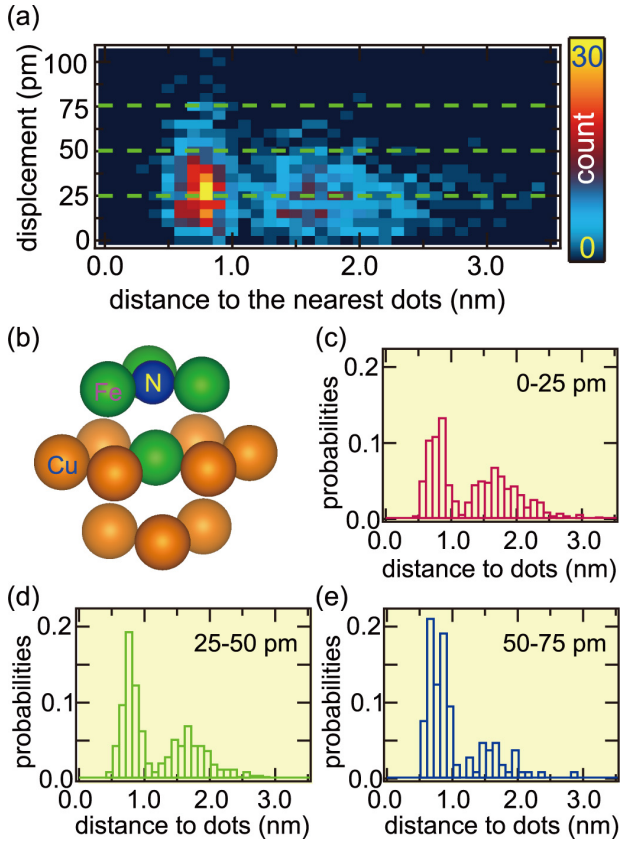

Fig. 2 (a) Two-dimensional histogram of the displacement of the moiré pattern center and the distance from the center to the nearest point protrusion. (b) Proposed schematic model of the point protrusion. (c–e) Histograms of the distance from the centers to the nearest point protrusions for three regions of the displacement 0- 25 pm in (c), 25–50 pm in (d), and 50–75 pm in (e). The counts are normalized by the total counts in each region [3].

Observed topographic STM images of the surface are shown in Fig. 1(a. b). A uniform iron-nitride film grows over the Cu(111) terrace larger than 100 × 100 nm^2, and a hexagonal moiré pattern with the periodicity of ~ 1.3 nm can be seen in the images. The green circles in Fig. 1(a) show the positions of the surface atoms along the [101] direction, and the cyan line is plotted along the moiré pattern. The latter is tilted from the lattice orientation of the hexagonal iron nitride monolayer by 1.1 ± 0.1°. A schematic model of the iron nitride monolayer on Cu(111) is displayed in Fig. 1(c). We assume that Fe atoms are observed as protrusions by STM. This model can reproduce the overall characteristics of the moiré pattern in the image including the 1.1° tilt as in Fig. 1(d). In the STM images, we notice larger and higher protrusions, which randomly distribute on the surface, than the atomic protrusions as indicated by the red circle in Fig. 1(a). We call them point protrusions.

A detailed analysis of the moiré pattern reveals that the center of the moiré pattern does not form a regular periodic lattice. The center positions randomly fluctuate from a hypothetical regular lattice points. Figure 2(a) shows a two dimensional histogram of the displacement of the moiré pattern center from the lattice point and the distance from the center of the moiré pattern to the nearest point protrusion. Our structural model of the point protrusion is given in Fig. 2(b). The histograms of the distance from the centers to the nearest point protrusions are made depending on the displacement to see the correlation more clearly as in Fig. 4(c–e). For the centers with a large displacement, the distance to the nearest point protrusion is relatively short compared to those with a small displacement. The point protrusions are preferentially formed in the regions with large lattice distortion of the iron nitride monolayer.

References
[1] S. Ohno *et al.*, Surf. Sci. **554**, 183 (2004).
[2] M. Ritter *et al.*, Phys. Rev. B **57,** 7240 (1998).
[3] T. Hattori *et al.*, Nano Lett. **21,** 2406 (2021).

Authors
T. Hattori, N. Kawamura,T. Miyamachi, and F. Komori

Steps as a Disorder on Atomic-Layer Superconductors

Hasegawa Group

Two-dimensional (2D) superconductors, whose thickness is thinner than the coherence length, exhibit peculiar properties. Compared with bulk superconductors, 2D superconductors are susceptible to disorder since induced electron localization enhances repulsive electron-electron interaction, which suppresses the Cooper pairing. As demonstrated with thickness-dependent critical temperature of amorphous superconducting thin films, changing parameters such as disorder, thickness, and perpendicular magnetic field lead to a superconductor-insulator transition (SIT). The zero-temperature transition is one of the typical examples of quantum phase transitions, and has been investigated extensively to elucidate its universal properties.

Recent technical advancements have allowed us to fabricate highly crystalline 2D superconductors, some of which has only mono-atomic layer thickness. In the case of such highly-ordered 2D superconductors it has been reported that during the SIT induced by the magnetic field application metallic phase appears in between. So far, the properties of this peculiar quantum metallic phase have been investigated mainly by transport measurements but the mechanism is still controversial. In order to understand its details atomistic real-space measurements are crucial. In the present study, we studied superconducting properties of striped-incommensurate (SIC) phase of the Pb/Si(111) system; one of the monoatomic-layer superconductors, formed on vicinal Si substrates. Since the substrate is tilted, uniformly distributed steps, whose spacing is equivalent or even smaller than the coherence length, should behave as a dispersed disorder on the ultimately thin superconductor. We investigated how the steps affect the superconducting properties and the magnetically induced SIT by using low-temperature scanning tunneling microscopy (STM).

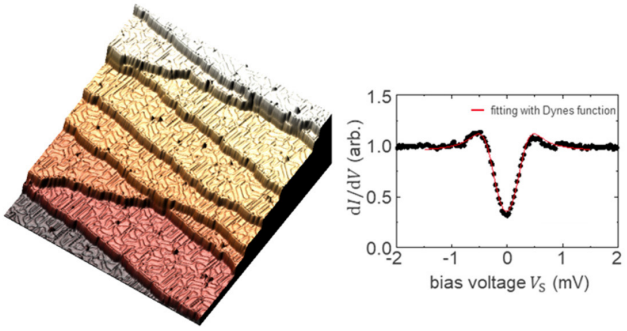

Fig. 1. (left) 3D-rendered STM image of striped incommensurate (SIC) phase of Pb/Si(111) system formed on a 1.1°-tilted vicinal substrate. (right) tunneling spectrum taken on a terrace of vicinal SIC phase taken at 0.36 K showing a superconducting gap of 0.30 meV.

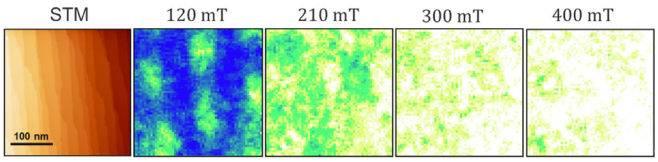

Fig. 2. STM image of the vicinal SIC superconducting phase and zero-bias-voltage maps, which correspond to the spatial distribution of the density of states (DOS) at the Fermi level, taken under the perpendicular magnetic field of 120, 210, 300, and 400 mT.

Figure 1 shows a 3D-rendered STM image of the SIC phase formed on a 1.1°-tilted vicinal Si(111) substrate taken at 0.36 K. A characteristic SIC stripe pattern can be seem on the terraces. In the image, the vertical scale is severely exaggerated; the step height corresponds to 0.31 nm whereas the averaged terrace width is 16 nm. A tunneling spectrum taken on a terrace shows a superconducting gap that can be well fitted with the Dynes function. The fitted superconducting gap, 0.30 meV, is almost same as that taken on SIC phase formed on a flat substrate, indicating the Cooper pairing is not affected by the presence of the steps.

In our previous studies on the role of steps on superconductivity, we found that the steps basically behave as a Josephson junction connecting the neighboring terraces, and the strength of the decoupling strongly depends on the phases [1, 2]. Among the Pb monolayer phases, the steps of the $\sqrt{3} \times \sqrt{43}$ phase decouple terraces significantly to make the terraces superconducting nano stripes [2]. On the other hand, the decoupling of the SIC phase is rather weak so that vortices are just pinned at step edges. In the case of the vicinal one, as the terrace width (16 nm) is much shorter than the coherence length of the flat one (38 nm), more than one steps are involved on the formation of a vortex.

Figure 2 shows an STM image and zero-bias-voltage maps, which correspond to the spatial distribution of the density of states (DOS) at the Fermi level, taken under various magnetic fields. At 120 mT, the vortices are observed elongated along the step direction. The DOS at the core of the vortices is not fully recovered to that of the normal metal. These are the characteristic features of an Abrikosov-Josephson vortex. The oval shape of the vortices is due to the reduced coherence length along the step-crossing direction caused by the limited mean free path due to the presence of the steps. Because of the reduced coherence length, the critical magnetic field, which is inversely proportional to the coherence length, is enhanced on the vicinal superconductor.

At the magnetic field of 210 mT, the number of vortices increases as well as the background DOS. The vortices are no longer distinct, and significant corrugation in DOS is discernible. By further increasing the magnetic field, DOS gradually increases and its distribution becomes homogeneous. Around 330 mT, DOS exhibits saturation, indicating the breaking of superconductivity. According to the transport measurement performed on the same phase the vortex liquid phase and quantum metallic phase are observed at these magnetic fields. The observed blur vortices and inhomogeneous DOS contrast presumably corresponds to thermally activated or quantum diffusing vortex liquid phase.

References
[1] S. Yoshizawa *et al.*, Phys. Rev. Lett. **113**, 247004 (2014).
[2] F. Oguro *et al.*, Phys. Rev B **103**, 085416 (2021).

Authors
Y. Sato, M. Haze, S. Yoshizawa[a], T. Uchihashi[a], and Y.Hasegawa
[a]National Institute for Materials Science

Carrier Density Control in Oxide Quantum Wells

Lippmaa group

Two-dimensional carrier confinement in a quantum well at an oxide heterointerface offers new ways of controlling the transport behavior of oxide materials by applied external fields. Magnetic tunability has been attributed to Rashba-type spin-orbit coupling in an asymmetric electron distribution, the enhancement of spin-orbit coupling close to a filling-dependent Lifshitz transition, or a change in the effective disorder experienced by carriers when the quantum well width changes. Electric fields, on the other hand, can be used to change the quantum well filling, by accumulating or depleting carriers at an interface, or to modify the width of the electron distribution in the depth direction.

Oxide quantum wells are usually formed by growing a thin epitaxial $LaAlO_3$ layer on $SrTiO_3$, in which case the quantum well forms at the surface of the $SrTiO_3$ substrate due to, at least in part, the change of lattice polarity at the interface. Instead of using the polar $LaAlO_3$ layer, it is also possible to form quantum wells by depleting oxygen from the surface or by delta-doping $SrTiO_3$ with a $(La,Sr)O_x$ monolayer. All these techniques produce a metallic quantum well with qualitatively similar properties, but the LaO_x delta-doping technique has several advantages in allowing a broad range of carrier densities to be explored. In contrast, the carrier number is essentially fixed by the polarity discontinuity at $LaAlO_3/SrTiO_3$ interfaces, while oxygen-deficient surfaces can only be maintained in ultra-high vacuum conditions.

In our recent work [1], we have studied the possibilities of constructing oxide quantum wells based on embedded $(La,Sr)O_x$ layers in $SrTiO_3$. The heterostructures were grown by Pulsed Laser Deposition on $SrTiO_3$ single crystals as illustrated in Fig. 1. The carrier number in these heterostructures is controlled by two parameters: the number of La atoms in the delta-doping layer, and the thickness of a $SrTiO_3$ capping layer. Since $SrTiO_3$ surfaces exposed to air are strongly depleted, a space-charge layer forms in the cap layer and the thickness of the capping layer can be used to partially deplete the carriers in from the quantum well. Almost complete carrier depletion occurs when the capping

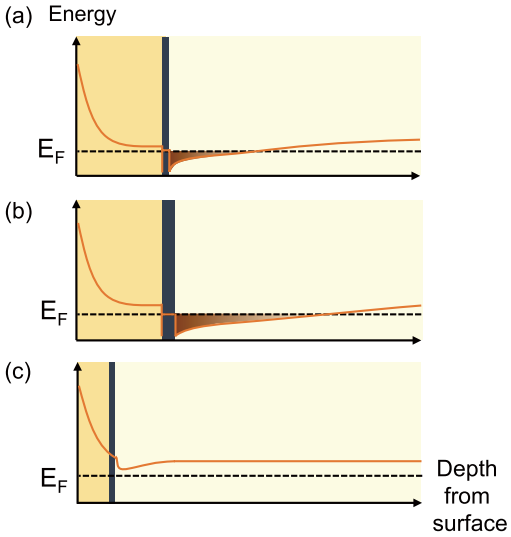

Fig. 1. Formation of a quantum well in $SrTiO_3$ around a $LaTiO_3$ delta doping layer. Due to surface depletion, carriers are depleted from the quantum well if the distance is small (c). Saturated metallic behavior is obtained only for capping layers thicker than 10 nm (a).

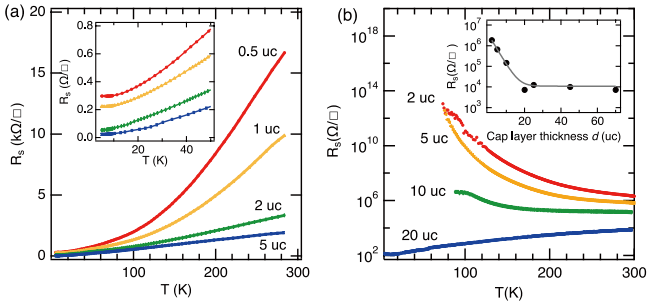

Fig. 2. Variation of the sheet resistance of $SrTiO_3/LaTiO_3/SrTiO_3$ heterostructures with the $LaTiO_3$ delta-doping layer thickness (a) and $SrTiO_3$ capping layer thickness (b). Layer thicknesses are given in unit cells (4Å).

layer thickness drops below 4 nm (10 unit cells). Above 10 nm capping thickness, surface depletion no longer affects the carrier density in the quantum well and the carrier density is set by the number of La atoms in the delta-doping layer. The built-in carrier density in the quantum well is thus set by two layer thickness parameters that are easy to control with precision in the growth process. When the heterostructures are formed into gated field-effect transistors, additional fine-tuning of the carrier density over a narrow range is possible by applying a suitable gate voltage. The electrostatically-gated heterostructure devices are thus particularly well suited for studying filling-dependent Lifshitz transitions, i.e. varying the Fermi energy in the quantum well across the Ti 3*d* conduction band $d_{xz,yz}$ - d_{xy} level crossing.

The effects of the doping and capping layer thicknesses on the transport behavior of the heterostructures are shown in Fig. 2. When a thick capping layer is used and the surface depletion effect can be ignored, metallic conductivity is obtained from the LaO_x layer coverage exceeds about 0.3 monolayers and a gradual reduction of the sheet resistance is observed as the La coverage is increased. For a single unit cell of $LaTiO_3$, the quantum well carrier density was on the order of 10^{13} cm^{-2}. In all cases, however, the Hall resistance was nonlinear, indicating that a significant depth distribution of carriers exists. Approximately 1/4 of the carriers are distributed to a distance of 10 nm or more from the interface. These 'deep' carriers do not suffer from interfacial scattering and reach a mobility of over 10^4 cm^2/Vs at 4K.

The built-in carrier concentration can be further adjusted by changing the cap layer thickness, as shown in Fig. 2b. As the cap layer thickness is reduced to 10 unit cells or less, the heterostructures become semiconducting and finally insulating. These experiments show that it is possible to tune the carrier density continuously close to the lowest densities where metallic conductivity can be sustained.

Reference

[1] J. N. Lee, X. Hou, R. Takahashi, and M. Lippmaa, Appl. Phys. Lett. **116**, 171601 (2020).

Authors
J. Lee, X. Hou, R. Takahashi[a], and M. Lippmaa
[a]Nihon University

Sandwich Structure Formation of BN-Covered Silicene on ZrB_2/Si(111) by Adsorption of NO and Thermal Processes

Yoshinobu Group

Atomic layer materials have attracted much attention in physics, chemistry and materials science. Silicene is a silicon analogue of graphene. A honeycomb silicene layer has been prepared on suitable substrates such as Ag, ZrB_2, Ir, ZrC surfaces. It has been reported that a silicene layer grown on these metallic surfaces has relatively strong interaction with the substrate because of the orbital mixing between metal bands and Si sp-bands. Towards the functionalization of silicene for device applications, several theoretical and experimental investigations have been carried out concerning the interaction between the silicene and other atoms/molecules. Here, we investigated the adsorption and thermal reaction processes of NO with the a silicene monolayer on the ZrB_2/Si(111) substrate using synchrotron radiation X-ray photoelectron spectroscopy (SR-XPS) and density-functional theory (DFT) calculations. SR-XPS experiments were carried out at BL13 of KEK-PF.

Figure 1 shows a series of O 1s, N 1s, Si 2p and B 1s XPS spectra of these processes. The initial surface is a clean silicene monolayer on ZrB_2/Si(111) (see each XPS for the clean surface). NO is dissociatively adsorbed on the silicene surface at 300 K. At an early stage of NO exposure, an atomic nitrogen is bonded to three Si atoms most probably by a substitutional adsorption with a Si atom of silicene (N≡Si_3). An atomic oxygen is inserted between two Si atoms of the silicene (Si-O-Si). After a large amount of NO exposure (1500 L), the two-dimensional honeycomb silicene structure becomes destroyed judging from the decay of typical Si 2p spectra for silicene (see Fig. 1c). The oxidation state of Si becomes Si^{4+} predominantly and the XPS peaks

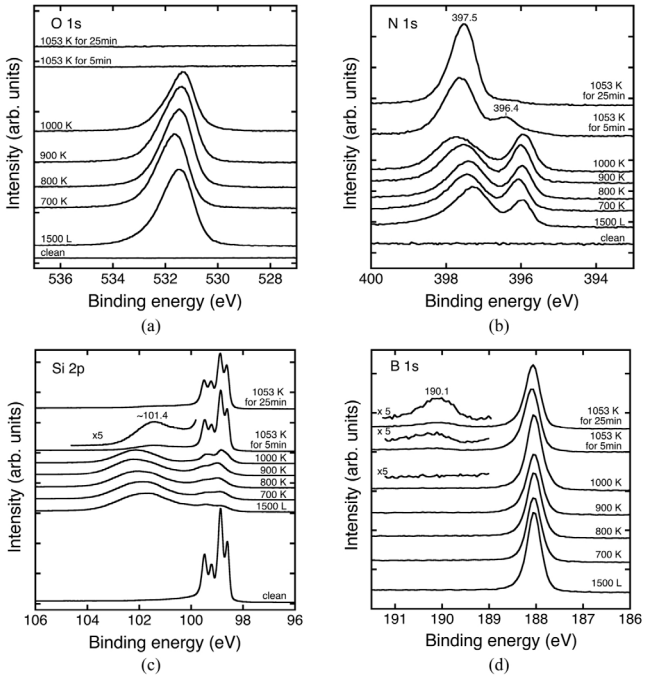

Fig. 1. A series of XPS spectra of the 1500 L NO/silicene/ZrB_2/Si(111) surface as a function of heating temperature. (a) O 1s spectra (hn = 700 eV), (b) N 1s spectra (hn = 560 eV), (c) Si 2p spectra (hn = 260 eV), and (d) B 1s spectra (hn = 700 eV). After quick heating to each temperature, the sample was cooled down to room temperature, and XPS measurements were carried out. Note that at 1053 K, the heating duration time was 5 min and 25 min.

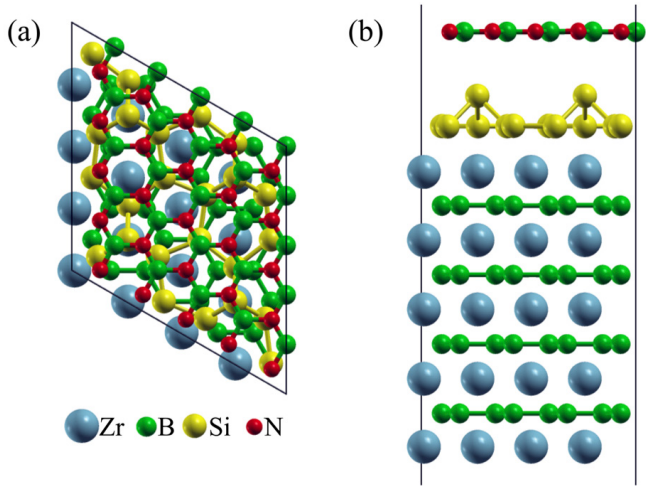

Fig. 2. (a) top view and (b) side view of the optimized structure of a sandwich structure of a hexagonal BN sheet on the silicene/ZrB_2 substrate

of ZrB_2 substrate are decreased in intensity, indicating that complicated silicon oxinitride species have developed three-dimensionally on the ZrB_2/Si(111) substrate at 300 K. By heating above 900 K, the oxide species start to desorb from the surface probably as SiO, but nitrogen-bonded species still exist (Figs. 1a and 1b). After heating at 1053 K for 5 min., no oxygen species is observed on the surface (Fig. 1a); SiN species are temporally formed as a metastable species and BN species also start to develop (Fig.1b). In addition, the silicene structure is partly restored on the ZrB_2/Si(111) substrate (Fig. 1c).

After the prolonged annealing at 1053 K for 25 min., the XPS spectra show a single peak at 397.5 eV for N 1s (Fig. 1b) and an emerging peak at 190.1 eV for B 1s state (Fig. 1d). Since the B 1s peak at 190.1 eV can be ascribed to the B atom in the hexagonal BN structure according to the reference XPS spectra of BN, we conclude that the hexagonal BN structure has developed on the silicene on ZrB_2. By DFT calculations, the geometrical structure has been optimized as shown in Fig. 2; a hexagonal BN sheet weakly interacts with the silicene layer on the ZrB_2 substrate. The calculated binding energy of the N 1s state in the hexagonal BN is 397. 61 eV on average, while there is a variation of the binding energies depending on the relative position of N atoms with respect to the Si atoms of silicene, and the minimum and maximum binding energies are 397.41 and 397.81 eV, respectively. The good agreement between the experimental and calculated binding energies supports the formation of the hexagonal BN structure after the prolonged annealing at 1053 K. Thus, the sandwich structure of BN-covered silicene on the ZrB_2/Si(111) substrate is formed by adsorption of NO at 300 K and prolonged heating at 1053 K.

Reference
[1] J. Yoshinobu *et al.*, J. Chem. Phys. **153**, 064702 (2020). doi: 10.1063/5.0011175

Authors
J. Yoshinobu, K. Mukai, T. Ozaki, Y. Yamada-Takamura[a] *et al.*
[a]Japan Advanced Institute of Science and Technology

Functional Characterization and Study on the Molecular Mechanism of Ion-transporting Rhodopsins

Inoue Group

Rhodopsin is photo-receptive heptahelical transmembrane protein in which a retinal chromophore is covalently bound to a conserved lysine residue in the seventh transmembrane helix (TM7), and animal and microbial rhodopsin families are known so far. Animal rhodopsins are present in animal retina to transfer visual signals to brain and are also related to non-visual light sensing in various tissues. Microbial rhodopsins show diverse functions: light-driven ion pump, light-gated ion channel, phototactic sensor, light-dependent regulation of gene expression and enzyme, and so on. Both types of rhodopsins are being widely used in optogenetics to control various cellular events, such as neural activity, gene expression, dynamic protein localization, and so on, by light.

In 2020, we reported the functional characterization of schizorhodopsin (SzR) which was found in metagenome assembled genomes of Asgard archaea which is thought to be the closest living prokaryote to the last common ancestor of eukaryotes [1]. The ion-transport activity assays revealed that SzRs function as light-driven inward proton (H^+) pumps [2]. The inward H^+ transport of SzRs are significantly higher than that of another inward H^+ pumping rhodopsin, xenorhodopsins (Fig. 1). The high-speed atomic force microscopy revealed the trimeric structure of SzR in lipid bilayer. The photocycle of SzR in which K, L, L/M and M intermediates are included was determined by the laser flash photolysis spectroscopy. The transient absorption change of a pH indicator (cresol red) indicated that the substrate H^+ is released to the cytoplasmic milieu and taken up from the extracellular side on the M-accumulation and decay, respectively. This suggests that no metastable trapping of H^+ released from retinal Schiff base (RSB) occurs on any amino acid residues, and it was supported by the low-temperature Fourier transform infrared spectroscopy. This is quite

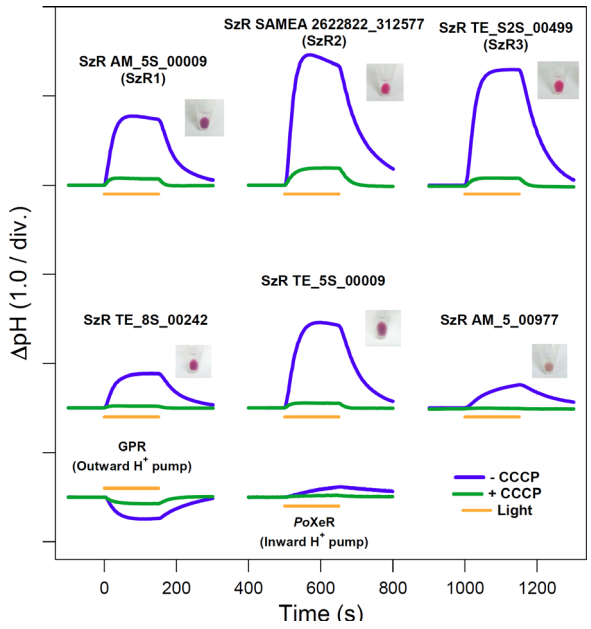

Fig. 1. Inward H^+ transport activity of six SzRs (top and middle) compared with outward H^+ pumping GPR and inward H^+ pumping XeR (*Po*XeR) (bottom).

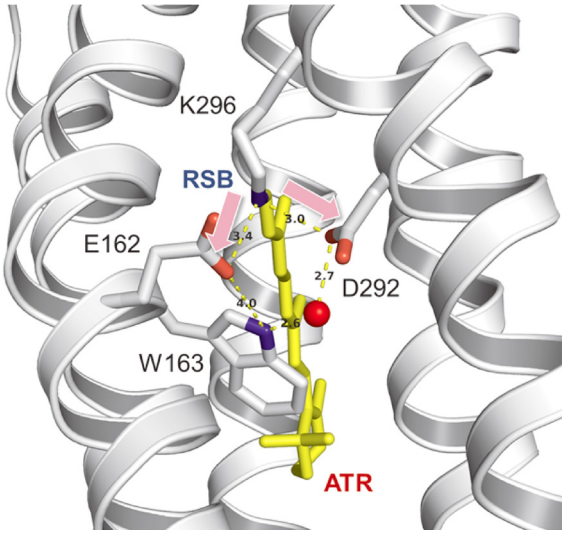

Fig. 2. Trp163 of C1C2 plays a role regulating the branching ratio of H^+ transfers between RSB and counterions, Glu162 and Asp292.

different from XeR, in which protonation of the proton accepting aspartate on the cytoplasmic side is involved in H^+ transfer from the RSB to the cytoplasmic milieu. A comprehensive amino-acid mutation experiment suggested that Cys75 and Glu81 in the transmembrane helix (TM) 3 and Asp184 in TM7 is critical for the inward H^+ transport of SzR.

Channelrhodopsins (ChRs) are light-gated cation channels which nonspecifically transports various cations according to the electrochemical potentials of cells. In order to reveal the cation transport function of ChR, we investigated a mutant of a member of ChR, C1C2, in which a tryptophane residue in TM3 was substituted with phenylalanine (C1C2 W163F). Trp163 of C1C2 is highly conserved in most microbial rhodopsins, but its relationship to the channel function is not known. C1C2 W163F showed greatly attenuated channel activity, while outward proton pumping activity became more prominent. This result indicates that Trp163 plays a critical role in suppressing the outward proton pumping function and increasing channel activity by regulating the branching ratio of proton transfer to the two counterions Glu162 and Asp292 respectively (Fig. 2) [3].

We also reported the theoretical and experimental studies on the Cotton effect observed in the visible CD spectrum of sodium pump rhodopsin (KR2) [4]. KR2 shows a visible CD spectrum whose peak is significantly red-shifted from that of its absorption spectrum. The transition density fragment interaction (TDFI) method quantitatively revealed that this shift is caused by the excitonic coupling between retinal chromophores in pentamer of KR2 [4].

References

[1] P.-A. Bulzu, A.-Ş. Andrei, M. M. Salcher, M. Mehrshad, K. Inoue, H. Kandori, O. Béjà, R. Ghai, and H. L. Banciu. Nat. Microbiol. **4**, 1129 (2019)

[2] K. Inoue, S. P. Tsunoda, M. Singh, S. Tomida, S. Hososhima, M. Konno, R. Nakamura, H. Watanabe, P.-A. Bulzu, H. L. Banciu, A.-Ş. Andrei, T. Uchihashi, R. Ghai, O. Béjà, and H. Kandori, Sci. Adv. **6**, eaaz2441 (2020)

[3] Y. Nagasaka, S. Hososhima, N. Kubo, T. Nagata, H. Kandori, K. Inoue, and H. Yawo. Biophys. Physicobiol. **17**, 59 (2020)

[4] K. J. Fujimoto and K. Inoue, J. Chem. Phys. 153, 045101 (2020).

Authors

K. Inoue, T. Nagata, H. Yawo

Omnidirectional Control of Large Electrical Output in a Topological Antiferromagnet

Nakatsuji Group

The net magnetization defines the signal size of memory devices and sensors, and thus the manipulation of magnetization is essential for the broad application of ferromagnets. However, the magnetization itself causes a dilemma. While its size matters to obtain strong responses upon its reversal, the large magnetization simultaneously suppresses the range of its directional control due to the demagnetizing field. To overcome the demagnetization/shape barrier, one needs to carefully tune the crystalline and interfacial effects [1]. Thus, it would be ideal to find alternative magnets that carry no magnetization but strong responses.

The antiferromagnet Mn_3Sn hosts a large Berry curvature in momentum space owing to the topological metallic state. The Berry curvature can be manipulated by the ferroic ordering of the cluster magnetic octupole and remains large even with negligible magnetization. This feature enables disproportionately large transverse responses such as anomalous Hall effect (AHE)[2] and anomalous Nernst effect

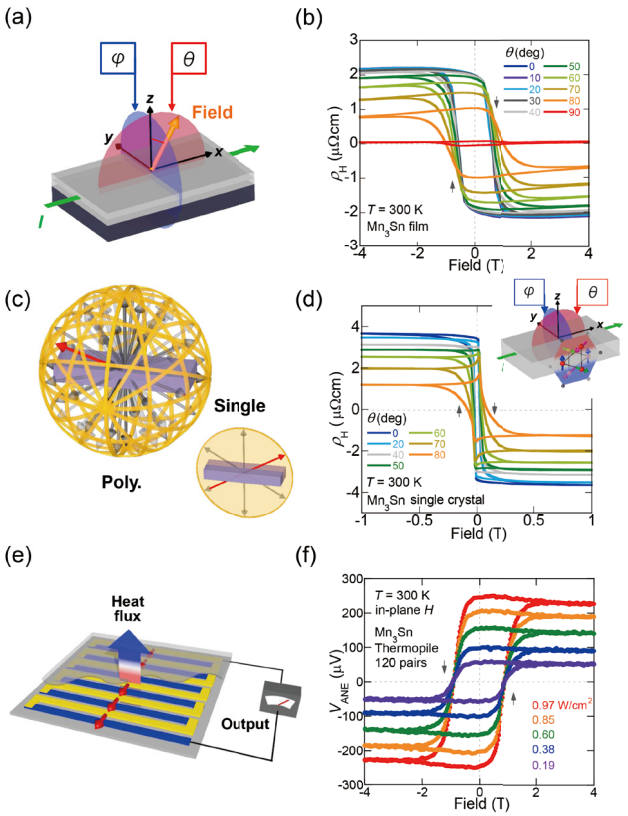

Fig. 1. (a) Schematic illustration of the rotation planes. θ and φ are the angles from the normal direction within the planes parallel and perpendicular to the electric current direction, respectively. The orange arrow represents the direction of the external magnetic field. (b) Field dependence of the Hall resistivity obtained for the Mn_3Sn film with various angles θ at 300 K. The black arrows indicate the field sweep direction. (c) Schematic illustrations ofthe 3D omnidirectional property for randomly oriented multi-grains and the 2D omnidirectional property for a single crystal/grain. The red arrow represents the direction of the magnetic order parameter. (d) Field dependence of the Hall resistivity obtained for the Mn_3Sn single crystal with various angles θ at 300 K. Inset: Schematic illustrations of the rotation planes for the single crystal. (e) Schematic illustration of heat flux sensor. (f) Field dependence of the Nernst voltage V_{ANE} for the Mn_3Sn thermopile made of 120 pairs of Mn_3Sn/Au wires under several values of the heat flux q_{heater} at 300 K.

(ANE)[3], opening up the possibilities for replacing ferromagnets with antiferromagnets in magnetic devices. As the first step for spintronics applications, we fabricated Mn_3Sn thin films [4]. And more recently, we demonstrated electrical manipulation of the magnetic ordering in the Mn_3Sn /heavy metal bilayer devices [5], which has triggered extensive research activities into the interface properties of Mn_3Sn thin film.

In this study [6], we report the omnidirectional behavior in Mn_3Sn due to negligible shape anisotropy. Moreover, we demonstrate a new method for multi-level data recording and a magnetically robust ANE-type heat flux sensor.

We have fabricated the polycrystalline Mn_3Sn thin films on the thermally oxidized Si substrate by dc magnetron sputtering methods [4]. With these thin films, we measured the anomalous Hall effect as a function of magnetic field angles, θ and ϕ (Fig. 1(a)). As shown in Fig. 1(b), the field dependence of AHE obtained for various θ exhibits a multi-stable signal. Namely, the spontaneous Hall signal gradually decreases with increasing θ, indicating that the polarization direction of the magnetic octupole essentially follows the field direction rather than being restricted within the *xy* plane. Notably, the rotation for both θ and ϕ angles shows the same angular dependence, indicating that the magnetic octupole can be freely (omnidirectionally) orientated in all directions (Fig. 1(c)) as a result of the negligibly small shape anisotropy and polycrystalline arrangement.

Interestingly, single-crystal/grain samples also show the multi-stable signals as a function of the field angle, but only for field rotations within the kagome layer (Fig. 1(d)). Ferromagnets with magneto-crystalline anisotropy sufficiently larger than the shape anisotropy can show similar multi-stable behavior in their polycrystalline form. However, in the single crystal samples, the magnetization is restricted to one direction due to the substantial magneto-crystalline anisotropy, and therefore only a binary signal can occur. The new multi-level recording method found in Mn_3Sn may allow writing and reading beyond two units of information (0 and 1), namely, a device comprising a single grain of nanometer scale can hold three or more units of information.

Taking advantage of the small shape anisotropy and the omnidirectional property, we developed a ANE heat flux sensor consisting of micro-fabricated Mn_3Sn wires (Fig. 1(e)). This sensor exhibits the heat flux sensitivity comparable to that made of ferromagnetic materials while being resistant to magnetic field disturbances (Fig. 1(f)).

References

[1] R. Skomski and J. M. D. Coey, Scr. Mater. **3**, 112 (2016).
[2] S. Nakatsuji *et al*., Nature **527**, 212 (2015).
[3] M. Ikhlas, T. Tomita *et al*., Nat. Phys. **13**, 1085 (2017).
[4] T. Higo *et al*., Appl. Phys. Lett. **113**, 202402 (2018).
[5] H. Tsai, T. Higo *et al*., Nature **608**, 580 (2020).
[6] T. Higo *et al*., Adv. Funct. Mater. 31, 2008971 (2021).

Authors

T. Higo, Y. Li[a], K. Kondou[b], D. Qu, M. Ikhlas, R. Uesugi, D. Nishio-Hamane, C. L. Chien[a], Y. Otani, and S. Nakatsuji
[a]Johns Hopkins University
[b]RIKEN-CEMS

Large Hall Signal due to Electrical Switching of an Antiferromagnetic Weyl Semimetal State

Nakatsuji, Otani, and Miwa Groups

The topologically protected properties in Weyl semimetals have been extensively studied in recent years. The Weyl points act as sources and drains of Berry curvature, leading to significant responses such as anomalous Hall effect (AHE) and anomalous Nernst effect (ANE) [1-3]. In nano-scale technology, such large topological responses may play a significant role in developing next-generation electronic devices.

Recently, the electrical manipulation of the topological state has been demonstrated in antiferromagnetic Weyl semimetal Mn_3Sn [4]. Mn_3Sn is a metallic antiferromagnet with the hexagonal D019 structure and ABAB-stacking of Mn kagome lattice along [0001]. The geometrical frustration leads to a 120-degree structure made of Mn magnetic moments with a negative vector chirality (Fig 1(a)). This non-collinear structure can be viewed as a ferroic order of a cluster magnetic octupole made of six neighboring Mn moments. The polarization of the magnetic octupole determines the distribution of Weyl points in momentum space and thus the polarity of AHE (Fig 1(b)). Figure. 1(c) shows the schematic image of the current switching in Mn_3Sn/heavy metal heterostructures. Taking Mn_3Sn/W as an example, with an applied electrical current in the multilayer, a spin current generated by the spin Hall effect in the W

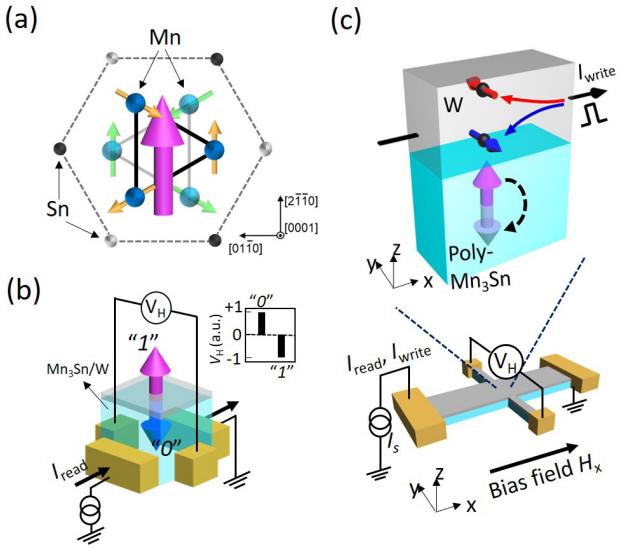

Fig. 1. (a) Crystal and spin structures of Mn_3Sn. Blue and light blue spheres represent Mn atoms on the kagome bilayers, forming an octahedron. Black and gray spheres represent Sn atoms. The noncollinear spin structure consisting six Mn magnetic moments (yellow and green arrows) can be viewed as a ferroic ordering of an magnetic octupole (purple arrow). (b) Hall voltage measured in Mn_3Sn/W devices. The sign of readout voltage is determined by the out-of-plane component in the polarization direction of the magnetic octupole of Mn_3Sn (purple and blue arrows), namely, "*0*" or "*1*" state. (c) Bottom: Schematic image of Mn_3Sn/heavy metal devices and the setup of electrodes. The samples are fabricated in 16 μm × 96 μm Hall bar structure with Au/Ti electrodes. Top: Schematic image of the current switching in Mn_3Sn/W bilayer. An electrical current flowing in the W layer generates a spin current by the spin Hall effect of W. This spin current induces a spin-orbit torque in the Mn_3Sn layer and switch the polarization direction of the magnetic octupole. Here, red and blue thin arrows represent the spin moments of the spin current. Purple and light purple thick arrows represent the polarization direction of the magnetic octupole.

layer exerts the spin-orbit torque on the Mn_3Sn spin texture, causing the switching of the polarization direction of the magnetic octupole. This manipulation of AHE enables us to store the information from the electrical signal, "*0*" or "*1*" state, into the magnetic octupole of Mn_3Sn. Thus, Mn_3Sn can work as a non-volatile memory, in which the information can be written and read by current. Moreover, the antiferromagnetic structure of Mn_3Sn allows electronic devices with higher density and computing speed than those made of conventional ferromagnets [5]. For applications, it is essential to enhance the readout signal of the switching. This study demonstrates that the switching signal of Mn_3Sn can grow dramatically by adjusting the crystal orientation and interface condition of the Mn_3Sn/heavy metal structures. Moreover, by increasing the read current, the readout voltage may go well beyond 1 mV, a milestone for future memory technology.

To find the largest readout signal, we prepared four different multilayer stacks: (i) Ru(2)/Mn_3Sn(40)/Pt(5), (ii) Mn_3Sn(40)/Pt(5), (iii) Ru(2)/Mn_3Sn(40)/W(5), and (iv) Mn_3Sn(40)/W(5), all units in nm, deposited on a Si/SiO_2 substrate. For the sample (i)-(iii), the stacks are annealed at 450 °C for 0.5 h after the fabrication of the Mn_3Sn layer. The samples (iv) Mn_3Sn(40)/W(5) is annealed at 450 °C for 0.5 h after the fabrication of the W layer. Using these thin films, a Hall bar structure (16 μm × 96 μm) is fabricated, with Ti/Au electrodes attached (Fig 1(c)). Figure. 2(a) shows the AHE signal in W devices with and without the Ru layer. By removing the Ru layer, the AHE becomes 1.6 times larger than that observed in devices with the Ru layer. Similar enhancement of the AHE also occurs in Pt devices. This enhancement comes from the crystal orientation change of Mn_3Sn. The X-ray diffraction analysis shows that the kagome plane of Mn_3Sn tends to align in-plane in the presence of the Ru underlayer. After removing the Ru layer, Mn_3Sn layer becomes completely polycrystalline. The out-of-plane component of the magnetic octupole is more than one with the Ru layer, resulting in a larger AHE. Next, we investigated the electrical switching in W devices. In these experiments, both electrical current and bias field are applied along the longitudinal direction (*x*-direction) and the transverse Hall voltage V_H is detected in the *y*-direction, as shown in Fig. 1(c). A strikingly large switching Hall voltage, $\Delta V_H^{current}$ ~70 μV, is observed in Mn_3Sn/W devices (Fig. 2(b)). This Hall signal is 3 times larger than that observed in the Ru/Mn_3Sn/W devices, more pronounced than the 1.6 times difference of the AHE caused by removing the Ru layer. We attribute this enhancement in current switching to the different annealing process because only the Mn_3Sn/W samples is once annealed after the W deposition. This additional annealing process may affect the interface condition. Finally, since the Hall voltage is proportional to the read current within a suitable temperature range, we tried to enhance the read current to maximize the readout signal (Fig. 2(c)). We found that the readout switching Hall voltage ΔV_H can exceed 1 mV when applying 3 mA read current. This observed mV order Hall voltage is a significant advance in the electrical switching technology, and our results may pave the path for designing a new type of memory device using the robust topological properties of Weyl antiferromagnets.

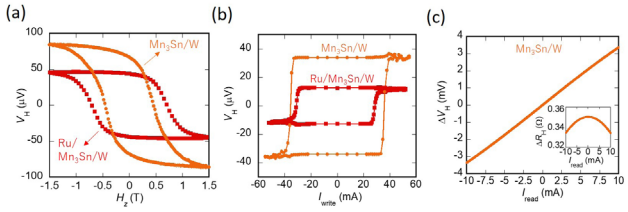

Fig. 2. (a) Hall voltage V_H as a function of a perpendicular magnetic field H_z for Ru/Mn_3Sn/W and Mn_3Sn/W devices, respectively. (b) V_H as a function of the write-current I_{write} under a bias field $\mu_0 H_x$ = 0.1 T applied along the electrical current direction for Ru/Mn_3Sn/W and Mn_3Sn/W devices, respectively. (c) Switching Hall voltage ΔV_H as a function of the read current I_{read} in the Mn_3Sn(40)/W(5) sample. Inset: Hall resistance ΔR_H as a function of the read current I_{read}.

References

[1] H. B. Nielsen and M. Ninomiya, Phys. Lett. B, **130**, 389 (1983).
[2] S. Nakatsuji, N. Kiyohara, and T. Higo, Nature, **527**, 212 (2015).
[3] M. Ikhlas, T. Tomita, T. Koretsune, M. Suzuki, D. Nishio-Hamane, R. Arita, Y. Otani, and S. Nakatsuji, Nat. Phys. **13**, 1085 (2017).
[4] H. Tsai, T. Higo, K. Kondou, T. Nomoto, A. Sakai, A. Kobayashi, T. Nakano, K. Yakushiji, R. Arita, S. Miwa, Y. Otani, and S. Nakatsuji, Nature **580**, 608 (2020).
[5] T. Jungwirth *et al.*, Nat. Nanotechnol. 11, 231 (2016).

Authors

H. Tsai, T. Higo, K. Kondou[a], S. Sakamoto, A. Kobayashi, T. Matsuo, S. Miwa, Y. Otani, and S. Nakatsuji

[a]RIKEN, Center for Emergent Matter Science (CEMS)

A Tunable Stress Dilatometer and Measurement of the Thermal Expansion under Uniaxial Stress of Mn_3Sn

Nakatsuji Group

The hexagonal antiferromagnet Mn_3Sn with triangular spin structure exhibits large spontaneous electronic responses associated with Weyl fermions [1], which has attracted tremendous attention due to its potential for spintronic applications [2]. The single crystals of this compound are known to be stable in their off-stoichiometric compositions. Depending on the composition, three distinct kinds of magnetic phases can emerge as a function of temperature, namely the high-temperature triangular spin structure phase ($\mathbf{q}$ = 0) [3], the intermediate-temperature incommensurate spin spiral phase ($\mathbf{q} \neq 0$) [4], and the low-temperature cluster spin glass phase [5]. The topological transport properties vanish in the incommensurate phase, whose origin remains elusive. A theoretical study suggests that out-of-plane antiferromagnetic exchange interaction may destabilize the triangular spin structure [6].

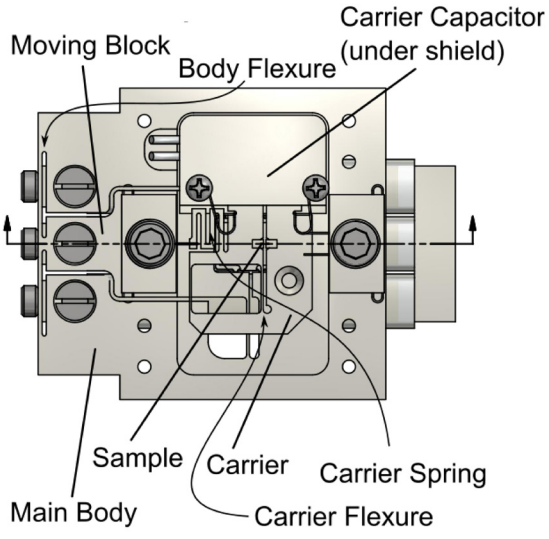

Fig. 1. Uniaxial stress dilatometer

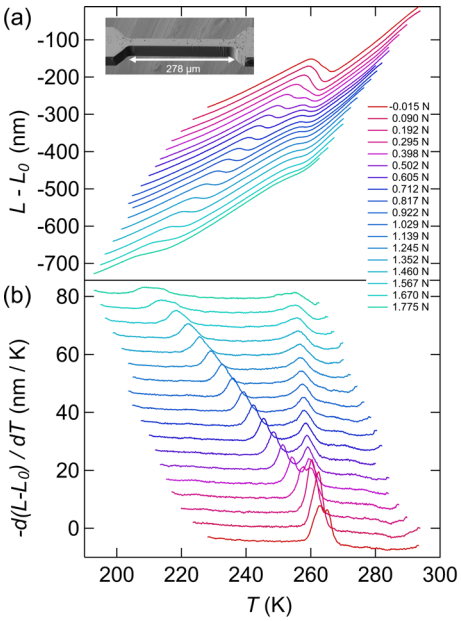

Fig. 2. Thermal expansion of Mn_3Sn under uniaxial pressure. (a) Sample's *c*-axis length change L-L_0 vs. temperature under various applied uniaxial forces. Inset shows the sample used for the measurements. (b) Derivative of *c*-axis length change -d(L-L_0)/dT vs. temperature (bottom panel) under various applied uniaxial forces.

A long-wavelength incommensurate spin structure can originate from various mechanisms, such as competition between short-range and long-range exchanges in CeSb [7], and Fermi surface nesting in hexagonal rare-earth elemental metals [8]. In the latter case, Fermi surface nesting is largely determined by the lattice constant ratio c/a, which is tunable by alloying or uniaxial pressure. Uniaxial pressure is a clean tuning parameter compared to chemical doping. Here, we explore the evolution of the magnetic phase diagram of Mn_3Sn under *c*-axis uniaxial pressure.

In collaboration with Dr. Clifford Hicks and Dr. Kent Shirer from Max Planck Institute for Chemical Physics of Solids (MPI CPfS), Dresden, Germany, we developed a piezoelectric-based uniaxial stress dilatometer that provides *in-situ* stress tunability, as shown in Fig 1. This device allows high-sensitivity thermal expansion measurements, offering a compelling route to thermodynamic information on magnetic phase evolution under large and homogenous applied stress. The sample is sculpted into a paddle using a focused ion beam and then epoxied across the central gap of the sample carrier, as seen in the inset of Fig 1a. Applying voltage to the piezo stacks displaces a spring and delivers uniaxial stress to the sample, while the sample's length change was estimated from the displacement of the parallel plate capacitor attached to the carrier.

Figure 2a shows the temperature dependence of *c*-axis length change L-L_0 of Mn_3Sn at various applied uniaxial forces. At zero force, the sample exhibits a first-order transition from triangular to spiral spin structure on cooling below T_H = 267 K, accompanied by a discontinuity in L-L_0. Under uniaxial force, the transition splits into two, as shown in Fig. 2b. The peak in $-d\Delta L/dT$ that shifts to lower temperatures with an increasing uniaxial force corresponds to the response of the central narrow portion of the sample. With an elastic compressive stress of σ_z ~-1.5 GPa, the transition is suppressed by ΔT ~ -50 K. Below -σ_z ~ 0.5 GPa, T_H has a linear dependence on σ_z, with $\partial T_H/\partial\sigma_z$ = 33.3 K at zero stress. We estimate an entropy change of ΔS ~ 0.1 mJ mol^{-1} K^{-1} from Clausius-Clapeyron relation, using the magnitude of the discontinuity in ΔL and $\partial T_H/\partial\sigma_z$. This value of ΔS is consistent with that estimated from heat capacity data. Above -σ_z ~ 0.5 GPa, $\partial T_H/\partial\sigma_z$ does not deviate appreciably from its ambient pressure value; this information cannot be extrapolated solely based on the zero pressure $\partial T_H/\partial\sigma_z$. Overall, we found that the transition is insensitive to stress compared with its response to chemical doping, suggesting that the lattice is not the primary driver of the transition. This device is compatible with other probes, such as transport and spectroscopy, opening a new avenue to study phases of matter under extreme conditions [9].

References

[1] T. Chen, T. Tomita, S. Minami, M. Fu *et al.,* Nat. Comm. **12**, 572 (2021).
[2] H. Tsai, T. Higo *et. al*., Nature **580** (2020).
[3] T. Nagamiya, S. Tomiyoshi, and Y. Yamaguchi, Solid State Commun. **42** (1982).
[4] J.W. Cable *et. al*., Solid State Commun. **88** (1983).
[5] W. J Feng, D. Li *et. al*., Phys. Rev. B **73** (2006).
[6] S. Dasgupta and O. Tchernyshyov, Phy. Rev. B **102** (2020).
[7] M. E. Fischer and W. Selke, Phys. Rev. Lett. **44** (1980).
[8] A. Andrianov *et. al*., Phys. Rev. B **62** (2000).
[9] M. Ikhlas, K. Shirer *et. al.*, Appl. Phys. Lett. **117** (2020).

Authors

M. Ikhlas, K. Shirer[a], P.-Y. Yang[a], A. P. Mackenzie[a], C.W. Hicks[a], and S. Nakatsuji

[a]Max Planck Institute for Chemical Physics of Solids

Large Transverse Thermoelectric Effect in Iron-Based Binary Ferromagnets

Nakatsuji and Miwa Groups

Thermoelectricity provides vital technology for versatile energy harvesting and heat current sensors. So far, thermoelectric technologies are focused on the longitudinal Seebeck effect. Its transverse counterpart, the anomalous Nernst effect (ANE), has recently gained significant attention, owing to several potential benefits [1,2]. Namely, the transverse geometry of the Nernst effect enables simplified structures of thermoelectric generators with enhanced conversion efficiency once the suitable materials become readily available. Moreover, the transverse geometry is hypothetically better suited for thermoelectric conversion, as the Ettingshausen heat current should support the Nernst voltage while the Peltier heat current may suppress the Seebeck voltage [3]. A server obstacle here is that the anomalous Nernst effect is too small compared to the Seebeck effect for real-life thermoelectric applications. Thus, it is essential to design a new class of materials that exhibit a large ANE without an external magnetic field.

To find candidate compounds efficiently, we carried out a high-throughput calculation to screen materials and found two candidate iron-based cubic compounds, Fe_3X (X = Ga,

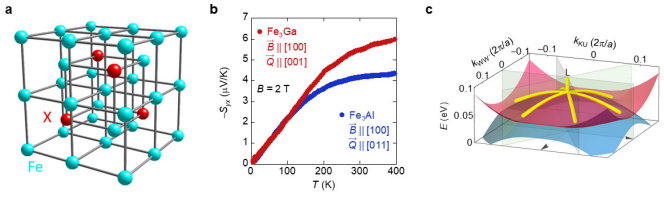

Fig. 1. (a) Crystal structures of Fe_3X (X = Ga, Al) (b) Temperature dependence of the Nernst signal $-S_{yx}$ in Fe_3X (X = Ga, Al) under a [100] magnetic field of 2T. (c) The nodal web in momentum space formed by nodal lines (yellow) of nearly flat energy dispersion around the L point.

Al) (Fig. 1a). We discovered record high spontaneous transverse thermoelectric effects at room temperature in these materials, reaching about 6 μVK^{-1} in Fe_3Ga and 4 μVK^{-1} in Fe_3Al (Fig. 1b). We then succeeded in fabricating Fe_3Ga and Fe_3Al thin films that display an ANE of about 4 μVK^{-1} and 2 μVK^{-1} at room temperature with an applied in-plane temperature gradient. For an out-of-plane temperature gradient, these thin films exhibit a zero-field ANE, with a coercivity B_C of the in-plane magnetization being about 40 Oe in Fe_3Ga and 20 Oe in Fe_3Al, respectively. These features are suitable for designing low-cost, flexible thermoelectric generators.

The comparison between experiment and theory indicates that the Fermi energy tuning to the nodal web is the key to the substantial enhancement in the transverse thermoelectric coefficient. Figure 1(c) shows a schematic of the nodal web, a flat band structure made of interconnected nodal lines. The Berry curvature is particularly enhanced at the momenta connecting the edge of the nodal web around the L point at the Brillouin zone boundary, extending over a quasi-2D area spanned by the web. The strongly enhanced Berry curvature occurs near the momenta originally belonging to the flat nodal web, such as the one around the L point.

Our innovative iron-based thermoelectric material represents a significant step toward commercializing thermoelectric generators that can power small devices such as remote sensors or wearable devices. It is vital to enhance the coercivity further to achieve stable performance in daily use. Finally, it would be an interesting future direction to look for an enhanced output by combining the ANE with the spin Seebeck effect, both of which occur in the same transverse geometry. [4]

References

[1] A. Sakai *et al*., Nat. Phys. **14**, 1119 (2018).
[2] M. Ikhlas, T. Tomita *et al*., Nat. Phys. **13**, 1085 (2017).
[3] M. Mizuguchi, and S. Nakatsuji, Sci. Technol. Adv. Mater. **20**, 262 (2019).
[4] A. Sakai, S. Minami, T. Koretsune, T. Chen, T. Higo *et al*., Nature **581**, 53 (2020).

Authors

A. Sakai, S. Minami[a], T. Koretsune[b], T. Chen, T. Higo, Y. Wang, T. Nomoto[c], M. Hirayama[d], S. Miwa, D. Nishio-Hamane, F. Ishii[a], R. Arita[c,d], and S. Nakatsuji

[a]Kanazawa University
[b]Tohoku University
[c]University of Tokyo
[d]RIKEN CEMS

Electrical Manipulation of a Topological Antiferromagnetic State

Nakatsuji, Otani, and Miwa Groups

The Weyl semimetal features nodal points formed by two linearly dispersive non-degenerate bands. These touching points or Weyl nodes act as topologically protected monopoles or antimonopoles of underlying Berry curvature, resulting in large anomalous Hall effect (AHE) and chiral anomaly. The electrical manipulation of Weyl nodes is among the key topics of technological innovation utilizing a novel topological state. Moreover, electrical manipulation of an antiferromagnetic Weyl metal is considered a significant advancement, given the prospects of antiferromagnetic (AF) spintronics for realizing high-density, ultrafast devices [1].

We demonstrate the electrical switching of the AF Weyl state using Mn_3Sn/nonmagnetic metals (NM = Pt, W, Cu) bilayer devices and the spin-orbit torque (SOT) switching method [5]. The inverse triangular spin structure of Mn_3Sn can be viewed as a ferroic ordering of cluster magnetic octupoles. The magnetic octupole's polarization direction determines the location of Weyl nodes and the associated distribution of the Berry curvature in the momentum space (Fig. 1(b) right) [2]. With an electrical current applied to the Pt layer, a spin polarized current generated by the spin Hall effect of Pt induces the SOT on the Mn_3Sn layer and causes the switching of the polarization direction of the magnetic octupole (Fig. 2a). The measurement configuration and optical micrograph of the fabricated bilayer Hall bar devices are shown in Fig. 2(b). We first perform the magnetic field switching of the Hall voltage V_H by using an out-of-plane magnetic field H_z and a read current of

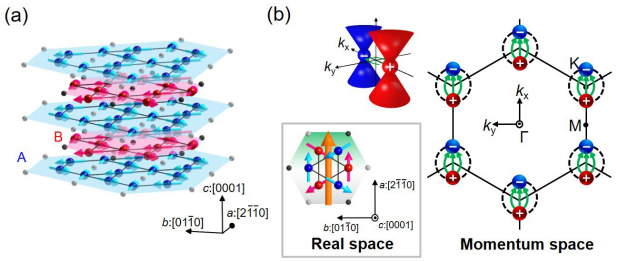

Fig. 1. (a) Mn_3Sn crystal structure and inverse triangular spin (ITS) structure. The Mn magnetic moments (light blue and pink cylindrical arrows) lie within the kagome layer with the ABAB stacking sequence and form the ITS structure at room temperature. This spin structure can be viewed as a ferroic ordering of cluster magnetic octupoles. (b) Bottom-left: cluster magnetic octupole (orange cylindrical arrow) consisting of the six spins on the kagome bilayer. Right: schematic of the Weyl point distribution near the Fermi energy in momentum space (k_X-k_Y plane at k_Z = 0); the corresponding magnetic structure is shown in the left-side figure. The red and blue spheres correspond to Weyl nodes acting as sources (+) and drains (-) of the Berry curvature (green arrows). Inset: three-dimensional schematic of a pair of Weyl nodes.

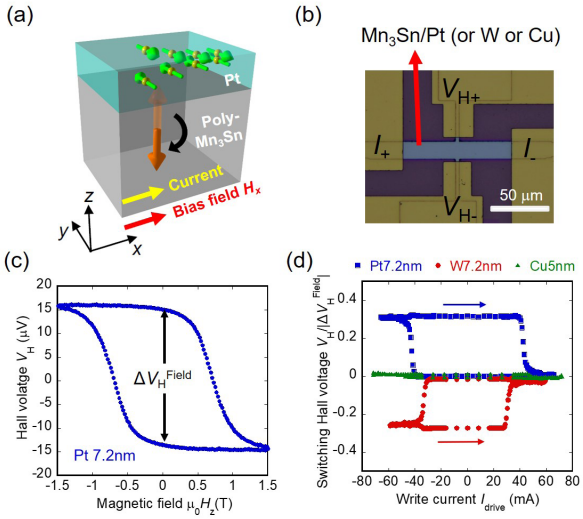

Fig. 2. (a) Schematic image for the spin-orbit torque switching. Under a write current and a bias field along the x-direction, the spin-polarized current in Pt (green cylindrical arrows on yellow spheres) exerts a spin-orbit torque, causing the polarization axis of the cluster magnetic octupole to switch (orange cylindrical arrow) in the polycrystalline Mn_3Sn (b) Measurement configuration and optical micrograph of the Mn_3Sn-nonmagnet bilayer Hall bar devices. (c) Hall voltage V_H vs. magnetic field along the z-direction H_z obtained for the Mn_3Sn/Pt 7.2 nm device at room temperature. (d) Hall voltage V_H vs. write current I_{write} for the Pt 7.2 nm, Cu 5 nm, and W 7.2 nm devices at room temperature. The Hall voltage is normalized by the zero-field Hall voltage $|\Delta V_H^{field}|$ obtained from the magnetic field dependence measurements for each sample.

0.2 mA, and a clear hysteresis of V_H with the zero-field change of ΔV_H^{field} (= $V_H(+H_z \to 0) - V_H(-H_z \to 0)$) is observed (Fig. 2(c)). To examine the possible SOT switching of Mn_3Sn, we pass a 100 ms write-pulse current I_{write} along the x-direction; then, we wait for 600 ms after the pulse current and measure V_H with a 0.2 mA read current. Figure 2(d) shows V_H as a function of I_{write} in Pt, W, and Cu devices. For the NM = Pt (spin Hall angle $\theta_{SH} > 0$) and a bias field H_x parallel to the current direction, a clear negative (positive) jump appeared in the Hall voltage for a positive (negative) current larger than a critical threshold write-current I_c. The magnitude of the jump reaches ~30 % of the total Hall voltage change $|\Delta V_H^{field}|$ in the field sweep measurements. To confirm that the observed switching of V_H is related to the SOT due to the spin Hall effect in the NM layer, we prepared NM = W ($\theta_{SH} < 0$) and Cu ($\theta_{SH} \sim 0$). For NM = W, the switching polarity is opposite to the Pt case, while for NM = Cu, hysteresis is absent with the electrical current cycle. The difference in switching polarity between Pt and W devices and the absences of switching in Cu devices cannot be explained by the current-induced Oersted field but agree well with the sign of θ_{SH} of the NM layer. These results demonstrate that SOT from the NM layer induces the perpendicular switching of the AF domain and thus manipulates the direction of the Weyl nodes.

In recent years, utilizing antiferromagnets in spintronics devices have attracted significant attention as its vanishing small stray fields and much faster spin dynamics than ferromagnets [1]. We achieved the electrical switching of the AF Weyl metal using the same protocol as the one used for ferromagnetic metals [3, 4]. The critical write current density in the NM layer is considerably smaller than that in the NM/FM devices. These results indicate that topological antiferromagnets offer the unmatched potential for spintronic applications that may surpass today's ferromagnetic counterparts [5].

References

[1] T. Jungwirth *et al*., Nat. Nanotechnol. **11**, 231 (2016).
[2] S. Nakatsuji, N. Kiyohara, and T. Higo. Nature **527**, 212 (2015).
[3] I. M. Miron *et al*., Nature **476**, 189 (2011).
[4] L. Liu *et al*. Science **336**, 555 (2012).
[5] H. Tsai, T. Higo, K. Kondou, T. Nomoto, A. Sakai, A. Kobayashi, T. Nakano, K. Yakushiji, R. Arita, S. Miwa, Y. Otani, and S. Nakatsuji, Nature **580**, 608 (2020).

Authors

H. Tsai, T. Higo, K. Kondou[a], Takuya Nomoto[b], A. Sakai, A. Kobayashi, T. Nakano[c], K. Yakushiji[c], R. Arita[a], S. Miwa, Y. Otani, and S. Nakatsuji

[a]RIKEN CEMS
[b]The University of Tokyo
[c]AIST

Weyl-Fermion-Induced Anomalous Transport in the Chiral Antiferromagnets Mn_3X, (X = Sn, Ge)

Nakatsuji Group

The blooming field of spintronics has bridged astonishingly complex antiferromagnetic structures to the realm of energy-efficient memory technologies. However, a significant obstacle to overcome is the tiny response of the antiferromagnetic structure to external magnetic fields [1]. The recent discoveries of large room-temperature anomalous transport effects in antiferromagnets Mn_3X (X = Sn, Ge) [2,3] signifies an experimental breakthrough in this direction, bringing the study on strongly correlated topological phases to the main stage of basic science and technological innovation. These anomalous transport properties are considered fingerprints of Weyl fermions in the momentum-space band structure [4]. Therefore, understanding the role of magnetic Weyl fermions in driving the transport properties of chiral antiferromagnets is all the more important for making real-life applications with topological states of matter.

In this work, we establish Weyl fermions as the origin of the large anomalous Hall and Nernst effects in Mn_3X systems by combining our previous reports with a new, comprehensive set of transport measurements and theoretical analysis of high-quality Mn_3Sn and Mn_3Ge single crystals [5]. In particular, Mn_3Ge provide an ideal experimental platform for identifying transport signatures stemming from Weyl fermions; in this compound, the inverse triangular covers a wide temperature range down to at least 0.3 K, approximately one-thousandth of the Néel temperature. This feature allows a clear-cut detection of the Weyl-fermion-induced transport anomalies at sufficiently low temperatures, where spin fluctuations are essentially suppressed.

The fingerprint of Weyl points in magnetotransport is known as the chiral anomaly. With a magnetic field, the Weyl crossings are quantized into Landau levels (LLs), and the lowest LL are divided into left- and right-movers of opposite chirality. These two groups do not mix, leading to separate number conservation of the three-dimensional left- and right-handed Weyl fermions. Once an electric field parallel to the magnetic field is applied, the conservation of chirality no longer holds due to mixing the left-and-right movers. In such a case, charge pumping between the Weyl nodes of opposite chirality generates the positive longitudinal magnetoconductivity (LMC) or the negative magnetoresistivity (LMR) only when the electric current and magnetic field are parallel to each other. This strongly anisotropic behavior of LMC provides transport evidence for Weyl fermions.

Our findings of magnetotransport signatures specific to chiral anomalies in Mn_3Ge and planar Hall effect in Mn_3Sn provide concrete evidence for the presence of Weyl fermions in both materials. Figure 1a shows the field dependence of the magnetoconductivity observed in Mn_3Ge at 0.3 K. For applied fields B > 2T, the magnetoconductivity becomes positive for the parallel configuration and is nearly quadratic in magnetic field. The B^2 dependence of the positive LMC is likely a result of strongly titled type-II Weyl cones with the applied magnetic field perpendicular to the tilt axis. We

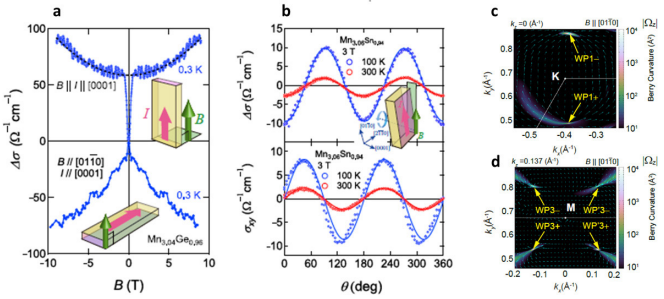

Fig. 1. (a) The magnetoconductivity as a function of the magnetic field B for the parallel and perpendicular configurations with the current $I \parallel [0001]$ measured at 0.3 K in Mn_3Ge. The dashed line is a fit to the quadratic magnetic field dependence. (b) Angle dependence of the longitudinal magnetoconductivity (top) and the planar Hall effect (PHE) (bottom) in $Mn_{3.06}Sn_{0.94}$ obtained at 300 and 100 K under B = 3 T. (c, d) Contour plots of the calculated Berry-curvature spectrum $|\Omega_z|$ in the k_x–k_y-plane under $B \parallel$ [01-10] at k_z = 0 (Å^{-1}) (c) and at k_z = 0.137 (Å^{-1}) (d). The arrows indicate the Berry curvature induced by the pairs of Weyl points WP1 and WP3 (WP'3) near the Fermi level.

further verified that the angular dependence of the magneto-conductivity and the planar Hall signal observed in Mn_3Sn agree well with the theoretical forms for the chiral anomaly (Fig. 1b), another transport evidence for magnetic Weyl fermions.

Moreover, we compare our results on the anomalous Hall and Nernst effects with the first-principles calculations that consider the substantial bandwidth renormalization and quasiparticle damping due to the strong electronic correlation in Mn_3X systems (Fig. 1c, d). The calculated transverse thermoelectric coefficients well reproduce the overall temperature dependence of the experimental data, suggesting that the large Berry curvature stemming from the Weyl nodes leads to significantly enhanced AHE and ANE in the absence of net magnetization.

Strongly correlated topological states have become a central focus for quantum materials research, and Mn_3X (X = Sn, Ge) is widely considered a textbook example of this kind. Our findings provide concrete evidence for the presence of Weyl fermions in both materials, which may trigger further exploration of their rich physics and useful properties emerging from the interplay between magnetism and band topology.

References

[1] T. Jungwirth *et al*., Nat. Nanotechnol. **11**, 231 (2016).
[2] S. Nakatsuji *et al.,* Nature **527**, 212 (2015).
[3] M. Ikhlas, T. Tomita *et al*., Nat. Phys. **13**, 1085 (2017).
[4] K. Kuroda *et al*., Nat. Mater. **16**, 1090 (2017).
[5] T. Chen, T. Tomita, S. Minami, M. Fu *et al*., Nat. Comm. **12**, 572 (2021).

Authors

T. Chen, T. Tomita, S. Minami, M. Fu, T. Koretsune[a], M. Kitatani, I. Muhammad, D. Nishio-Hamane, R. Ishii, F. Ishii[b], R. Arita[c,d], and S. Nakatsuji

[a]Tohoku University
[b]Kanazawa University
[c]RIKEN CEMS
[d]The University of Tokyo

Giant Effective Damping of Octupole Oscillation in a Chiral Antiferromagnet Mn_3Sn

Miwa, Nakatsuji, and Otani Groups

Understanding of spin dynamics forms the basis of spintronic application. For the ultrafast THz control of staggered moments in antiferromagnets, the time-resolved observation of spin dynamics is essential for developing the associated technology. However, such observation has been limited to insulators to date. Recently, the metallic anttiferromagnets Mn_3X have attracted significant attention for its strong response (e.g. anomalous Hall effect) comparable to ferromagnets owing to the hidden ferroic order, which configures large Berry curvature originated from Weyl points in a momentum space. Such ferroic order can be characterized by cluster magnetic octupoles based on neighbouring magnetic moments, and thus it is highly important to clarify the dynamics of cluster octupole for designing the spintronic application. In this research, we conduct time-resolved observation of spin-dynamics in a chiral antiferromagnet Mn_3Sn.

Bulk single-crystal $D0_{19}$-Mn_3Sn has been employed. Mn_3Sn has the hexagonal Ni_3Sn-type crystal structure consisting of an *ABAB* stacking of the kagome lattice of

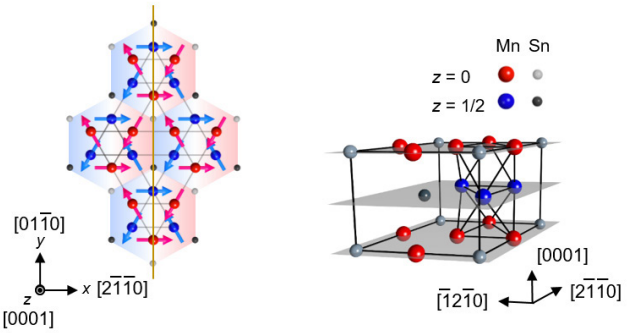

Fig. 1. (a) Spin and crystal structures of Mn_3Sn. Different colors are used to denote Mn and Sn atoms in the z = 0 and z = 1/2 planes. The inverse triangular spin-structure can be viewed as a ferroic ordering of cluster magnetic octupole, which possesses the same symmetry as the spin-magnetization (e.g. as indicated by a mirror plane (orange line)).

Mn atoms along the [0001] axis. Red (blue) circles in Fig. 1 indicate Mn atoms in *A*- (*B*-) plane of the kagome lattice. An inverse triangular spin structure is stabilized by exchange and Dzyaloshinskii-Moriya interactions [1,2]. The inverse triangular spin structure is made of a ferroic ordering of cluster magnetic octupoles [3].

Figure 2(a) shows typical TR-MOKE results, where a magnetic field of 2 T was applied normal to the surface. First, a pump light induces rapid decrease in the polar MOKE intensity of a probe light, similar to ultrafast demagnetization observed in ferromagnetic metals [4]. Consecutively, the MOKE intensity start to recover with delay time more than 0.3 ps, exhibiting a small but clear oscillation during the recovery. To further characterize the oscillating component, a non-oscillating component was estimated as a background (black solid curve) and subtracted from the raw data. The lower panel of Fig. 1(b) shows the TR-MOKE signals after subtracting the background. Figure 1(c) also shows typical TR-MOKE results (upper panel) and the analysis for the oscillating component (lower panel) in a relatively long-time range. From the fits in the lower panel of Figs. 1(b) (orange curve) and 1(c) (blue curve), oscillation frequencies (ω_I, ω_{II}) are determined as a function of an external magnetic field, namely, ω_I = 0.86 THz and ω_{II} = 18 GHz. The oscillating behaviour is most significant when the magnetic field is normal to the Mn_3Sn surface. Because

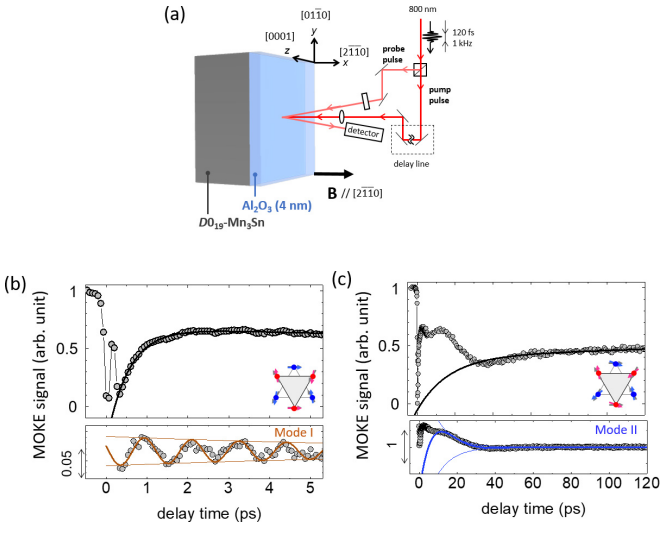

Fig. 2. (a) Schematic diagram of the time-resolved polar MOKE measurements (TR-MOKE). (b), (c) TR-MOKE signals of Mn_3Sn under a magnetic field of 2 T in the [2-1-10] direction. Backgrounds, indicated by black curves in upper panels, were subtracted from the raw data and plotted in the lower panels.

TR-MOKE signal is proportional to the surface normal polarization of the cluster magnetic octupoles, the oscillating Kerr signal should come from a change of size of the cluster magntic octupole order.

Two oscillation modes I and II are found through the analyses shown in Figs. 1(b) and 1(c), which should come from the dynamics of the cluster magnetic octupoles. The mode I and II are assigned to the optical and collective-precession-like modes. From Fig. 1(c), we find that the dynamics of the cluster octupole in Mn_3Sn is enhanced by exchange interaction, and it is feasible to conduct an ultrafast switching at < 10 ps, a hundred times faster than the case of spin-magnetization in a ferromagnet. Moreover, our theoretical analysis with the aforementioned experimental results shows that the Néel type domain wall velocity in Mn_3Sn can be estimated as > 10 km/s, which is greater than the recently reported value (~2 km/s) for the ferrimagnetic systems in the vicinity of the angular momentum compensation temperature [5]. Significantly, our study provides the first demonstration of the time-resolved observation of the spin-wave oscillation in an antiferromagnetic metal.

References

[1] S. Nakatsuji, N. Kiyohara, and T. Higo, Nature **527**, 212 (2015).
[2] S. Tomiyoshi and Y. Yamaguchi, J. Phys. Soc. Jpn. **51**, 2478 (1982).
[3] M.-T. Suzuki, T. Koretsune, and M. Ochi, Phys. Rev. B **95**, 094406 (2017).
[4] E. Beauprepaire *et al.*, Phys. Rev. Lett. **76**, 4250 (1996).
[5] K.-J. Kim *et al.*, Nat. Mater. **16**, 1187 (2017).

Authors

S. Miwa, S. Iihama[a], T. Nomoto[b], T. Tomita, T. Higo, M. Ikhlas, S. Sakamoto, Y. Otani, S. Mizukami[a], R. Arita[b], and S. Nakatsuji

[a]Tohoku University

[b]The University of Tokyo

Low Gilbert Damping in Epitaxial Thin Films of the Nodal-Line Semimetal $D0_3$-Fe_3Ga

Miwa and Nakatsuji Groups

$D0_3$-ordered Fe_3Ga [Fig. 1(a)] is a nodal-line semimetal and shows a giant anomalous Nernst effect (ANE). The origin of the ANE was attributed to the large density of states (DOS) and the large Berry curvature near the Fermi level. The large Berry curvature emerges as a result of spin-orbit-coupling-induced gap opening along the nodal lines consisting of nearly flat valence and conduction bands touching each other. This peculiar band structure may be useful for spintronics device application because a gate voltage may effectively modulate Berry-curvature-associated responses as well as magnetic anisotropy. In this regard, it is important to characterize the magnetization dynamics of $D0_3$-Fe_3Ga. For such a purpose, we fabricated epitaxial thin films of $D0_3$-Fe_3Ga and bcc-Fe and performed ferromagnetic resonance (FMR) measurements to evaluate their Gilbert damping constants.

50-nm-thick $D0_3$-Fe_3Ga and Fe thin films were grown by dc magnetron sputtering and molecular beam epitaxy, respectively. We confirmed that the $D0_3$-Fe_3Ga layer was grown epitaxially by performing high-energy electron diffraction and x-ray diffraction measurements. We conducted FMR measurements using a vector network analyzer and a coplanar waveguide. We employed a field-modulation technique [2], which measures the magnetic-field (H) derivative of the transmission coefficient ΔS_{21}, to minimize field-independent background signals.

Figure 1(b) shows typical FMR spectra of the Fe_3Ga thin film taken with magnetic fields applied along the [001] direction. Here, a FMR spectrum refers to ΔS_{21} as a function of magnetic field at a fixed frequency. From the FMR spectra, we deduced the peak positions and peak widths, which are shown in Figs. 1(c) and 1(d), respectively. We fitted the Kittel formula to the FMR peak positions, and the fits are shown by solid curves in Fig. 1(c). We found that the in-plane cubic anisotropy $H_{4//}$ of Fe_3Ga favors the magnetization along the [110] direction ($H_{4//} \sim -15$ mT), while those of Fe and disordered Fe-Ga alloys favor the [100] direction ($H_{4//} \sim +60$ mT for Fe and $H_{4//} \sim +75$-100 mT for the Fe-Ga alloys [3]). This magnetic-anisotropy change indicates that the $D0_3$ atomic ordering significantly alters the electronic band structure of Fe-Ga alloys and induces the giant ANE as a result.

The FMR peak widths of the Fe and Fe_3Ga thin films [Fig. 1(d)] showed linear behavior, the slope of which corresponds to the Gilbert damping constant. The linear fits yielded the Gilbert damping constants of $\alpha = 0.0023 \pm 0.0002$ for Fe and $\alpha = 0.0060 \pm 0.0002$ for $D0_3$-Fe_3Ga. These values are somewhat consistent with what is expected from the theoretical DOSs, indicating that Ga atoms do not significantly increase the spin-orbit coupling strength. Although the Gilbert damping constant of $D0_3$-Fe_3Ga is larger than that of bcc-Fe, it is still low compared to typical ferromagnets such as CoFeB ($\alpha \sim 0.004$-0.006) [4] and Permalloy ($\alpha \sim 0.007$) [5]. In other words, the nodal lines near the Fermi level do not hinder the magnetization dynamics much. The low Gilbert damping may be useful for spintronics device applications because one may be able to efficiently manipulate the magnetization direction by exploiting the peculiar band structure of $D0_3$-Fe_3Ga.

In summary, we have investigated the magnetization dynamics of the epitaxial thin films of the nodal-line semimetal $D0_3$-Fe_3Ga by ferromagnetic resonance measurements. We have deduced the intrinsic Gilbert damping constant of $D0_3$-Fe_3Ga to be $(6.0 \pm 0.2) \times 10^{-3}$, which is

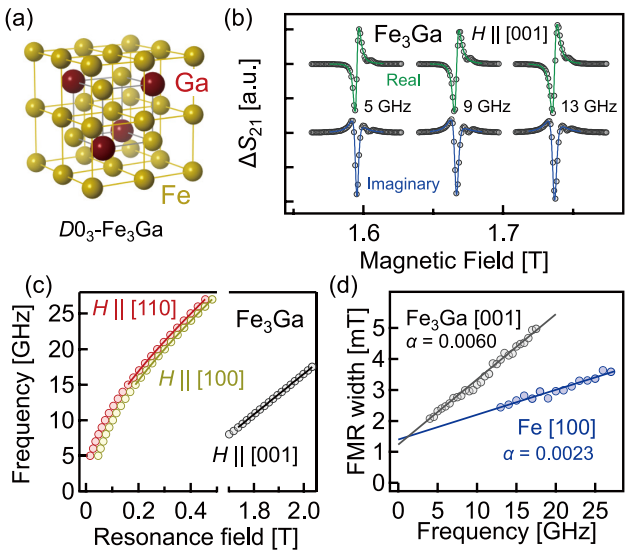

Fig. 1. (a) Crystal structure of $D0_3$-Fe_3Ga. (b) Typical Ferromagnetic resonance (FMR) spectra of $D0_3$-Fe_3Ga. (c) Resonance frequency plotted against resonance magnetic fields. The solid curves are the fits using the Kittel formula. (d) FMR peak widths of $D0_3$-Fe_3Ga and bcc-Fe. The solid lines represent the linear fits, the slope of which represents the intrinsic Gilbert damping constant.

larger than the Fe Gilbert damping constant of (2.3 ± 0.2) × 10^{-3} but as low as other typical ferromagnets. The low Gilbert damping and the peculiar band structure with a large Berry curvature make $D0_3$-Fe_3Ga attractive as a building block of spintronics devices.

References

[1] A. Sakai, S. Minami, T. Koretsune, T. Chen, T. Higo, Y. Wang, T. Nomoto, M. Hirayama, S.Miwa, D. Nishio-Hamane, F. Ishii, R. Arita, and S. Nakatsuji, Nature **581**, 53 (2020).
[2] S. Tamaru, S. Tsunegi, H. Kubota, and S. Yuasa, Rev. Sci. Instrum. **89**, 053901 (2018).
[3] S. Budhathoki, A. Sapkota, K. M. Law, B. Nepal, S. Ranjit, S. KC, T. Mewes, and A. J. Hauser, J. Magn. Magn. Mater. **496**, 165906 (2020).
[4] A. Conca, J. Greser, T. Sebastian, S. Klingler, B. Obry, B. Leven, and B. Hillebrands, J. Appl. Phys. **113**, 213909 (2013).
[5] Y. Zhao, Q. Song, S.-H. Yang, T. Su, W. Yuan, S. S. P. Parkin, J. Shi, and W. Han, Sci. Rep. **6**, 22890 (2016).

Authors

S. Sakamoto, T. Higo, S. Tamaru[a], H. Kubota[a], K. Yakushiji[a], S. Nakatsuji, and S. Miwa
[a]National Institute of Advanced Industrial Science (AIST)

Textbook Renormalization Group Prescription in Tensor-Network Language

Kawashima Group

Kadanoff's block-spin method gives a simple physical picture for the general RG transformations. Combined with Migdal's bond-moving trick, it serves as the first approximation that allows us direct estimation of the critical exponents, though the accuracy may not be satisfactory in many cases. However, it is not obvious how we can systematically improve on it so that eventually we can obtain, at least in principle, estimates as accurate as we like. Modern tensor-network (TN)-based methods, such as tensor renormalization group (TRG), tensor network renormalization (TNR), loop-TNR, high-order TRG (HOTRG), etc, opened up new possibilities for the RG transformations. Generalizing the conventional real-space RG (RSRG) transformations, they are more versatile and, more importantly, systematically improvable. The free energy, the energy, the magnetization, or any other locally defined order parameters can be computed by one of those methods. As for the estimation of the scaling dimensions, the CFT-based transfer-matrix method based on the conformal-field theory has been widely used for two-dimensional classical systems. For higher dimensions, however, the only method generally applicable

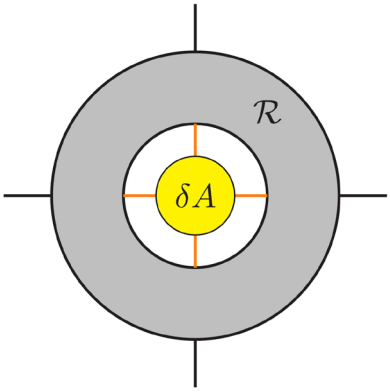

Fig. 1. Schematic diagram of the linearized tensor RG equation "R". In the proposed method, it can be generated using automatic differentiation once the coarse graining is implemented.

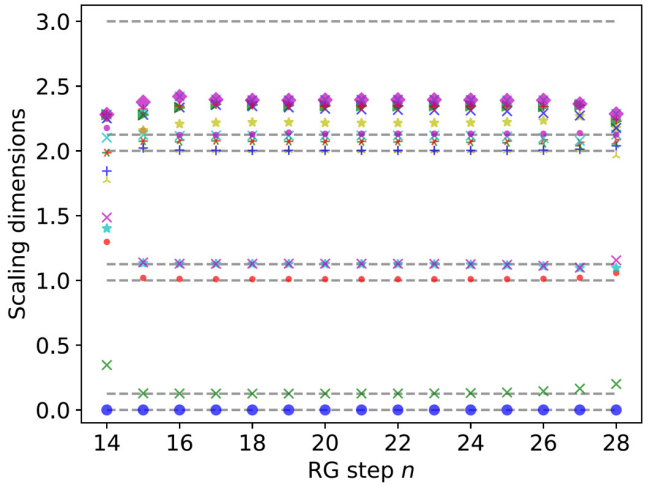

Fig. 2. The scaling dimensions of the 2D Ising model obtained directly from the linearized RG plotted against the number of RG steps applied at the critical point. The flat region represents the fixed point values.

was to esimate the correlation functions and apply the finite-size scaling to them. This indirect method may be good for obtaining one or two scaling dimensions, but it is obviously not a systematic way for obtaining a series of scaling dimensions.

Conceptually, it is straight-forward to construct a method for obtaining the series of scaling dimensions from any RSRG method. Simply we can expand the renormalized tensor with respect to the preceding tensor, i.e., the tensor at one RG step before the current one (Fig. 1). At the fixed point, the linear term would produce the scaling dimensions as its eigenvalues. This is exactly what we learn from textbooks for obtaining the scaling dimensions, in many cases with the Migdal-Kadanoff (MK) approximation as an example. In the MK approximation for the Ising model, we have only two independent fields, and it is impossible to obtain more than two scaling dimensions, whereas in the general TN-based method, we have as many fields as we like and, accordingly, we can in principle obtain many scaling dimensions systematically from the same calculation. However, it has been hard to carry out this straight-forward textbook program in practice because of the influence of the short-range entanglement.

In the paper [1], we adopted the graph-independent local truncation (GILT) method to eliminate the short-range entanglement. This made it possible to fully exploit the RG interpretation of various tensor-network-based methods and show a way to carry out the above-mentioned textbook RG prescription in the TN language: identify a fixed point, linearize the RG equation around this fixed point, and diagonalize it to obtain scaling dimensions. For the RSRG, we used HOTRG though it is not the only possible choice. As shown in Fig. 2, our benchmark calculation on the 2D classical Ising model shows that the proposed method works equally well compared with the above-mentioned CFT-based transfer matrix. The advantage of the present scheme is its potential applications to 3D systems, where the CFT-based method is inapplicable.

Reference

[1] X. Lyu, R. G. Xu, and N. Kawashima, Phys. Rev. Research **3**, 023048 (2021)

Authors

X. Lyu, R. G. Xu[a], and N. Kawashima
[a]The University of Tokyo

Weak Ferromagnetism and Possible Non-Fermi Liquid Behavior in Itinerant Electronic Material Co_3SnC

Uwatoko Group

In Fermi-liquid (FL) theory, the quasiparticle (QP) approximation and the generalized Boltzmann equation can describe the collective behaviors of strongly correlated multi-electron systems. For magnetic materials, strong magnetic correlations usually induce large changes in the QP-QP interactions, which make the QPs behave abnormally. Especially, when approaching the magnetic quantum critical point (QCP), various pronounced deviations from the Landau FL behaviors appear, e.g., non-Fermi liquid (NFL) and strong enhancement of the QP effective mass. On these issues, many correlated electronic materials including the heavy fermion (HF) systems have been studied through tuning the magnetic orders by strengthening the hybridizations between the 4f and conduction electrons and/or enhancing the magnetic correlations via external parameters. These studies are helpful to reveal the intrinsic characteristics of the competing electronic orders near QCPs.

Cobalt-contained materials are such alternatives to explore exotic QCPs owing to the various spin states of cobalt ions and their strong response to the external stimuli. Especially for those materials with both localized and itinerant electrons, the varieties of magnetic transition and phase diagram are more interesting. Metallic perovskite $M_3M'X$ (M is transition metals; M' is the main group elements; X is C, N) is such an example with diversified crystal structures and magnetic phase transitions. But the intrinsic magnetic interaction in $M_3M'X$ is controversial although various classical models were proposed. One possible reason for the absence of the universal theoretical model is that the system is not limited to the simple localized and/or itinerant interactions. Some reports have argued that these materials are close to the boundary of the localized and itinerant ferromagnetism and thus can be taken as an excellent platform to study the crossover between them. Among them, $Co_3M'X$ could be a good example to clarify these issues considering its unstable magnetic ground state and

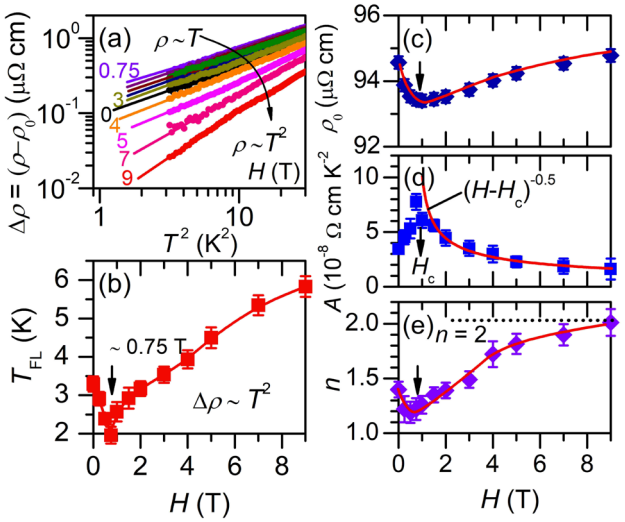

Fig. 1. (a) $\Delta\rho(T)$ vs. T^2 in a log-log scale; the arrow shows the crossover from T- to T^2-dependence. (b) Field-dependence of T_{FL}; the arrow shows the critical field; field dependence of the parameters: (c) ρ_0; (d) A and the exponential fitting results by the $(H\text{-}H_c)^{-0.5}$ (the red solid line); (e) n; the arrows in (c)-(e) indicate the change tendency and guides to the eye.

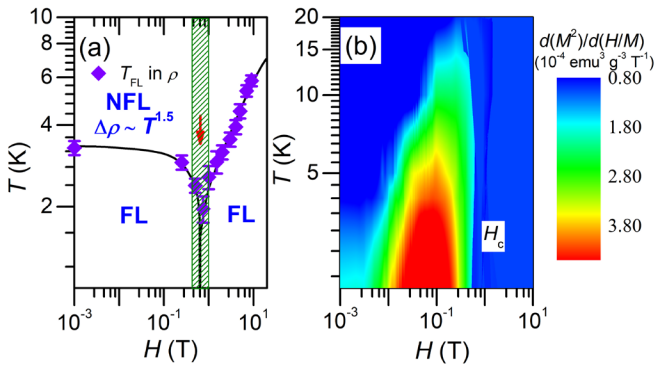

Fig. 2. Phase diagram and field-dependence of characteristic parameters for Co_3SnC: (a) T_{FL}; (b) the color shows its change tendency of $d(M^2)/d(H/M)$ vs. H which is proportional to the magnitude of magnetic fluctuations.

the abnormal quantum behaviors are expected by applying non-thermodynamic parameters.

In this study, weak ferromagnetism and NFL behaviors were observed in Co_3SnC via measurements of magnetic properties, electrical transport and specific heat under magnetic fields. Magnetic measurements suggest that it undergoes a paramagnetic to itinerant ferromagnetic phase transition with NFL behaviors including the power-law temperature dependence of resistivity, the -Tlog$T$-dependent upturn in specific heat, and the $T^{4/3}$-dependence of inverse susceptibility. With increasing the magnetic fields, the temperature coefficient of T^2-term in resistivity follows a $(H\text{-}H_c)^{-0.5}$-divergence upon approaching the critical field H_c, apart from the $1/(H\text{-}H_c)$-dependence with the whole Fermi surface under the singular scattering. The exponent n in the temperature dependence of resistivity shows an increase from n = 1.0 to 2.0 with increasing the field above H_c as the evidence for the field-induced crossover from NFL to FL behavior; the relative mass enhancement factor $\lambda(H)/\lambda(0)$ reduce to nearly 60% at 9.0 T, indicating the gradual suppression of magnetic fluctuations and electron-electron scattering. The results indicate that Co_3SnC is a good candidate for exploring itinerant quantum magnetic QCP.

Reference

[1] B. S.Wang, Y. Uwatoko, J. -G. Cheng, and Y. P. Sun, Phys. Rev. B. **102**, 085153 (2020)

Authors

B. S. Wang[a], Y. Uwatoko, J.-G. Cheng[a] and Y. P. Sun[b,c]

[a]Institute of Physics, CAS

[b]High Magnetic Field Laboratory, CAS

[c]Institute of Solid State Physics, CAS

Pattern Formation Induced by Mechanochemical Coupling of Reaction-Diffusion and Membrane Deformation

Noguchi Group

Shapes of biological membranes are dynamically regulated in living cells. Although membrane shape deformation by proteins at thermal equilibrium has been extensively studied, nonequilibrium dynamics have been much less explored. Recently, chemical reaction propagation has been experimentally observed in plasma membranes. Thus, it is important to understand how the reaction-diffusion dynamics are modified on deformable curved membranes.

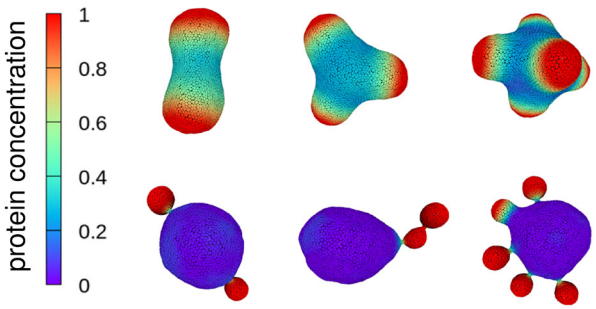

Fig. 1. Snapshots of vesicles with Turing patterns. Top panel: multi-spindle shapes. Bottom panel: budded vesicles. Color indicates the concentration of the curvature-inducing protein.

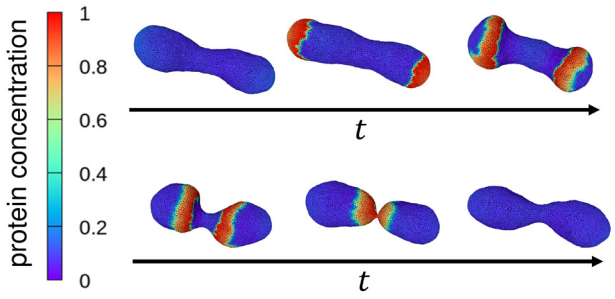

Fig. 2. Sequential snapshots of a shape-oscillation vesicle. Budding repeatedly occurs, accompanied by the propagation wave. Color indicates the concentration of the curvature-inducing protein.

In this study, we present nonequilibrium pattern formation on vesicles induced by mechanochemical feedback between membrane deformation and chemical reactions, using dynamically triangulated membrane simulations combined with a modified Brusselator model that is one of the simplest reaction-diffusion models. Two proteins (curvature-inducing and regulatory proteins) bind to the membrane. We found that membrane deformation changes stable patterns relative to those that occur on a non-deformable curved surface, as determined by linear stability analysis [1]. Temporal oscillation of the protein concentration can be changed into Turing pattern (stable spatial patterns). Budding and multi-spindle shapes are also induced by Turing patterns as shown in Fig. 1.

We also found that the propagating wave patterns change into non-propagating patterns and spiral wave patterns due to the mechanochemical effects [2]. Moreover, the wave speed is positively or negatively correlated with the local membrane curvature depending on the spontaneous curvature and bending rigidity. In addition, self-oscillation of the vesicle shape occurs, associated with the reaction-diffusion waves of curvature-inducing proteins as shown in Fig. 2. This agrees with the experimental observation of GUVs with a reconstituted Min system, which plays a key role in the cell division of *Escherichia coli*. Our results demonstrate the importance of mechanochemical feedback in pattern formation on deforming membranes.

References
[1] N. Tamemoto and H. Noguchi, Sci. Rep. **10**, 19582 (2020).
[2] N. Tamemoto and H. Noguchi, Soft Matter **17**, 6589 (2021).

Authors
N. Tamemoto and H. Noguchi

Structures and Dynamics of Hydrogen Cluster Materials Li_5MoH_{11} and Li_6NbH_{11}

Yamamuro Group

In the current research field of batteries, there are strong demands for high-performance hydrogen storage materials and ionic (H^+, Li^+, etc.) conductors. Recently, a series of novel materials Li_5MoH_{11}, Li_5WH_{11}, Li_6NbH_{11}, Li_6TaH_{11} which contain unusual ninefold hydrogen-coordinated clusters MH_9 (M= Mo, W, Nb, Ta), whose structure is shown in the inset of Fig. 1, were synthesized by Orimo group in Tohoku University [1]. These are of interest since they have high hydrogen density and possible high Li ionic conductivity. The dynamics of MH_9 cluster may play important roles in determining the physical properties of the materials. We have performed the neutron powder diffraction (NPD) and quasielastic neutron scattering (QENS) experiments of Li_5MoH_{11} and Li_6NbH_{11}.

Both samples were synthesized from solid-state reactions under high pressure (ca. 5 GPa) and high temperature (ca. 700 K). Owing to these difficulties, the sample amounts of Li_5MoH_{11} and Li_6NbH_{11} were 33 mg and 20 mg, respectively. The NPD and QENS measurements were conducted using high intensity total diffractometer NOVA (BL21) and biomolecular dynamic spectrometer DNA (BL02) in MLF, J-PARC, respectively. The DNA data were collected with both high and low energy resolution modes.

From the Rietveld analyses for the NPD data at room temperature, we have checked the purity of the samples (Li_5MoH_{11}: 75 %, Li_6NbH_{11}: 57 %) and confirmed that the MH_9 clusters are orientationally disordered. Figure 1 shows the intermediate scattering functions of Li_5MoH_{11}. Similar data were obtained also in Li_6NbH_{11}. Relaxation phenomena were observed in a wide temperatures range between 150 K and 300 K. It is quite unusual that the relaxation occurs in a wide time range over 3 orders of magnitude as shown in the data at 300 K. Therefore, the data were fitted with not an exponential but Kohlraush-Williams-Watts (KWW) function

$$I(Q,t) = a(Q) + b(Q)\exp[-(t/\tau_{KWW})^{\beta}],$$

where Q is magnitude of a scattering vector, t is a time, τ_{KWW} is a relaxation time, β is a non-exponential parameter, and $a(Q)$ and $b(Q)$ are elastic and relaxation components, respectively. The β parameter ($0 < \beta < 1$) reflects the width

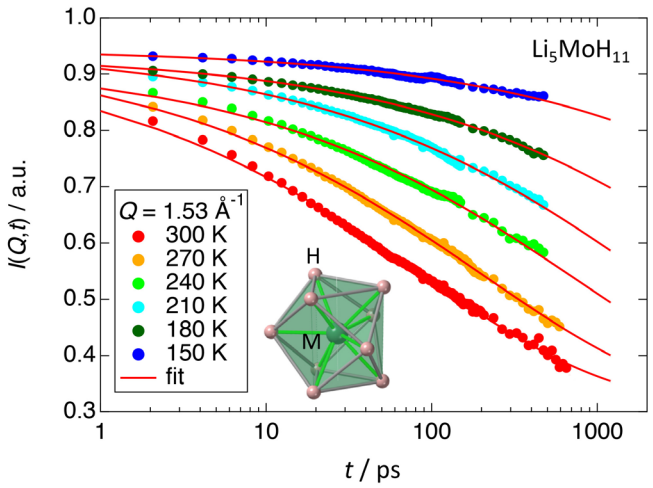

Fig. 1. Intermediate scattering functions (Q = 1.53 Å^{-1}) of Li_5MoH_{11} measured at several temperatures between 150 K and 300 K. The solid curves are fitting curves to the KWW functions with β = 0.38. The inset shows the structure of the MH_9 cluster.

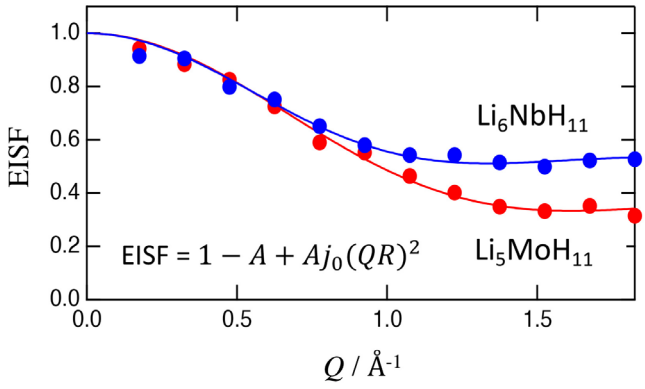

Fig. 2. Elastic Incoherent Structure Factor (EISF) obtained at 300 K for Li_5MoH_{11} and Li_6NbH_{11}. The solid curves are the fitting curves to the equation in the figure.

of the relaxation time distribution; no distribution at $\beta = 1$. The fittings were satisfactory as shown by solid curves in Fig. 1. The determined β were 0.38 for Li_5MoH_{11} and 0.33 for Li_6NbH_{11}, indicating that the distribution of the relaxation time is very wide; cf. β is around 0.5 for glass forming liquids. The activation energies obtained from the temperature dependence of the relaxation times were 15 kJmol^{-1} for Li_5MoH_{11} and 27 kJmol^{-1} for Li_6NbH_{11}. The magnitude of the activation energy may depend on the ionic valence and size (M-H distance) of the hydrogen cluster (MoH_9^{3-}: 1.76 Å, NbH_9^{4-}: 1.86 Å) .

Figure 2 shows the Q dependence of EISF (Elastic Incoherent Scattering Factor) which is defined by EISF = $a(Q)/[a(Q) + b(Q)]$. As shown by the solid curves in Fig. 2, EISF was well fitted by

$$\text{EISF} = 1 - A + Aj_0^2(QR),$$

where $j_0(QR)$ is a 0th order sphere Bessel function with a radius R. This indicates that MH_9 clusters are spherically rotating at 300 K, which is consistent with the structural information. The rotational states of the MH_9 clusters are now investigated with a first-principle MD simulation technique. We guess that the wide distribution of the relaxation time is associated with the positional disorder of Li ions conducting in the crystals.

This work is financially supported by JSPS KAKENHI No. JP 18H05513 and JP18H05518.

Reference

[1] S. Takagi, Y. Iijima, T. Sato, H. Saitoh, K. Ikeda, T. Otomo, K. Miwa, T. Ikeshoji, and S. Orimo, Sci. Rep. **7**, 44253 (2017).

Authors
Y. Ohmasa, H. Akiba, S. Takagi[a], S. Orimo[a], H. Saito[b], T. Yamada[c], Y. Kawakita[d], K. Ikeda[e], T. Otomo[e] and O. Yamamuro
[a]Tohoku University
[b]QST
[c]CROSS
[d]JAEA
[e]KEK

Magnetic Order in the Chemically Substituted Frustrated Antiferromagnet $CsCrF_4$

Masuda Group

In geometrically frustrated magnets, macroscopically degenerated ground-states in low-energy regime can be solved by small perturbations. This tells us that magnetic states at low temperatures highlights small effects such as magnetic anisotropy, exchange randomness, and site dilution. These thus play key roles in determining ground states in frustrated magnets. The equilateral triangular spin tube antiferromagnet $CsCrF_4$ [1,2] is a candidate for realizing a ground state sensitive to small perturbations. Magnetic Cr^{3+} ions having $S = 3/2$ form triangular spin tubes along the crystallographic c axis, as illustrated in Fig. 1. The tubes couple magnetically with one another and form the kagome-triangular lattice in the ab plane [3]. Neutron powder diffraction study conducted by our group identified long-range magnetic order below 2.8 K [4]. The magnetic moments form a quasi-120° structure in the ab plane. It is unique that the 120° structure propagates antiferromagnetically along the a and c axes with a magnetic propagation vector $\boldsymbol{k}_{mag}$ = (1/2, 0, 1/2). Discussion of ground states in the kagome-triangular lattice model suggested that the ground state of $CsCrF_4$ is close to the boundary on the magnetic phase diagram in the kagome-triangular lattice model [4]. This proposes that small perturbations may induce various types of magnetic states in $CsCrF_4$.

To introduce small perturbations into $CsCrF_4$, we investigate chemical substitution effect. A magnetic Fe-substituted $CsCr_{1-x}Fe_xF_4$ showed long-range magnetic order and enhancement of magnetic anisotropy [5]. In a nonmagnetic Al-substituted $CsCr_{1-x}Al_xF_4$, a weak feature of magnetic ordering was observed [5]. Hereby, we report chemical substitution effects on the magnetic ground state in $CsCrF_4$ [6].

We carried out neutron powder diffraction experiments on $CsCr_{0.94}Fe_{0.06}F_4$ and $CsCr_{0.98}Al_{0.02}F_4$. In both compounds, magnetic Bragg peaks indicative of the long-range magnetic order are clearly observed, as shown in Fig. 2. Most strikingly, the magnetic peaks in $CsCr_{0.94}Fe_{0.06}F_4$ are indexed by a propagation vector $\boldsymbol{k}_{mag}$ = (0, 0, 1/2), which is different symmetry from $\boldsymbol{k}_{mag}$ = (1/2, 0, 1/2) in the parent $CsCrF_4$. Magnetic structure analysis identifies that the 120° structure does not alternate in the ab plane, whereas the intratube structure is the same as in $CsCrF_4$. Based on the Goodenough-Kanamori rule on superexchange interactions [7,8], it is predicted that ferromagnetic (antiferromagnetic) interactions between the Cr^{3+} ions via the F^- ions turn into antiferromagnetic (ferromagnetic) interactions by the Fe^{3+} ion substitution, namely bond substitution. The identified magnetic structure, thus, means that the bond substitution by the magnetic Fe^{3+} ion modifies the intertube structure, but the intratube structure is intact.

On the contrary, in $CsCr_{0.98}Al_{0.02}F_4$ the observed magnetic peaks are indexed by the same propagation vector as in the parent $CsCrF_4$. Analyzing the magnetic structure,

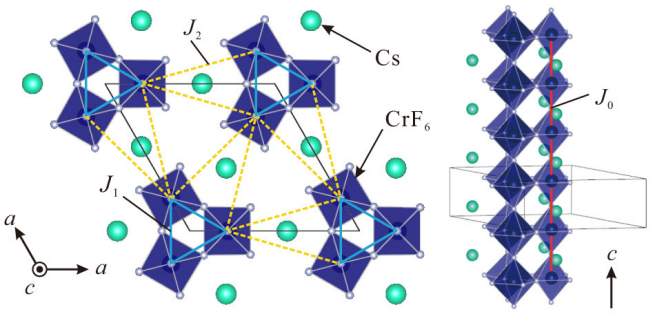

Fig. 1. Schematic view of the crystal structure of $CsCrF_4$. Red lines a indicate the nearest-neighbor interaction along the c axis. Blue and yellow lines indicate the nearest- and second-neighbor interactions in the ab plane.

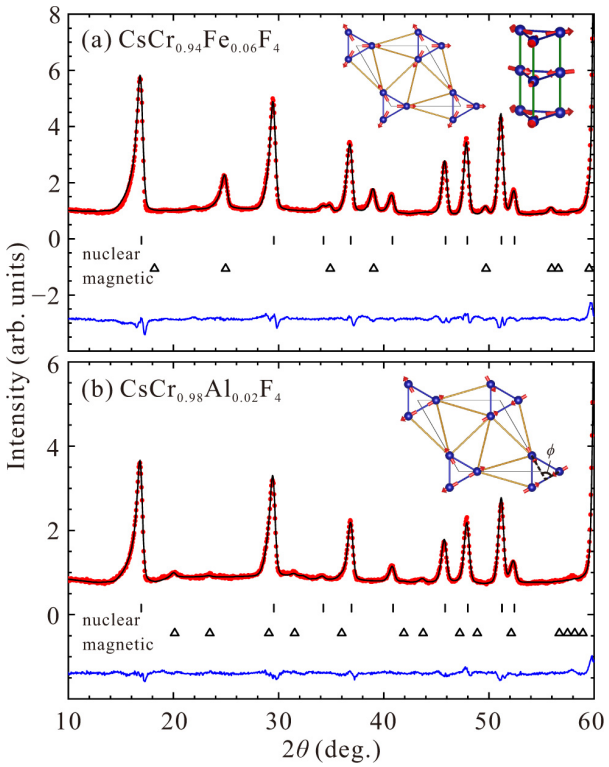

Fig. 2. Neutron diffraction profiles for (a) $CsCr_{0.94}Fe_{0.06}F_4$ and (b) $CsCr_{0.98}Al_{0.02}F_4$ at 1.5 K. Red circles and black curves show the experimental data and simulations, respectively. Vertical bars and triangles indicate the position of the nuclear and magnetic Bragg peaks. Blue curves show the difference between the data and simulations. Insets are the determined magnetic structures.

we find that the spin configuration in $CsCr_{0.98}Al_{0.02}$ is not changed drastically, even though a relative angle between three spins in the 120° structure deviates more from 120° than that in $CsCrF_4$. Since substituting the Cr^{3+} ion with the Al^{3+} ion creates a spin vacancy, trigonal symmetry of the 120° structure is locally broken. However, the spin vacancy only produces a small effect on the ground state of $CsCrF_4$, and therefore the quasi-120° structure is still realized globally in $CsCr_{0.98}Al_{0.02}F_4$.

In conclusion, we have studied magnetic orders in magnetic Fe- and nonmagnetic Al-substituted $CsCrF_4$ through the neutron powder diffraction experiment. The magnetic structure analysis reveals that the Fe-substituted sample exhibits a 120° structure having $\boldsymbol{k}_{mag}$ = (0, 0, 1/2), and the Al-substituted one has a quasi-120° structure having $\boldsymbol{k}_{mag}$ = (1/2, 0, 1/2). Importantly, the magnetic structure in $CsCr_{0.94}Fe_{0.06}F_4$ differs from that in the parent $CsCrF_4$. This result concludes that the ground state in $CsCrF_4$ is more sensitive to magnetic substitution rather than nonmagnetic one on the Cr site.

References
[1] H. Manaka *et al.*, J. Phys. Soc. Jpn. **78**, 093701 (2009).
[2] H. Manaka *et al.*, J. Phys. Soc. Jpn. **80**, 084714 (2011).
[3] K. Seki and K. Okunishi, Phys. Rev. B **91**, 224403 (2015).
[4] M. Hagihala *et al.*, npj Quantum Mater. **4**, 13 (2019).
[5] H. Manaka *et al.*, J. Phys. Soc. Jpn. **88**, 114703 (2019).
[6] S. Hayashida, M. Hagihala, M. Avdeev, Y. Miura, H. Manaka, and T. Masuda, Phys. Rev. B **102**, 174440 (2020).
[7] J. B. Goodenough, Phys. Rev. **100**, 564 (1955).
[8] J. Kanamori, J. Phys. Chem. Solids **10**, 87 (1959).

Authors
S. Hayashida, M. Hagihala[a], M. Avdeev[b], Y. Miura[c], H. Manaka[d], and T. Masuda
[a]High Energy Accelerator Research Organization (KEK)
[b]Australian Nuclear Science and Technology Organisation (ANSTO)
[c]Suzuka National College of Technology
[d]Kagoshima University

Zero-Energy Excitation in the Classical Kagome Antiferromagnet $NaBa_2Mn_3F_{11}$

Masuda Group

Localization of spin-wave excitations, so-called *zero-energy mode*, is one of the unique phenomena in geometrically frustrated magnets [1]. Largely degenerate ground states allow a continuous rearrangement of spins with no energy cost, generating a dispersionless mode in a spin-wave excitation spectrum. The classical kagome antiferromagnet is a prototypical model for the dispersionless mode in the spin-wave excitations. It has an infinite degeneracy of 120° structures in the ground state. This degeneracy allows a continuous change of the spin arrangement with no energy cost, as illustrated in Fig. 1(a).

In real kagome antiferromagnets, the macroscopic degeneracy of the 120° structures is solved by some types of magnetic anisotropy such as the Dzyaloshinskii-Moriya interaction, single-ion anisotropy, and magnetic dipole-dipole interaction. Then, the zero-energy mode becomes visible as an excited state lifted by those anisotropies. Although the zero-energy mode is one of the most characteristic phenomena in frustrated kagome antiferromagnets, it has been reported only in $KFe_3(OH)_6(SO_4)_2$ [2]. Therefore, further study in different materials is highly desirable.

Our target material, a classical kagome antiferromagnet $NaBa_2Mn_3F_{11}$ [3], is a promising candidate exhibiting the zero-energy mode. Mn^{2+} ions having spin S = 5/2 are responsible for magnetic properties. Neutron powder diffraction demonstrated that antiferromagnetic order below T_N = 2 K forms the 120° structure selected by the magnetic dipolar interaction [4], as shown in Fig. 1(a). According to theoretical studies, the zero-energy mode in the classical kagome antiferromagnet with the magnetic dipolar interaction is predicted to emerge at its lowest excited state [5], as shown in Fig. 1(b). Hereby, we report the zero-energy mode excitation in $NaBa_2Mn_3F_{11}$ through a combination of inelastic neutron scattering technique and linear spin-wave calculations [6].

Figures 2(a)-2(d) show a temperature variation of the inelastic neutron scattering spectra for a powder sample of $NaBa_2Mn_3F_{11}$. Magnetic diffuse scattering indicative of short-range correlation is observed at 30 K in the paramagnetic phase [Fig. 2(d)]. The diffuse scattering is suppressed with decreasing temperature, and the spectrum splits into two parts: strong intensity at 0.2 meV and weak intensity at 1.5 meV [Figs. 2(a)-2(c)]. In the magnetic ordered state at 1.5 K, spin-wave excitations having a magnetic anisotropy

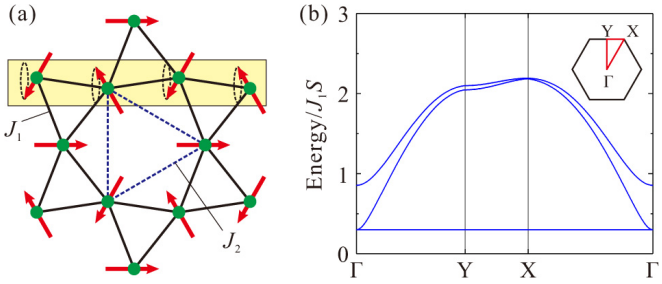

Fig. 1. (a) Magnetic structure having $\boldsymbol{k}$ = **0** of $NaBa_2Mn_3F_{11}$. The red arrows represent directions of spins. Dashed loops illustrate the zero-energy mode as described in the text. Solid and dashed lines are the nearest-neighbor and second-neighbor paths, respectively. (b) Spin-wave excitation having the nearest-neighbor exchange interaction J_1 and magnetic dipole-dipole interaction $J_{MDD} = J_1/100$. The energy is normalized by the magnitude of J_1 and spin S.

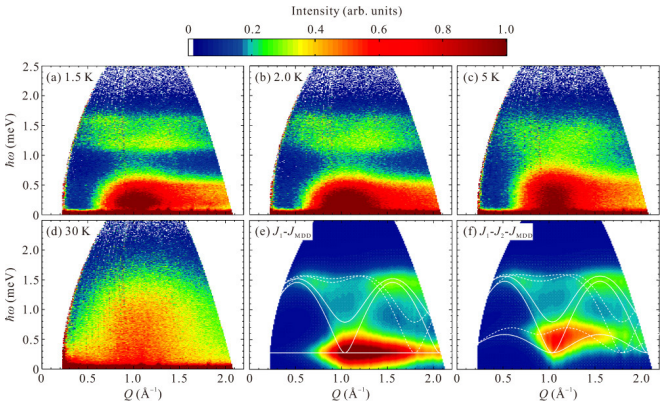

Fig. 2. Inelastic neutron scattering spectra of $NaBa_2Mn_3F_{11}$ at (a) 1.5 K, (b) 2.0 K, (c) 5 K and (d) 30 K. The incident neutron energy is E_i = 3.1 meV. Calculated spin-wave spectra with (e) J_1 = 0.28 meV, J_2 = 0, and J_{MDD} = 4.9 μeV and with (f) J_1 = 0.27 meV, $J_2 = J_1/10$, and J_{MDD} = 4.9 μeV. Solid and dashed curves in (e) and (f) are spin-wave dispersions along [1 0 0] and [1 1 0] directions, respectively.

gap of 0.21 meV is observed, as shown in Fig. 2(a). Notably, the excitation at 0.21 meV does not shift on varying wave number Q. This suggests that the excitation is a dispersionless zero-energy mode lifted by the magnetic dipolar interaction.

To identify if the observed dispersionless mode indeed originate from the magnetic dipolar interaction, we simulated the spin-wave excitation spectra in the linear spin-wave theory with considering the nearest-neighbor exchange interaction J_1, the second neighbor exchange interaction J_2, and the nearest-neighbor magnetic dipolar interactions J_{MDD}. Figures 2(e) and 2(f) show powder-averaged spin-wave spectra in J_1-J_{MDD} and J_1-J_2-J_{MDD} models, respectively. The calculated spectra semi-qualitatively reproduce the low-energy strong excitation and high-energy weak excitation. Importantly, the calculated spectrum shows that the second-neighbor interaction J_2 makes the zero-energy excitation dispersive (Fig. 2(f)), because further neighboring interactions suppress the continuous rearrangement of the spins with no energy cost. This means that the observed dispersionless excitation at 0.2 meV indicates that J_2 is negligible in $NaBa_2Mn_3F_{11}$.

The most remarkable finding is that the energy position of the dispersionless mode is reproduced solely by the magnetic dipolar interaction. We note that the magnetic dipolar interaction is ubiquitous in every real magnet even though the qualitative behavior of most kagome antiferromagnet can be explained by models including only the nearest-neighbor interaction. Therefore, we come to the conclusion that the observed dispersionless excitation in $NaBa_2Mn_3F_{11}$ is the ideal zero-energy mode in the realistic classical kagome antiferromagnet.

In summary, we discovered a dispersionless zero energy mode in the classical kagome antiferromagnet $NaBa_2Mn_3F_{11}$ by the inelastic neutron scattering technique. The calculations based on the linear spin-wave theory reveal that the excitation is described by the zero-energy mode lifted solely by the magnetic dipole-dipole interactions. $NaBa_2Mn_3F_{11}$ is a unique classical kagome antiferromagnet exhibiting a truly dispersionless lifted zero-energy excitation.

References

[1] A. B. Harris, C. Kallin, and A. J. Berlinsky, Phys. Rev. B **45**, 2899 (1992).
[2] K. Matan *et al*., Phys. Rev. Lett. **96**, 247201 (2006).
[3] H. Ishikawa *et al*., J. Phys. Soc. Jpn. **83**, 043703 (2014).
[4] S. Hayashida *et al*., Phys. Rev. B **97**, 054411 (2018).
[5] M. Maksymenko, R. Moessner, and K. Shtengel, Phys. Rev. B **96**, 134411 (2017).
[6] S. Hayashida, H. Ishikawa, Y. Okamoto, T. Okubo, Z. Hiroi, G. J. Nilsen, H. Mutka, and T. Masuda, Phys. Rev. B **101**, 214409 (2020).

Authors
S. Hayashida, H. Ishikawa, Y. Okamoto[a], T. Okubo[b], Z. Hiroi, G. J. Nilsen[c], H. Mutka[d], and T. Masuda
[a]Nagoya University
[b]The University of Tokyo
[c]ISIS Neutron and Muon Source
[d]Institute Laue Langevin

Spin Density Wave Induced by Bound Two-Magnon in S = 1/2 Frustrated Chain Compound $NaCuMoO_4(OH)$

Masuda Group

Frustrated magnetism has attracted great attention because of nontrivial phases induced by the lift of macroscopic degeneracy. One of the interesting examples is found in S = 1/2 one-dimensional spin system with nearest-neighbor ferromagnetic and next-nearest-neighbor antiferromagnetic interactions [1]. A theory predicts that a bound two-magnon in high magnetic field induces exotic phases characterized by the spin-density-wave (SDW) and spin multipole correlations in the frustrated ferromagnetic chain [2]. So far, these states have not been fully investigated by spectroscopic method because of high saturation field and/or difficulty of obtaining a large single crystal for existing model compounds. $NaCuMoO_4(OH)$ is an experimental realization of the system having decent energy scale, saturation field of 26 T [3] which is available on the pulse magnet for neutron scattering [4]. The synthesis of a single crystal

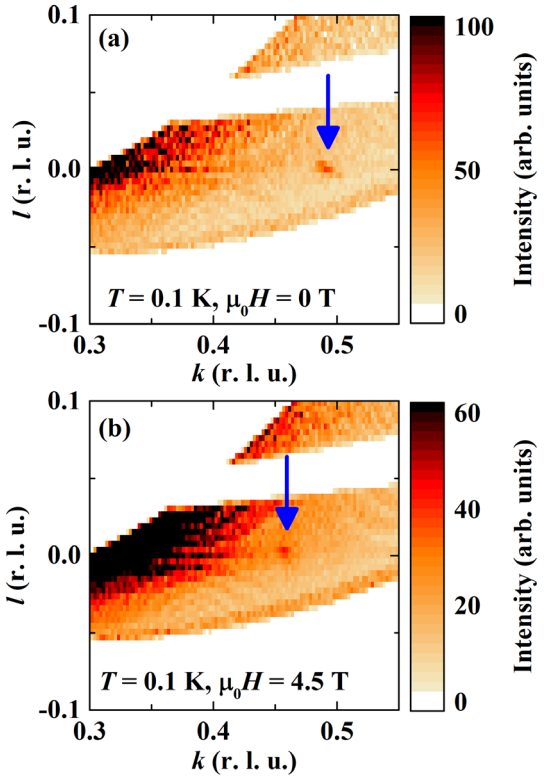

Fig. 1. Contour maps of neutron intensities in the (0kl) plane around the reciprocal lattice point (0, δ, 0) at 0.1 K under the magnetic field of (a) 0 and (b) 4.5 T.

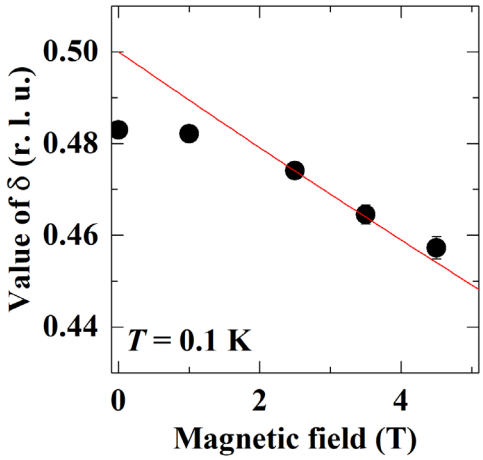

Fig. 2. Value of δ as a function of field

was reported [5]. The NMR and heat capacity study suggest a magnetic transition at H_c of 1.5 - 1.8 T [3]. For the full identification of the magnetic states in zero and finite fields neutron diffraction technique is indispensable. We hereby report the magnetic structure analysis by using the time-of-flight neutron diffractometer SENJU installed at J-PARC [6] on a single crystal $NaCuMoO_4(OH)$.

Figure 1(a) and 1(b) shows the contour maps of neutron intensities in the (0*kl*) plane around the reciprocal lattice point (0, δ, 0) at 0.1 K under the magnetic field of (a) 0 and (b) 4.5 T. We found that the peak indicated by the blue arrow in Fig. 1(a) appear at (0, δ, 0) ($\delta \sim 0.48$) below the transition temperature of 0.6 K. It means that the peak comes from the magnetic origin. We further found peaks at (1 δ 1) and (0 δ 2). Magnetic structure analysis reveals that the proper-screw structure with the ferromagnetic interchain coupling with the propagation vector of (0, δ, 0) is realized at zero field. Furthermore, we found that the magnetic peak at (0 δ 0) was shifted to smaller k direction by applying a magnetic field as shown in Fig. 1(b). This behavior suggests that the field induces SDW state, in which the density correlation of bound magnon is developed and its incommensurability is represented in terms of magnetization. In Fig. 2 the value of δ is independent of the field below H_c, and it decreases with increasing the field above H_c. The negative slope of the line above H_c indicated by red line is consistent with the theoretical prediction for the SDW_2 state [7]. The result demonstrates that the bound two-magnon leads to the SDW state in high magnetic field in the compound.

References

[1] S. Furukawa, M. Sato, and S. Onoda, Phys. Rev. Lett. **105**, 257205 (2010).
[2] T. Hikihara, L. Kecke, T. Momoi, and A. Furusaki, Phys. Rev. B **78**, 144404 (2008).
[3] K. Nawa, Y. Okamoto, A. Matsuo, K. Kindo, Y. Kitahara, S. Yoshida, S. Ikeda, S. Hara, T. Sakurai, S. Okubo, H. Ohta, and Z. Hiroi, J. Phys. Soc. Jpn. **83**, 103702 (2014).
[4] H. Nojiri, S. Yoshii, M. Yasui, K. Okada, M. Matsuda, J. -S. Jung, T. Kimura, L. Santodonato, G. E. Granroth, K. A. Ross, J. P. Carlo, and B. D. Gaulin, Phys. Rev. Lett. **106**, 237202 (2011).
[5] K. Nawa, Y. Okamoto, and Z. Hiroi, J. Phys.: Conf. Ser. **828**, 012005 (2017).
[6] T. Ohhara, R. Kiyanagi, K. Oikawa, K. Kaneko, T. Kawasaki, I. Tamura, A. Nakao, T. Hanashima, K.Munakata, T. Moyoshi, T. Kuroda, H. Kimura, T. Sakakura, C.-H. Lee, M. Takahashi, K.-i. Ohshima, T. Kiyotani, Y. Noda, and M. Arai, J. Appl. Cryst. **49**, 120 (2016).
[7]. M. Sato, T. Momoi, and A. Furusaki, Phys. Rev. B **79**, 060406(R) (2009).

Authors

S. Asai, T. Oyama, K. Nawa[a], A. Nakao[b], K. Munakata[b], K. Kuwahara[c], M. Hagihala[d], S. Itoh[d], Z. Hiroi, and T. Masuda

[a]Institute of Multidisciplinary Research for Advanced Materials, Tohoku University
[b]Research Center for Neutron Science and Technology, Comprehensive Research Organization for Science and Society
[c]Institute of Quantum Beam Science, Ibaraki University
[d]High Energy Accelerator Research Organization

Neutron Resonance Spin Echo Measurements on the Magnetic Skyrmion Lattice State in MnSi

Nakajima Group

Magnetic skyrmions are vortex-like spin objects, which can be regarded as topological defects composed of magnetic moments in a magnetic material [1]. They were discovered in a small phase pocket in the vicinity of the critical temperature in chiral cubic magnets; previous small-angle neutron scattering (SANS) [2] and Lorentz transmission electron microscopy [3] measurements have revealed that the magnetic vortices are arranged to form a triangular lattice on a plane perpendicular to an applied magnetic field. It is also reported that the magnetic skyrmions can be driven by flowing an electric current [4]. These observations show that magnetic skyrmions behave like particles once they are formed, while it remains unclear how the particle character emerges upon the phase transition from the paramagnetic (PM) phase to the skyrmion lattice (SkL) phase.

In the present study, we investigate the PM-to-SkL transition in an archetypal skyrmion compound MnSi by means of neutron spin echo (NSE) spectroscopy [5], which is suited for probing diffusive dynamics with the time scales of the order of pico- to submicroseconds. Actually, spin fluctuations in MnSi were studied by means of polarimetric and ferromagnetic NSE measurements [6], in which the Larmor precession of polarized neutron spin is utilized for detecting very small changes in neutron velocity upon quasi-elastic scattering processes. However, neither the polarimetric nor ferromagnetic NSE is suited for the SkL phase. The former is limited to zero-field measurements. Although the latter is applicable for in-field measurements, the non-collinear

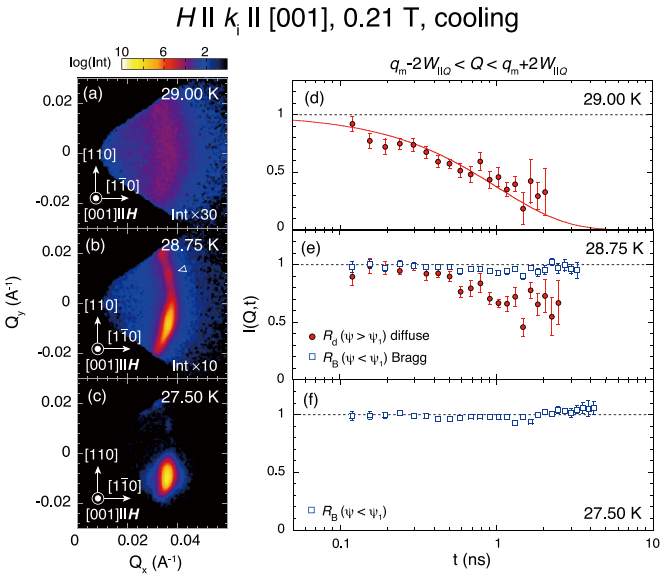

Fig. 1. [(a)-(c)] Intensities of scattered neutrons projected on the *Qx*-*Qy* plane measured at (a) 29.00, (b) 28.75, and (c) 27.50 K. on cooling. [(d)-(f)] $I(Q,t)$ profiles at each temperature.

spin arrangement of the SkL leads to mixing of spin-flip and non-spin-flip scatterings, which depolarizes the neutron spins. We thus employ neutron resonance spin echo technique, specifically the modulation-of-intensity-with-zero-effort (MIEZE) method, in which the intermediate spin correlation function $I(Q,t) = S(Q,t)/S(Q,0)$, where $S(Q,t)$ is the temporally Fourier transformed dynamical structure factor, is obtained not from the final neutron spin polarization after experienced the precessions mentioned above, but from beating patterns appearing in intensities of scattered neutrons as a function of time. Since the MIEZE signals are independent of the spin state of scattered neutrons, this technique is suited for measuring magnetic scattering in a magnetic field [7].

In Figs. 1(a)-1(c), we show typical SANS patterns measured in a magnetic field of 0.21 T at the VIN ROSE instrument in the materials and life science experiment facility in J-PARC. We observed a ring-like diffuse scattering pattern at 29 K, which is slightly above the critical temperature of 28.8 K (Fig. 1(a)). This indicates that a short-range isotropic spin correlation is developing in the sample. As the temperature is lowered, a Bragg peak emerges and coexists with the ring-like diffuse scattering (Fig. 1(b)). Finally, the diffuse scattering completely disappears and only the Bragg peak remains at 27.5 K (Fig. 1(c)). We obtained $I(Q,t)$ profiles of the diffuse and Bragg scattering components as shown in Figs. 1(d)-1(f). The $I(Q,t)$ profile at 29 K shows a decay, which is well described by a single-exponential decay function, revealing that the magnetic moments involved in the diffuse scattering are fluctuating with a characteristic time of 1 ns. By contrast, no temporal decay of the spin correlation is found at 27.5 K (Fig. 1(f)). At the intermediate temperature where the Bragg and diffuse scattering coexist, the $I(Q,t)$ profile for the diffuse component still shows a decay, while that for the Bragg peak is approaching unity. This demonstrates that the isotropic spin fluctuations with short-range spin correlations coexists with static SkL domains near the boundary between the PM and SkL phases. We also analyzed the $I(Q,t)$ values as a function of azimuthal angle, and concluded that an aggregation of the magnetic skyrmions upon cooling leads to orientational disorder of the small SkL domains. This picture is consistent with the particle-like character of the magnetic skyrmions. The present results also show that the MIEZE-type NSE at VIN ROSE is a powerful tool to study spin dynamics of magnetic skyrmion systems, for which measuring spin dynamics in low-Q regions in a magnetic field is essential.

References

[1] N. Nagaosa and Y. Tokura, Nat. Nanotechnol. **8**, 899 (2013).
[2] S. Muhlbauer *et al.*, Science **323**, 915 (2009).
[3] X. Z. Yu *et al.*, Nature **465**, 901 (2010).
[4] X. Z. Yu *et al.*, Nat. Mater. **10**, 106 (2011).
[5] T. Nakajima *et al.*, Phys. Rev. Research **2**, 043393 (2020).
[6] C. Pappas *et al.*, Phys. Rev. Lett. **102**, 197202 (2009).
[7] J. Kindervater *et al.*, Phys. Rev. X **9**, 041059 (2019).

Authors

T. Nakajima, T. Oda[a], M. Hino[a], H. Endo[b], K. Ohishi[c], K. Kakurai[c,d], A. Kikkawa[d], Y. Taguchi[d], Y. Tokura[d,e], and T. Arima[d,e]

[a]Kyoto University.
[b]IMSS, High Energy Accelerator Research Organization.
[c]Comprehensive Research Organization for Science and Society (CROSS).
[d]RIKEN Center for Emergent Matter Science (CEMS)
[e]The University of Tokyo.

Dynamics Fracture Behaviors of Slide-Ring Gels

Mayumi Group

Tough hydrogels have been attracting a lot of interest because of their potential application for biomaterials. To improve the mechanical strength of hydrogels, various chemical design of polymer networks have been proposed in the last two decades. One of the promising strategies to toughen gels is to introduce weak "sacrificial" crosslinks into polymer networks [1]. The sacrificial bonds in tough polymer gels are broken under deformation, and a part of input mechanical energy is dissipated, which leads to the large fracture energy of the dissipative gels. A problem of the dissipative tough polymer gels is their low mechanical recoverability. When reversible bonds (e.g. hydrogen bonds, ionic bonds, etc.) are utilized as sacrificial bonds, the broken sacrificial bonds can be recovered, but it takes a relatively long time (at least minutes) for complete recovery. For the applications as implant biomaterials such as artificial ligaments and prosthetic joints, the mechanical instant recoverability is needed because they should show constant mechanical responses under repeated deformations at a high frequency (e.g. 1 Hz).

Another tough polymer gel is slide-ring (SR) gel, in which polymer chains are cross-linked by ring molecules (Fig.1) [2]. The sliding of the movable cross-links composed of rings homogenizes network structure and reduces stress concentration in polymer networks, which results in high deformability and softness of SR gels. We have been investigating toughening mechanism of SR gels composed of polyethylene glycol (PEG) and cyclodextrin (CD). For conventional polymer gels cross-linked by fixed covalent bonds, the fracture energy is dominated by the strand length between cross-links. In the case of SR gels, the sliding of the cross-links enlarges the strand length and enhances the fracture toughness [3].

A unique feature of SR gels is their high mechanical recoverability. SR gels show no mechanical hysteresis under repeated stretching. This suggests that the sliding movement of the cross-links is faster than breaking/reforming dynamics of the reversible sacrificial cross-links. We systematically investigated the crack propagation behavior of SR gels at

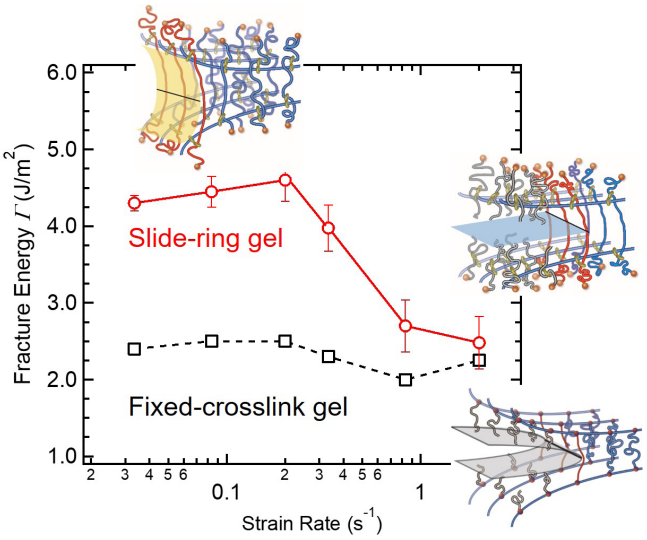

Fig. 1. Strain rate dependence of fracture energy of slide-ring and fixed cross-link gels.

various strain rates to evaluate the sliding dynamics of the movable cross-links [4]. At a certain strain rate and crack propagation velocity, a drastic decrease of the fracture energy was observed (Fig.1). For lower strain rates and crack propagation velocities, the slide-ring cross-links have enough time to slide along the polymer axes, which leads to the enhanced fracture energy. At fast fracture, however, the sliding of cross-links cannot catch up with the network deformation, and the fracture energy decreases to the same level as that of a fixed cross-link gel. From the critical crack propagation velocity at the transition point, we estimated the time scale of the sliding dynamics to be micro-seconds. This result is consistent with the diffusion coefficient of the sliding dynamics for CDs on PEG axis evaluated by a full atomistic molecular dynamics simulation [5]. The fast sliding motion of the cross-links is the origin of the high mechanical recoverability of SR gels under repeated deformations. SR gels exhibits high toughness and mechanical recoverability, which are needed for implant biomaterials and elastomer actuators for soft robots.

References

[1] J. Y. Sun, X. Zhao, W. K. Illeperuma, O. Chaudhuri, K. H. Oh, D. J. Mooney, J. J. Vlassak, and Z. Suo, Nature **489**, 133 (2012).
[2] K. Ito, Polym. J. **39**, 489 (2007).
[3] C. Liu, H. Kadono, K. Mayumi, K. Kato, H. Yokoyama, and K. Ito, ACS Macro Lett. **6**, 1409 (2017).
[4] C. Liu, H. Yokoyama, K. Mayumi, and K. Ito, Mech. Mater. **156**, 103784 (2021).
[5] Y. Yasuda, Y. Hidaka, K. Mayumi, T. Yamada, K. Fujimoto, S. Okazaki, H. Yokoyama, and K. Ito, J. Am. Chem. Soc. **141**, 9655 (2019).

Authors

K. Mayumi. C. Liu. K. Ito[a]

[a]The University of Tokyo

Charge-Fluctuation-Mediated Superconductivity in Organic Complexes

Kindo, Kohama, and Tokunaga Groups

Electron pairing in unconventional superconductors is driven by quantum fluctuations of electronic degrees of freedom. For various unconventional superconductors, such as high-T_c cuprates and heavy-fermion systems, their magnetic degrees of freedom often play an essential role in the pairing mechanisms. Although charge degrees of freedom can also mediate the Cooper-pair formation as exotic pairings, experimental investigation of the charge-fluctuation-mediated superconductivity has been insufficient for detailed discussion because only a few materials show superconductivity with pure charge instability.

The β′′-type organic charge-transfer complexes are known as the candidates showing superconductivity mediated by charge fluctuations. As shown in Fig. 1, the organic molecules in the β′′-type structure are uniformly arranged. Since the valence of each molecule is +0.5, the energy band of the electronic system is 1/4-filled. In this case, it is known that charge density exhibits inhomogeneous distribution in neighboring sites to reduce the intersite Coulomb repulsion when electron correlations are strong. Therefore, it is expected that this charge instability can trigger a superconducting transition. In the present research, we investigated the low-temperature electronic states of some β′′-type materials, β′′-(BEDT-TTF)$_4$[(H$_3$O)M(C$_2$O$_4$)$_3$]G (M=metal ions, G=guest molecules), using various

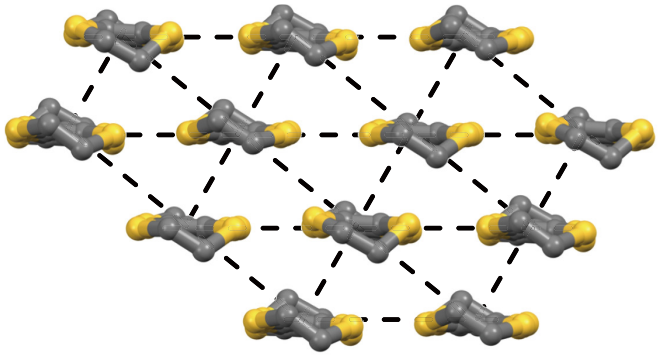

Fig. 1. Molecular arrangement of organic molecules in the conducting plane of the β′′-type organic materials. The dashed lines show predominant transfer integrals between the molecules, forming the distorted triangular lattice.

measurements and unveiled that the superconductivity in this compound is possibly mediated by charge fluctuations [1,2].

Figure 2 shows the high-magnetic-field quantum oscillations in magnetoresistance $\Delta R/R$ of β′′-(BEDT-TTF)$_4$[(H$_3$O)Ga(C$_2$O$_4$)$_3$]PhNO$_2$ at various temperatures. As shown by the dashed envelopes, the amplitude of the oscillations is modulated below 8 K. Detailed analyses with the Lifshits-Kosevich formula indicate that a transition occurs at 8 K, leading to a split of the Fermi pocket and an enhancement of the effective mass. This transition is observed in ultrasonic properties whereas a low-temperature x-ray diffraction measurement detects no significant anomaly at the temperature. Also, this transition has no magnetic field dependence. As orbital degrees of freedom are quenched in the present material, these results mean that a local lattice modulation is induced by charge disproportionation. Just below this transition temperature, this compound shows a transition from the charge disproportionation to the superconducting state at T_c~7 K. By replacement of the guest molecules, T_c is reduced with a decline of the charge disproportionation. This tendency implies that the charge fluctuations enhanced in this compound govern the pairing of the superconductivity.

Besides, we performed heat capacity measurements to determine the gap symmetry of the superconductivity. The temperature, magnetic field, and field-angle dependence of the heat capacity indicates that the gap function is aniso-

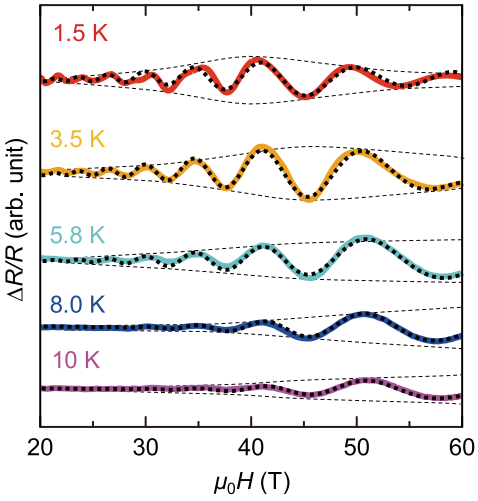

Fig. 2. High-magnetic-field Shubnikov-de Haas oscillations of β′′-(BEDT-TTF)$_4$[(H$_3$O)Ga(C$_2$O$_4$)$_3$]PhNO$_2$ shown as $\Delta R/R$. The dotted curves on the data are fits to a two-component Lifshitz-Kosevich formula. The dashed envelopes are guides for the eye to emphasize the amplitude change.

tropic and has no node on the Fermi surface, distinct from that of nodal *d*-wave symmetry arising from antiferromagnetic spin fluctuations observed in many unconventional superconductors. This full-gapped nature suggests that intersite repulsion, leading to the charge disproportionation, works as an attractive force for the on-site Cooper pairing.

These results indicate that the present superconductivity is formed by the charge fluctuations, and also, elucidate the detailed features of the charge-fluctuation-mediated superconductivity.

References

[1] S. Imajo, H. Akutsu, A. Akutsu-Sato, A. L. Morritt, L. Martin, and Y. Nakazawa, Phys. Rev. Res. **1**, 033184 (2019).

[2] S. Imajo, H. Akutsu, R. Kurihara, T. Yajima, Y. Kohama, M. Tokunaga, K. Kindo, and Y. Nakazawa, Phys. Rev. Lett. **125**, 177002 (2020).

Authors

S. Imajo, R. Kurihara, Y. Kohama, M. Tokunaga, and K. Kindo

Magnetic-Field-Induced Insulator-Metal Transition in a Strongly Correlated Insulator $V_{1-x}W_xO_2$ at 500 T

Y. H. Matsuda and Takeyama Groups

The magnetic ground state of most of strongly correlated insulators is antiferromagnetic ordered state. Roles of electron spins in realizing the insulating nature in correlated systems is well understood in the single-band Hubbard model; the magnetic energy determined by the exchange interaction J is much smaller than the Coulomb energy *U*, and thus the electrical insulating nature is essentially insensitive to the magnetic state. In some of actual materials, however, spin degree of freedom couples to crystal lattice through the orbital degree of freedom and results in nontrivial electronic states. Actually, in some of the strongly correlated insulators, the ground state exhibits spin-singlet state instead of the antiferromagnetic state. One of the most studied correlated insulators with the singlet ground state is VO_2 that undergoes a very sharp metal-insulator transition at 340 K. It has been debated for more than 60 years whether

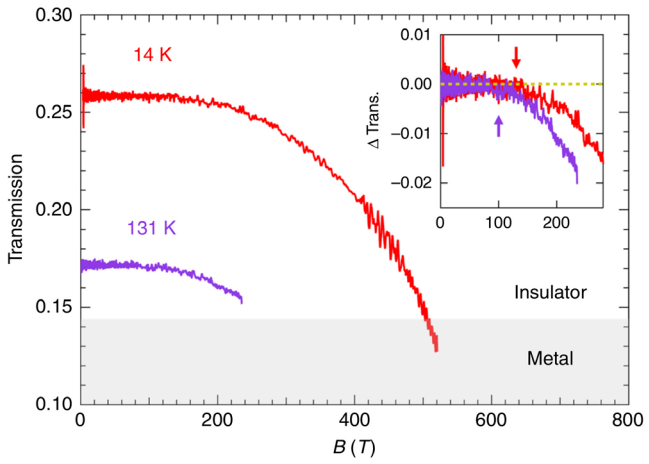

Fig. 1. Magnetic-field dependence of the optical transmission at 14 and 131 K. The transmission is plotted before the breaking point of the destructive measurement. The shaded area indicates transmission lower than that in the high-temperature metallic phase at 291 K. Inset: transmission change ΔTrans. as a function of the magnetic field. The dashed yellow line corresponds to ΔTrans.= 0. The red and purple arrow indicate the field positions (B*) where ΔTrans. deviates from zero.

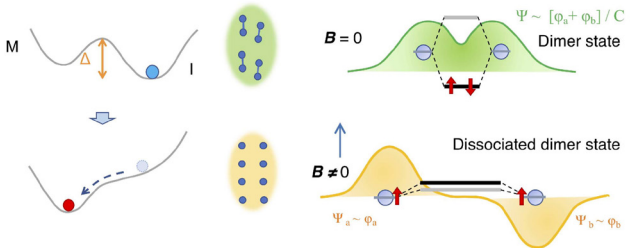

Fig. 2. Schematic of the magnetic-field-induced insulator-metal (IM) transition. The left side shows that the potential barrier Δ is lowered by the Zeeman energy. The middle part schematically shows the collapse of the V–V dimers. The right part shows that applying a magnetic field induces the dissociation of the dimer owing to the destabilization of formation of the bonding state Ψ of the molecular orbital, where φa and φb are the wave functions of the independent vanadium ions.

the electron correlation or the structural instability is more essential driving force behind the transition.

In the present work, we have demonstrated that a tungsten (W)-doped VO_2 undergoes insulator-metal (IM) transition by applying a ultrahigh magnetic field of 500 T. The field is produced by the electromagnetic flux compression 1000-T generator at the ISSP [1]. Figure 1 shows the magneto-transmission of a $V_{0.94}W_{0.06}O_2$ thin film at 1.977 μm [2]. A reduction of the transmission with magnetic field when the field is greater than 100 T is a direct evidence of the field induced metallization. One of the most probable explanation for the field-induced IM transition is that the singlet-dimer state is suppressed by such a ultrahigh magnetic field, and which results in breaking of structural V-V dimers as well. The molecular orbital occupied by two electrons with different spin directions is collapsed by forced alignment of the two spins by the strong magnetic field of 500 T. The discovered spin-controlled IM transition suggests that the principal driving force to the insulating state at a low temperature is structural instability (formation of dimers) rather than the electron correlation.

From another view point, the observed collapse of the V-V dimer is a similar phenomenon with the so-called the chemical catastrophe where a chemical bond is destroyed by the Zeeman effect of a super-strong magnetic field greater than 10^6 T in the cosmic space [3]. An energy to collapse the molecular orbital of the V-V dimer is scaled down by 3-4 orders of magnitude in a solid compared to a normal molecule, which enable us to observe the chemical catastrophe in a solid. Figure 2 is a schematic of the field-induced IM transition of W-doped VO_2; the V-V dimers are dissociated by forced alignment of spins in a 500-T-field [2].

References

[1] D. Nakamura, Akihiko Ikeda, H. Sawabe, Y. H. Matsuda, and S. Takeyama, Rev. Sci. Instrum. **89**, 095106 (2018).

[2] Y. H. Matsuda, D. Nakamura, A. Ikeda, S. Takeyama, Y. Suga, H. Nakahara, and Y. Muraoka, Nat. Commun. **11** 3591 (2020).

[3] M. Date, Australian Journal of Physics **48**, 187 (1995).

Authors

Y. H. Matsuda, D. Nakamura, A. Ikeda, S. Takeyama, Y. Suga[a], H. Nakahara[a], and Y. Muraoka[a]

[a]Okayama University

Capacitive Detection of Physical Quantities in Pulsed Magnetic Fields

Tokunaga Group

Capacitance is known as a physical quantity that can be measured with high precision. We have developed a system to precisely measure various physical quantities that change in pulsed high magnetic fields using high-speed capacitance measurements [1].

First, we measured magnetostriction. We attach a pair of electrode plates on top of a sample and on the probe with keeping a small gap between them. We can detect small change in the sample length through the change in the capacitance of this setup. Using this method, we observed magnetostriction in a Heusler alloy caused by a significant magneto-volume effect [2]. The entropy change associated with this magneto-volume effect is regarded as the origin of the giant inverse magneto-caloric effect observed in this class of materials [2,3]. Therefore, quantitative evaluation of the structural change can be essential to understand the magnetocaloric effect. In non-magnetic metals, magneto-striction can be used to detect the field-induced changes in band filling. Utilizing this technique, we achieved thermodynamic evidence of complete valley polarization in elemental bismuth in the ultra-quantum limit state [4].

Capacitance measurements are also valuable for studying multiferroic materials in which magnetic order correlates with the dielectric property. If the change in magnetic symmetry makes the crystal polar, we can detect it through electric polarization measurements. On the other hand, the change is hardly discernible in the polarization if the spin order does not break global inversion symmetry, such as in the antiferroelectric state. Our capacitive measurement of dielectric constants enabled to detect this kind of change in symmetry at high magnetic fields. Figures 1 show the magnetization and dielectric constant of single crystals of $Pb(TiO)Cu_4(PO_4)_4$. In contrast to the broad hump structure in the magnetization curve, dielectric constant shows a steep change around 26 T with field hysteresis, which unambiguously indicates the change in magnetic symmetry at this field. This technique provides us with a novel tool to identify the symmetry of magnetic phases emerging in high magnetic fields.

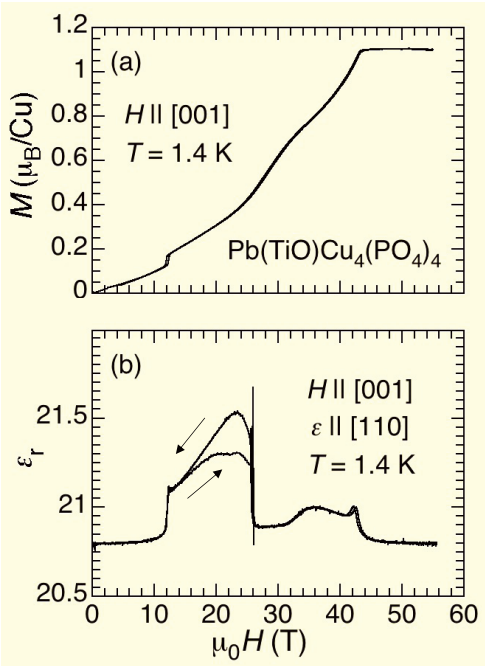

Fig. 1. Field dependence of (a) magnetization and (b) real part of the relative dielectric constant of $Pb(TiO)Cu_4(PO_4)_4$. Successive transitions of cluster spin multipole order show up as multiple anomalies in both physical quantities. Broad hump structure in magnetization around 26 T becomes prominent in the dielectric constant measured using the capacitance method.

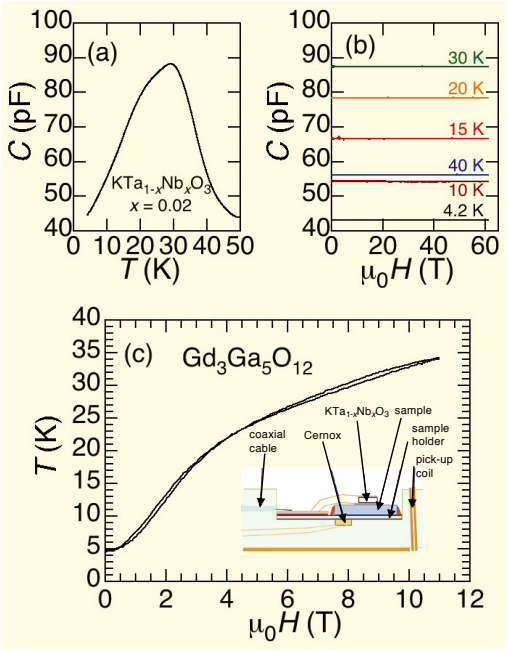

Fig. 2. (a) Temperature variation of the capacitance of $KTa_{1-x}Nb_xO_3$ at zero magnetic field. (b) Magnetic field dependence of the capacitance of $KTa_{1-x}Nb_xO_3$ at various temperatures. These two results indicate that this material can be used as a capacitance thermometer insensitive to a magnetic field. (c) Magnetocaloric effects in $Gd_3Ga_5O_{12}$ measured using this capacitance thermometer. The inset shows schematics of the experimental setup. Our fast capacitance measurements enable to evaluate the magnetocaloric effect in this material in a pulsed magnetic field.

By measuring dielectric constants of some non-magnetic materials attached to a sample, we can evaluate the temperature change of a sample in magnetic fields: the so-called magneto-caloric effect. We show an example of the measurements of the magneto-caloric effect using $KTa_{1-x}Nb_xO_3$ (x = 0.02) as a capacitance thermometer, whose dielectric constant has a temperature dependence as shown in Fig. 2(a). We have previously developed a similar system to measure the magneto-caloric effect using a thin-film resistance thermometer [5]. Although this method works effectively, we have to calibrate the effect of magnetoresistance in the thermometer in advance at each temperature. On the other hand, in the present capacitance thermometer, the capacitance is almost insensitive to the applied magnetic field, as shown in Fig. 2(b). Using this thermometer, we can successfully measure the magneto-caloric effect of a magnetic refrigerant $Gd_3Ga_5O_{12}$ in a pulsed magnetic field (Fig. 2(c)). Due to the non-magnetic nature of this thermometer, we can also measure magnetocaloric effects simultaneously with magnetization. Such simultaneous measurements will enable us to precisely determine the field-temperature phase diagram of all the kind of magnetic materials and to discuss more precise thermodynamics.

High precision measurements of capacitance improve evaluation of the structure, symmetry, and entropy changes of the sample in pulsed magnetic fields. We expect that such a technological innovation will open up new horizons in science at high magnetic fields.

References
[1] A. Miyake *et al*., Rev. Sci. Instrum. **91**, 105103 (2020).
[2] T. Kihara *et al*., Phys. Rev. Mater. **5**, 034416 (2021).
[3] T. Kihara *et al*., Phys. Rev. B **90**, 214409 (2014).
[4] A. Iwasa *et al*., Sci. Rep. **9**, 1672 (2019).
[5] T. Kihara *et al*., Rev. Sci. Instrum. **84**, 074901 (2013).

Authors
A. Miyake, H. Mitamura, S. Kawachi, K. Kimura[a], T. Kimura[a], T. Kihara[b], M. Tachibana[c], and M. Tokunaga
[a]The University of Tokyo
[b]IMR, Tohoku University
cNational Institute for Material Science

Generation of Long Pulsed-Magnetic Fields by Using Electric-Double-Layer-Capacitors

Kohama Group

The generation of pulsed magnetic fields was first achieved by Pyotr L. Kapitsa approximately a century ago. After his pioneering work, various power supplies were tested for pulsed field generation. The most common power supply for generating a pulsed magnetic field is the high-voltage and high-speed capacitor bank. However, such a capacitor bank has small value of capacitance (C = 1 – 100 mF) and consequently restricts the available range of pulsed duration up to ~0.1 s. The short pulse duration makes it difficult to put pulsed magnets to widespread use. Developing an alternative power supply for generating pulsed high magnetic fields is a demanding task in high magnetic field science.

In this study, we have reported a power supply based on an electric-double-layer-capacitor (EDLC) which is composed of a series connection of 336 EDLC cells [1]. This system has a total capacitance of 10.7 F and can store the energy of 3.87 MJ with the charged voltage of 860 V. We find that the EDLC based power supply can generate high magnetic field up to 30 T with pulse duration of ~1 s. Because of the low-cost and compact design of developed EDLC based power supply, our system can be used in many research and industrial fields.

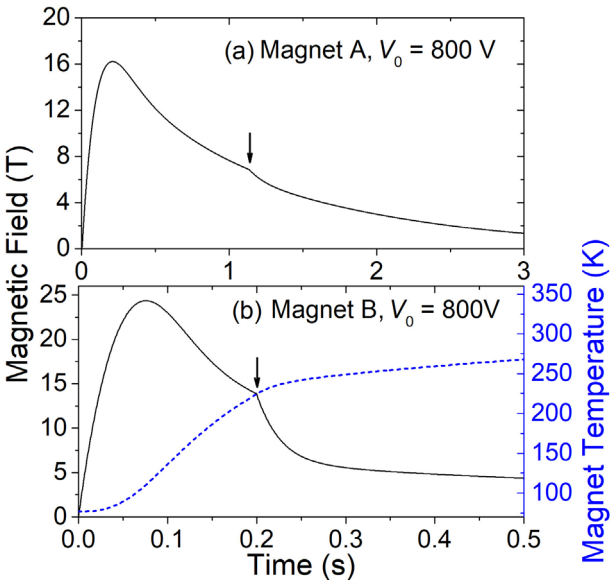

Fig. 1. Pulsed Field Profile generated by the EDLC based power supply. (a) Magnetic field profile generated with low-impedance pulsed magnet. (b) Magnetic field profile generated with high-impedance pulsed magnet. The right axis represents the calculated magnet temperature.

Figure 1a and b show the pulsed field profiles generated by our EDLC system. The arrows in Fig. 1 indicates the timing of the closing an energy bifurcation thyristor, which leads to an intentional reduction of the pulsed current. Due to the large capacitance of EDLC bank, we could observe the overdamped-like waveform for the setup A (Fig. 1a), which has long pulse duration of ~ a few seconds. The peak values of the fields (currents) are 16.2 T and 23.9 T (5.91 kA and 4.39 kA) for setup A and setup B (Fig.1b). The peaks of the fields shift to later times with decreasing charged voltage and indicate the strong influence of Joule heating on the pulsed field profile. Indeed, the calculated temperature of the pulsed magnet as shown in the right axes in Fig. 1(b) clearly shows the large Joule heating effect. In the paper, we have also reported how the pulsed field profile is influenced by the capacitance, internal resistance, coil resistance, charged voltage, coil inductance (not shown in this material) and found that a suitable choice of the coil design could increase accessible field strength up to 30 T and enhance pulsed duration up to a few seconds.

In summary, we have developed the EDLC based power supply which is cost-effective and compact discharge system and can generate strong magnetic fields with long duration. These systems can be used for many research fields such as nuclear magnetic resonance and neutron scattering experiments, which typically require long accumulation times to achieve good signal/noise ratios. In addition, we have confirmed that the generated pulsed field profile is well described by a series-connected RLC model with taking Joule heating into account. Finally, we note that connecting several EDLC units in parallel and series can generate a strong pulsed field of more than 30 T with a long time duration of a few seconds.

Reference
[1] K. Matsui, T. Kanda, Y. Ihara, K. Kindo, and Y. Kohama, Rev. Sci. Instrum. **92**, 024711 (2021).

Authors
K. Matsui, T. Kanda, Y. Ihara[a], K. Kindo, and Y. Kohama
[a]Hokkaido University

Observation of the Quantum Shift of a Backward Rescattering Caustic by Carrier-Envelope Phase Mapping

Itatani Group

When an atom or molecule is exposed to linearly-polarized intense optical fields, an electron wavepacket is freed from the atom, accelerated by the field, then collides with the parent ion. This process, recollision, is the fundamental of attosecond science. When recollision becomes recombination, the ionizing atoms emits a high energy photon (high harmonic generation). Meanwhile, it is well known that a part of recolliding events becomes elastic scattering. Especially the backward rescattering leads to the generation of high-energy electrons with a drift kinetic energy up to $10U_p$, where U_p is the ponderomotive potential. Recent theoretical progress of the adiabatic theory of rescattering gives an analytical formula for photoelectron momentum distributions (PEMDs) near the $10U_p$ cutoff which is scaled by the cutoff energy. Although the theoretical treatment of rescattering is fully quantum mechanical and straightfor-

ward, the experimental verification has been very difficult because it is not easy to realize systematic experiments to extract well-defined single rescattering events with multi-cycle laser pulses.

We hereby used intense few-cycle pulses in infrared to measure the backward PEMDs with controlled carrier-envelope phases (CEPs). The extremely short duration of the optical pulse allows to extract the single rescattering events of the three highest energies, and the CEP control enables to systematically change the maximum intensity in the focused volume without affecting the other parameters such as spatial distribution of the field intensity. Figure 1 shows the CEP dependent PEMDs with a pulse energy of 210 μJ. Dashed and solid curves represent classical and quantum caustics. The CEP dependent PEMD assures the one-to-one correspondence of the electron momentum at the instance of rescattering and the CEP, which we call the CEP mapping method. From this CEP mapping, we successfully determined the field intensity and the pulse duration to be 2.6×10^{13} W/cm^2 and 13.8 fs, respectively. Using these parameters, the observed PEMDs are deconvolved to three PEMDs that correspond to the rescattering events of different intensities within a single optical pulse, as shown in Fig. 2.

The laser parameters, elastic scattering differential cross sections, and tunnel ionization rate of the taget are encoded in PDMDs. Such information can be extracted from the observed PEMDs based on the adiabatic theory. Based on the quantitative agreement of the observed cutoff behavior of PEMDs with the adiabatic theory, elastic scattering cross section as a function of scattering momenta is successfully determined as shown in Fig. 3.

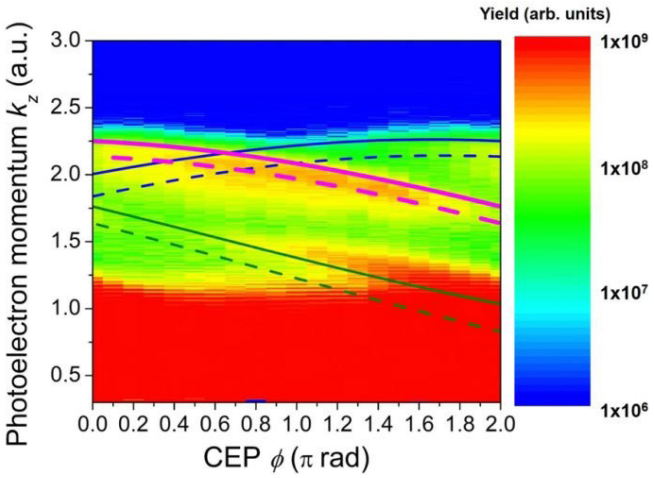

Fig. 1. Measured PEMDs as a function of CEP at a pulse energy of 190 μJ. Dashed and solid curves represent classical and quantum causitcs at the intensity of 2.6×10^{13} W/cm^2 and pulse duration of 13.8 fs.

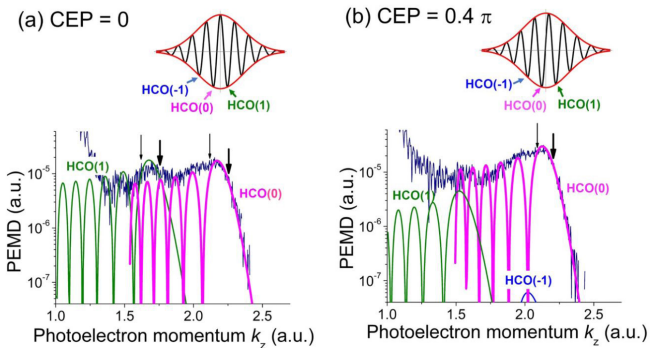

Fig. 2. Measured PEMDs at CEP=0 and 0.4π at an estimated intensity of 2.6×10^{13} W/cm^2 and a pulse duration of 13.8 fs. The thick red, thin blue, and thin green curves show calculated PEMDs corresponding to a half cycle of the electric field as depicted in the top figures. Thin and thick arrows indicate the classical and quantum caustics, respectively.

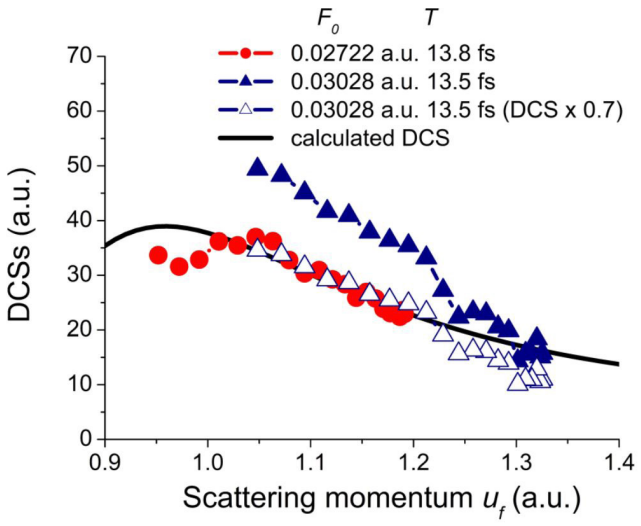

Fig. 3. Extracted DCSs of Xe+ for estimated field amplitudes of 0.02722 (circle) and 0.03028 a. u. (closed triangle) as a function of the rescattering momentum. The black curve represents calculated DCSs.

In summary, we experimentally and theoretically explored the rescattering PEMDs of a Xe atoms near the cutoff using CEP-stable few-cycle pulses [1]. The observed PEMDs are well reproduced by the analytical formula of the adiabatic theory including the quantum shift of the caustics. The results not only demonstrate the fact that the CEP mapping method with the adiabatic rescattering theory allows to extract well-defined elastic scattering, but also opens an opportunity to use rescattering to observe novel electron states such as vortex electrons [2].

References

[1] T. Mizuno, N. Ishii, T. Kanai, P. Rosenberger, D. Zietlow, M. F. Kling, O. Tolstikhin, T. Morishita, and J. Itatani, Phs. Rev. A **103,** 043121 (2021).

[2] O. I. Tolstikhin and T. Morishita, Phys. Rev. A **99**, 063415 (2019).

Authors

T. Mizno, N. Ishii, T. Kanai, P. Rosenberger[a], D. Zietlow[a], M. F. Kling[a, b], O. Tolstikhin[c], T. Morishita[d], and J. Itatani

[a]Ludwig-Maximillians-Universität München

[b]Max Planck Institute for Quantum Optics

[c]Moscow Institute of Physics and Technology

[d]The University of Electro-Communications

Observation of Small Fermi Pockets in a Copper Oxide High-T_c Superconductor

Kondo and Kohama Groups

High-temperature superconductivity is one of the most significant discoveries in physics in the latter half of the 20th century. Since the discovery of high-temperature superconductivity in 1986, their physical properties have been intensively studied from various aspects. However, a unified understanding of the mechanism for high-temperature superconductivity has not yet been established. The most basic and important issue relevant to it is the relationship between antiferromagnetic state forming Mott insulator and high-temperature superconductivity induced by carrier doping.

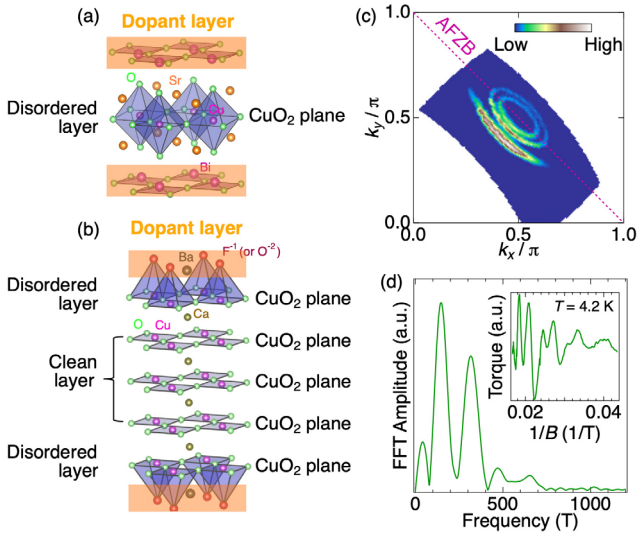

Fig. 1. (a) Crystal structure of single-layer cuprate superconductor ($Bi_2Sr_2CuO_{6+\delta}$ is presented as an example). (b) Crystal structure of 5-layer cuprate superconductor, $Ba_2Ca_4Cu_5O10(F,O)_2$, we have focused on in this study. (c) Fermi surfaces of $Ba_2Ca_4Cu_5O_{10}(F,O)_2$ observed by laser-ARPES. (d) Quantum oscillation measurements for the same compound.

In this study, we focused on a multi-layered cuprate high-T_c superconductor (Fig. 1b) with a clean superconducting plane (CuO_2 layer) that is structurally flat and has charges uniformly distributed along the plane. Here we perform laser-based angle-resolved photoelectron spectroscopy (ARPES) with high energy resolution and quantum oscillation measurement at a strong magnetic field and present the first observation of small Fermi pockets formed in the close vicinity of the Mott insulating phase. Furthermore, we find the coexistence of antiferromagnetism and high-temperature superconductivity in the same CuO_2 sheet.

Superconductivity of cuprate superconductors occurs via carrier doping to the CuO_2 layers from the dopant layers sandwiching them. The main target in previous studies was for structurally simple compounds with one or two CuO_2 planes per unit cell (Fig. 1a). While these have the advantage to be easy in synthesizing, it has been pointed out that the direct contact of the dopant layers to the superconducting layers causes structural distortion and non-uniform charge distribution along the CuO_2 plane, leading to disordered electronic states. To solve this problem, we selected a multilayer system with five CuO_2 planes per unit cell, $Ba_2Ca_4Cu_5O_{10}(F,O)_2$, for a study (Fig. 1b).

This compound has inner CuO_2 planes that can avoid direct contact to the dopant layers. These inner CuO_2 planes are structurally flat, and at the same time, protected by the outer CuO_2 plane from the dopant layers causing the effects of spatially non-uniform carrier doping and defects. Therefore, this multilayered system gives us an excellent opportunity to study an extremely clean superconducting layer that is close to the ideal case treated in theoretical studies.

By performing high-resolution laser-ARPES and quantum oscillation measurements for the clean superconducting layers (Fig. 1c), we successfully observed small Fermi pockets, which had been theoretically expected yet elusive for more than 30 years of research for cuprates. The spectra of Fermi pockets are much sharper in energy than that of Fermi arc, indicating that the pockets we observed indeed come from the inner CuO_2 plane protected from the random potential induced by dopant layers. Moreover, we have confirmed the existence of *d*-wave superconducting gap around the Fermi pockets, providing spectroscopic evidence for the coexistence between antiferromagnetism and superconductivity in the same CuO_2 sheet.

Our results are expected to facilitate the experimental and theoretical research pursuing the mechanism of high-temperature superconductivity in cuprates. In particular, these will contribute to solving the long-standing puzzle of the Fermi arc phenomena and urge the need for revisiting the Mott physics leading to the electron pairing in cuprates, which, up to now, has been based mainly on the research on single- and double-layered compounds with inhomogeneous electronic states.

References

[1] S. Kunisada *et al.*, Science **369**, 833 (2020).

Authors
S. Kunisada, S. Isono[a], Y. Kohama, S. Sakai[b], C. Bareille, S. Sakuragi, R. Noguchi, K. Kurokawa, K. Kuroda, Y. Ishida, S. Adachi[c], R. Sekine[a], T.K. Kim[d], C. Cacho[d], S. Shin, T. Tohyama[a], K. Tokiwa[a] and T. Kondo
[a]Tokyo University of Science
[b]RIKEN Center for Emergent Matter Science (CEMS)
[c]MANA, National Institute of Material Science
[d]Diamond Light Source

Higher-Order Topological Insulator Built from van der Waals Stacking of Bismuth-Halide Chains

Kondo Group

A Z_2 weak topological insulator (WTI) state can be formed in a material with stacked quantum spin Hall insulators (QSHIs), where the topological surface states appear only on side surfaces by accumulating helical edge states of QSHIs [1]. Similarly, a higher-order topological insulator (HOTI) is expected to be built from stacking QSHIs so that 1D helical hinge states are formed by accumulating the edge states. Utilizing symmetry-based indicators, the HOTI phases have been predicted in materials which were previously regarded as trivial insulators [2]. So far, only bulk bismuth has been experimentally shown to be in the HOTI phase [3]. However, bismuth is a semimetal, whose bulk cannot become insulating by carrier doping. Therefore, the experimental realization of a HOTI in an insulating material has been awaited.

In this study, we propose that quasi-1D bismuth halides offer a novel platform to investigate various topological phases that depend on the stacking sequences of Bi_4X_4 (where X is I or Br) chains. A WTI state has been observed in β-Bi_4I_4 with single-layered chains per unit cell, while a normal insulator state has been obtained in α-Bi_4I_4, which takes a double-layered structure (Fig. 1) [1]. Although Bi_4Br_4 also consists of double layers, each layer is alternately rotated by 180 degrees, leading to the prediction of a HOTI phase due to the slight shift of the inversion center in the unit cell. Based on this, we present angle-resolved photoemission spectroscopy (ARPES) results showing that Bi_4Br_4 is a HOTI for the first time as a real 3D material [4].

An advantage of employing quasi-1D materials lies in the formation of a number of steps aligned parallel to the chain direction on the cleavage surface. Figure 2(a) shows a photographic image of ribbon-like Bi_4Br_4 crystals used in the experiments. While the cleaved surface is relatively rough, as shown in Fig. 2(b), Grazing incidence Small-angle X-ray

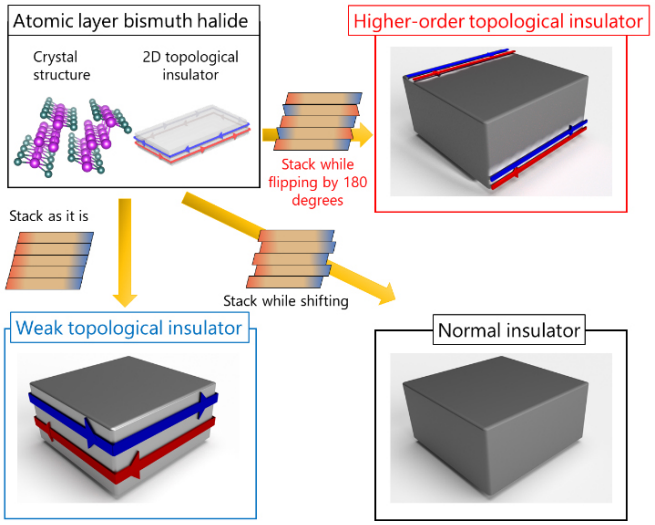

Fig. 1. Schematic of the various topological properties realized by stacking quasi-1D bismuth halide chains.

Scattering (GISAXS) measurements has revealed that the surface consists only of the top (001) surface and the side (100) surface. This result indicates that a huge number of hinges between the two planes are exposed on the cleaved surface, offering the possibility of detecting the topological hinge states by ARPES measurements.

Figure 2(c) presents the ARPES result of Bi_4Br_4 taken by high-resolution laser-ARPES. The strong photoemission signals observed at ~0.6 eV below the Fermi level (E_F) are assigned to the bulk valence band. Interestingly, we also observed metallic in-gap states with Dirac-like dispersions around EF (bottom panel of Fig. 2(c)). This is further confirmed in the momentum distribution curves at the energy of the roughly estimated Dirac point (middle panel of Fig. 2(c)). The in-gap states are found to form a quasi-1D intensity distribution in the Fermi surface mapping. These observations are in stark contrast to the case for a trivial insulator α-Bi_4I_4, where no indication for in-gap states is found in ARPES image or the corresponding momentum distribution curve (Fig. 2(d)). Therefore, the 1D Dirac state in Bi_4Br_4 is attributed to the topological states, demonstrating the realization of the HOTI phase in Bi_4Br_4. Our comprehensive study on bismuth halides also shows that the difference in chain stacking is the origin of the different band topologies among Bi_4Br_4, α-Bi_4I_4, and β-Bi_4I_4. The quasi-1D HOTI state we have verified in this study will bring the new capability of designing and engineering functional materials utilizing the stacking-dependence of the topological phases.

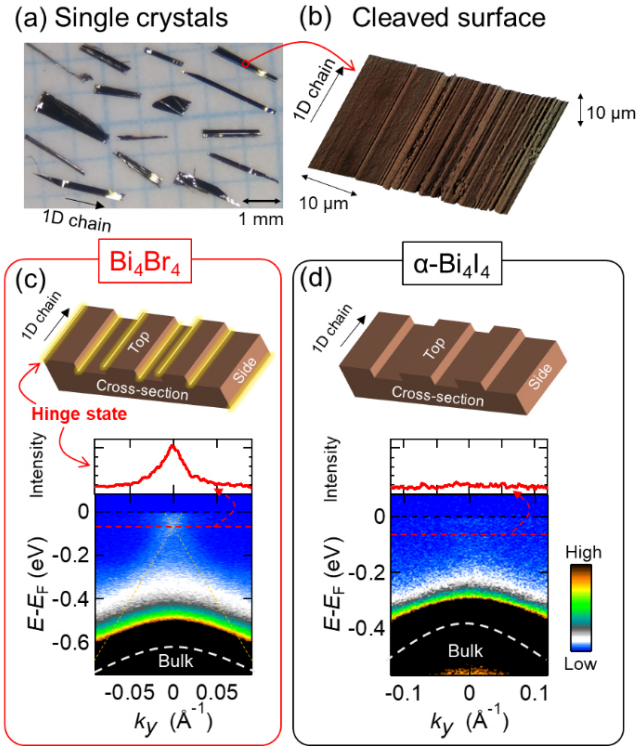

Fig. 2 (a) Photograph of Bi_4Br_4 crystals. (b) Laser microscope image of a cleaved surface. (c) ARPES band map of Bi_4Br_4 around the $\bar{\Gamma}$ point (bottom) and the corresponding momentum distribution curve at E-E_F=-60 meV (middle). Schematic of the cleaved surface of Bi_4Br_4 with topological hinge states (top). (d) Similar results to (c), but for α-Bi_4I_4.

References

[1] R. Noguchi *et al*., Nature **566**, 518 (2019).
[2] F. Tang, H. C. Po, A. Vishwanath, and X. Wan, Nat. Phys. **15**, 470 (2019).
[3] F. Schindler et al., Nat. Phys. **14**, 918 (2018).
[4] R. Noguchi et al., Nat. Mater. (2021). https://doi.org/10.1038/s41563-020-00871-7

Authors

R. Noguchi, M. Kobayashi[a], Z. Jiang[b], K. Kuroda, T. Takahashi[a], Z. Xu[b], D. Lee[b], M. Hirayama[c], M. Ochi[d], T. Shirasawa[d], P. Zhang, C. Lin, C. Bareille, S. Sakuragi, H. Tanaka, S. Kunisada, K. Kurokawa, K. Yaji, A. Harasawa, V. Kandyba[f], A. Giampietri[f], A. Barinov[f], T. K. Kim[g], C. Cacho[g], M. Hashimoto[h], D. Lu[h], S. Shin, R. Arita[c,i], K. Lai[b], T. Sasagawa[a], and T. Kondo

[a]Tokyo Institute of Technology
[b]University of Texas at Austin
[c]RIKEN Center for Emergent Matter Science (CEMS)
[d]Osaka University
[e]National Metrology Institute of Japan, National Institute of Advanced Industrial Scienceand Technology
[f]Elettra Synchrotron Trieste
[g]Diamond Light Source
[h]Stanford Synchrotron Radiation Lightsource, SLAC National Accelerator Laboratory
[i]The University of Tokyo

Observation and Control of the Weak Topological Insulator State in $ZrTe_5$

Kondo Group

A quantum spin Hall insulator hosts topological states at the one-dimensional (1D) edge, along which backscattering by nonmagnetic impurities is strictly prohibited. Its 3D analogue, a weak topological insulator (WTI), possesses similar quasi-1D topological states confined at side surfaces. The enhanced confinement could provide a route for dissipationless current and better advantages for applications relative to strong topological insulators (STIs) [1]. However, the topological side surface is usually not cleavable and is thus hard to observe.

$ZrTe_5$ was predicted to be a WTI candidate at the early stage of exploring WTIs [2]. This compound exhibits very high mobility, thus it has been regarded as a promising platform for devices. Nonetheless, the topological property of $ZrTe_5$ has not been experimentally identified to date because the observation of band structure on the side surface has not been successful so far. All the previous surface-sensitive studies were carried out on the top surface, which only confirms the lack of surface states; whether or not this material is topological, therefore, has not been determined beyond speculation. Another difficulty for this study is that

$ZrTe_5$ is in proximity to multiple topological phases, whereas this feature could bring an attractive functionality of controlling bulk topology by fine-tuning a physical parameter.

In this study, we visualize the topological states of $ZrTe_5$ by spin- and angle- resolved photoemission spectroscopy (ARPES): a quasi-1D band with spin-momentum locking was revealed on the side surface. We further demonstrate that the bulk band gap is controlled by external strain, realizing a more stable WTI state or an ideal Dirac semimetal (DS) state. The highly directional spin-current and the tunable band gap in $ZrTe_5$ will provide an excellent platform for applications [3].

$ZrTe_5$ has a quasi-1D crystal structure. In principle, it should be possible to cleave both top and side surfaces. Along the lattice *b* direction, the layers are stacked by van der Waals forces, and a clean surface can be easily obtained by cleavage. Instead, Te–Te bonding exists between adjacent layers along the lattice *c* direction, causing much more difficulty in cleaving the side *a*-*b* surface. In this work, we successfully cleaved the side *a*-*b* surface with a top post and silver epoxy. The problem, however, is that the cleaved areas are very small and inhomogeneous. With a synchrotron-based nano-ARPES (spot size < 1 μm), we took real space maps of photoemission intensity on several samples, as sketched in Fig. 1(a). It is found that the typical dimension of cleaved areas is around or smaller than 50 μm (Fig. 1(b)).

In *k*-space, a quasi-1D Fermi surface is exhibited by plotting ARPES intensities about the Fermi level, which shows no dispersion along lattice *b* direction (Fig. 1(d)). Along the lattice *a* direction, the band shows a hole-like dispersion (Fig. 1(c)). With different photon energies (74 eV and 7 eV), we did not find any change for this band, which support its surface origin (no k_z dispersion). For the topological surface state, spin polarization is expected. To confirm this, we have used spin-resolved ARPES to check

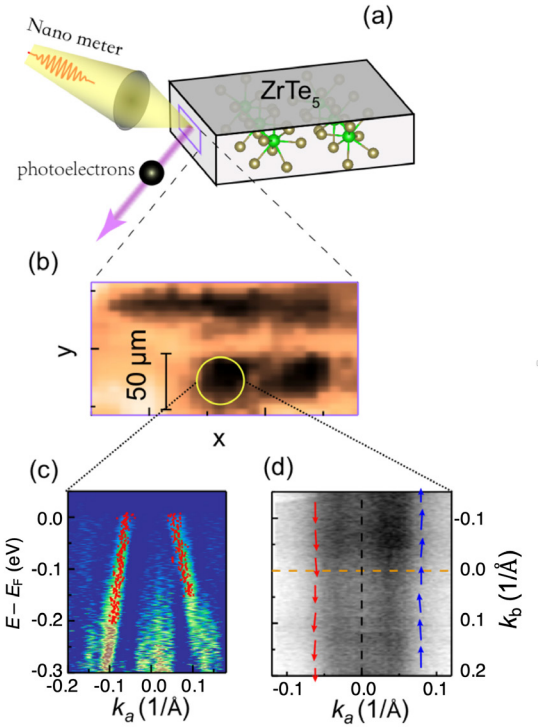

Fig. 1. ARPES measurements with nano-ARPES on the side surface. (a) Schematic of the experimental setup. (b) Real space intensity mapping with nano- ARPES. The signal is clear only within an area of 50 μm. (c) Band structure along the chain direction. The hole-like band is one of the topological surface band. (d) Fermi surface of the surface band in (c). Its spin-texture is indicated by red and blue arrows.

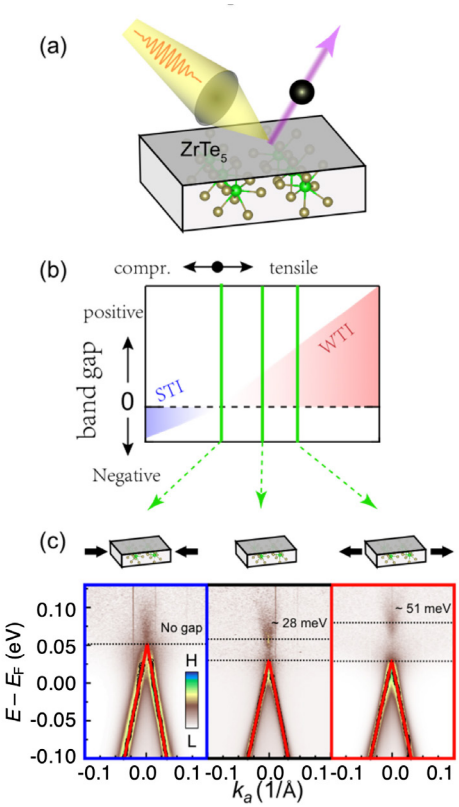

Fig. 2. ARPES measurements with laser-ARPES on the top surface with strain. (a) Schematic of the experimental setup. (b) Topological phase diagram of $ZrTe_5$ with different strain along chain direction. (c) Band structure observed from the top surface with different strain.

the spin texture of the surface band. A clear spin polarization is detected along the lattice *b* direction. In contrast, the spin polarization is almost zero along the lattice *a* and *c* directions, as indicated by red and blue arrows in Fig. 1(d). Therefore, the band is spin-polarized along the *b*-direction with spin-momentum locking, consistent with the spin-texture of WTIs with a quasi-1D dispersion.

On the top surface (Fig. 2(a)), we observe a small bulk gap (~ 28 meV), as shown in the middle panel of Fig. 2(c), which indicates that the WTI state in $ZrTe_5$ is protected only marginally from external perturbations. Theoretical calculations proposed that the band gap changes with external strain. Thus, we further designed a strain device and checked the strain dependence of band structure in $ZrTe_5$. Both compressive strain and tensile strain are applied along the chain direction of $ZrTe_5$. The band structures under different strains are displayed in Fig. 2(c). The sample with no strain shows a band gap of ~28 meV. With tensile strain, the band gap is enlarged to ~ 51 meV. In contrast, we could reduce the band gap by compressive strain, even realizing a Dirac semimetal state with no band gap. In Fig. 2(b), we summarized the topological phases of $ZrTe_5$ with different strains.

Our results demonstrate the existence and tunability of the WTI states in $ZrTe_5$. The spin-momentum locked quasi-1D surface states and the strain-tunable bulk gap make $ZrTe_5$ an ideal platform for 2D devices and spin engineering.

Reference

[1] R. Noguchi *et al.*, Nature, **566**, 518 (2019).
[2] H. Weng, X. Dai, and Z. Fang, Phys. Rev. X **4**, 011002 (2014).
[3] P. Zhang *et al.*, Nature Commun. **12**, 406 (2021).

Authors
P. Zhang, R. Noguchi, K. Kuroda, C. Lin, K. Kawaguchi, K. Yaji[a], A. Harasawa, M. Lippmaa, S. Nie[b], H. Weng[c], V. Kandyba[d], A. Giampietrid, A. Barinovd, Q. Li[e], G.D. Gu[e], S. Shin[f], and T. Kondo
[a]National Institute for Materials Science
[b]Stanford University
[c]Chinese Academy of Sciences
[d]Elettra - Sincrotrone Trieste
[e]Brookhaven National Laboratory
[f]The University of Tokyo

Bose-Einstein Condensation Superconductivity Induced by Disappearance of the Nematic State

Okazaki Group

The crossover from the superconductivity of the Bardeen-Cooper-Schrieffer (BCS) regime to the Bose-Einstein condensation (BEC) regime holds a key to understanding the nature of pairing and condensation of fermions. Figure 1a shows a canonical phase diagram of BCS-BEC crossover. Weak-coupling Bardeen-Cooper-Schrieffer (BCS) pairing and strong-coupling Bose-Einstein condensation (BEC) are connected continuously through the BCS-BEC crossover regime. This regime holds a key to understanding the nature of pairing and condensation of particles. In the weak-coupling BCS regime, the dispersion of the Bogoliubov quasiparticle (BQP) shows the characteristic back-bending near k_F, which is downward convex around $k = 0$ in the case of a hole band below E_F, as shown in Fig. 1b, where k is the crystal momentum of electrons. On the other hand, in the strong-coupling BEC regime, the dispersion with a minimum

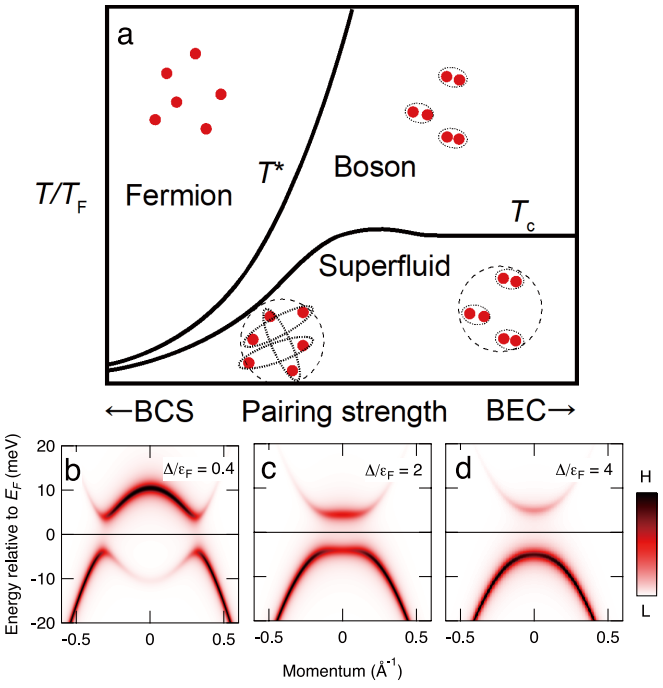

Fig. 1. Phase diagram of the BCS-BEC crossover and BQP band dispersions. (a) Canonical phase diagram of BCS-BEC crossover. T_c and T^* are condensation and pairing temperatures, respectively. As the pairing strength increases, T^* and T_c become separate, and a pseudogap is expected at $T^* > T > T_c$. (b)-(d) BQP band dispersions in the BCS regime, the crossover regime, and the BEC regime, respectively. The dispersion is downward convex around $k = 0$ for the BCS regime, becomes flat in the crossover regime, and then becomes upward convex in the BEC regime, because of the chemical potential shift. Δ/ε_F is referred to as a measure of the pairing strength for single-band superconductors.

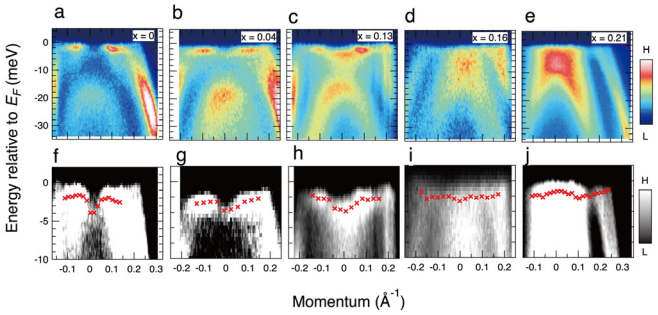

Fig. 2. ARPES intensity plots of $FeSe_{1-x}S_x$ along the Γ−M direction measured in the SC state. (a)-(e) ARPES intensity plots of x = 0, 0.04, 0.13, 0.16, and 0.21 along the Γ-M direction taken at 2 K with s-polarized incident light. (f)-(j) Enlarged plots of (a)-(e) around E_F. The red markers represent the BQP band dispersions determined from the energy distribution curves.

gap at $k = 0$ is expected, which is upward convex around $k = 0$ in the case of a hole band below E_F, as shown in Fig. 1d. In the crossover regime, the BQP dispersion is intermediate between two extreme cases and the flat dispersion appears. In the crossover regime, a pseudogap is also expected to open at a temperature higher than T_c as a result of preformed bosonic pairs, as shown in Fig. 1a. Here, we provide systematic evidence for the BCS-BEC crossover in iron-based superconductors $FeSe_{1-x}S_x$ from laser-excited angle-resolved photoemission spectroscopy, and show that the system enters the BEC regime with $x = 0.21$, where the nematic state that breaks the orbital degeneracy is fully suppressed.

Figures 2a-2e show the ARPES intensity plots of $FeSe_{1-x}Se_x$ (where x = 0, 0.04, 0.13, 0.16, and 0.21) taken in the SC state with s-polarized light. To see the BQP band dispersions more clearly, we show enlarged plots around E_F in Figs. 2f-2j. We have plotted the BQP band dispersions determined from the energy distribution curves (EDCs) of each composition as indicated by red markers. From these plots, we can see that the BQP band dispersion, which is downward convex at $x = 0$, systematically changes and becomes flat at $x = 0.16$; it then, eventually, becomes upward convex at $x = 0.21$. This systematic change is consistent with that expected from the chemical potential shift in the BCS-BEC crossover, as shown in Figs. 1b-1d, and thus strongly suggests that $FeSe_{1-x}S_x$ is tuned from the BCS-BEC crossover regime ($x = 0$) to the BEC regime ($x = 0.21$). To obtain complete evidence for the BCS-BEC crossover, we have investigated the existence of a pseudogap, and found that the pseudogap appears at $T^* \sim 15$ K for $x = 0.21$. Thus, from the BQP band and the existence of the pseudogap, we have concluded that BEC superconductivity is realized for $x = 0.21$. We have also investigated the substitution dependence of Δ/ε_F, where where Δ and ε_F are the SC gap and the Fermi energy, respectively, and from the obtained substitution dependence, we have also concluded that the multiband nature is important for the realization of BEC superconductivity in this system, and that it is induced by the suppression of electronic nematicity.

Reference
[1] T. Hashimoto, Y. Ota, A. Tsuzuki, T. Nagashima, A. Fukushima, S. Kasahara, Y. Matsuda, K. Matsuura, Y. Mizukami, T. Shibauchi, S. Shin, and K. Okazaki, Sci. Adv. **6**, eabb9052 (2020).

Authors
T. Hashimoto, Y. Ota, A. Tsuzuki, T. Nagashima, A. Fukushima, S. Kasahara[a], Y. Matsuda[a], K. Matsuura[b], Y. Mizukami[b], T. Shibauchi[b], S. Shin[b], and K. Okazaki
[a]Kyoto University
[b]The University of Tokyo